RF Design of a Transverse Mode Cavity for Kaon Separation

M. McAshan [1]), R. Wanzenberg [2])

[1]) FERMILAB, P.O. Box 500, Batavia, Illinois 60510, USA
[2]) DESY, Notkestr. 85, 22603 Hamburg, Germany

March 22, 2001

Abstract

Two deflecting mode RF systems can be used to separate secondary kaons from a momentum selected particle beam, primarily consisting of a mix of protons, pions and kaons, by a time of flight method. The principles of this methods and the choices of the parameters are explained. It is planned to use a 3.9 GHz 13-cell super-conducting cavity operated in a π-dipole-mode. First, the passband structure of different cavity shapes, which mainly differ by the cell-to-cell coupling and the resulting dispersion slope, is investigated. The main concern is the frequency difference between the π-mode and the next lowest mode in the same passband and the implications on the tuneability of the cavity. For three shapes the possible end-cell designs for a 7-cell and 13-cell cavity are presented. All numerical field calculations are performed by the MAFIA code. An equivalent circuit model, based on a two chain model, is applied to a 7-cell cavity. It is demonstrated that the dispersion diagram obtained by MAFIA calculations can be very well approximated by this equivalent circuit.

Contents

1 Introduction **4**

2 Cavity Shapes **8**

3 Basic Design Parameters of a Transverse Mode Cavity **11**

4 Results for Single Cell Cavities **15**
4.1 Comparison of the basic design parameters for different cavity shapes. 19

5 End-cell Design **24**

6 Multi-cell Results **29**
6.1 7-cell and 13-cell cavities of shape A15 29
6.2 7-cell cavity of shape B19 36
6.3 13-cell cavity of shape C15 39

7 Equivalent-Circuit Modeling of Transverse-Mode Structures **42**
7.1 Introduction 42
7.2 Equivalent-Circuit Modeling of the Forward-Wave Deflection Structure 42
7.3 Discussion 46
7.4 Equivalent-Circuit Modeling of the Backward-Wave Deflection Structure 49
7.4.1 The Two-Chain Model 49
7.4.2 The Single Chain Model 52
7.4.3 Modeling Problems 54

8 Conclusion **55**

A Properties of the Longitudinal and Transverse Voltage of a Cavity **57**
A.1 The relation between $\boldsymbol{V}_\perp$ and $V_\parallel$ 57
A.2 Properties of $V_\parallel(r,\phi)$ and the Dependence of $\boldsymbol{V}_\perp$ on the radius. . 58

B A 7-cell cavity of shape B19 with an uncompensated end-cell **60**
B.1 Modes from a MAFIA calculation 60
B.2 Eigenvalues and Eigenvectors from a MAFIA Calculation 63
B.3 System Matrix 64
B.4 Table of Eigenvalues and Eigenvectors from Double-Chain Model . 65

B.4.1 Upper Band 65
B.4.2 Lower Band 66
B.5 Some Results from the Modeling and MAFIA Studies of a 13-Cell Structure of B15 Shape with a Tuned End Cell 67

C Modes of a 13-cell cavity of shape C15 with a tuned end-cell **68**

D Cavity of shape C15 with an alternative end-cell design **74**

E Separator System and RF Cavity Parameters **77**

References **79**

1 Introduction

The Fermilab Main Injector will produce intense beams of protons for fixed target experiments. For kaon physics [1] the extracted primary proton beam of momentum 120 GeV/c will strike a thick target, and the generated secondary particles pass through a momentum selection stage. These particles are primarily a mix of protons, pions and kaons of the same momentum but of different speeds. The kaons can be separated by a time of flight separation using two rf-systems. The set-up is schematically shown in Fig. 1. Kaons, pions and protons are kicked by an transverse mode rf-system (#1) and transfered through an optical system, which performs a $-I$ mapping to the second rf-system. The pions arrive earlier at the second rf-stations and are kicked onto a beam stopper while the kaons are passing the beam stopper. The protons arrive later than the pions and kaons and are kicked to the beam stopper, too.

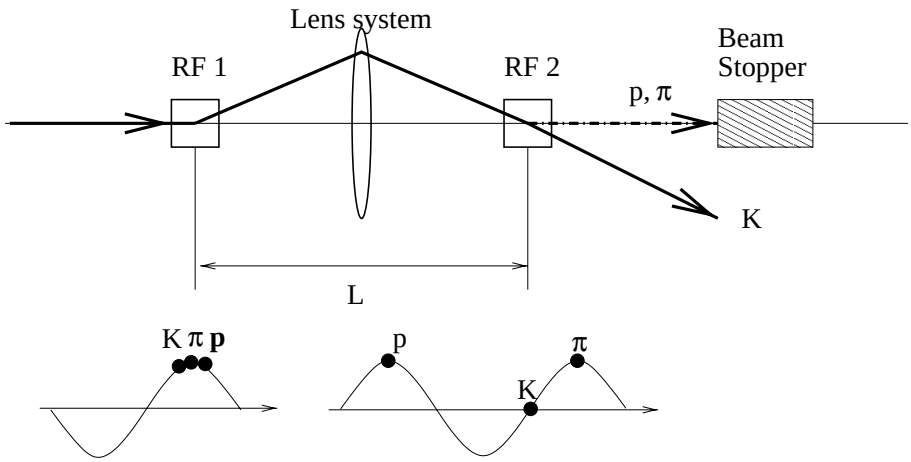

Figure 1: Kaon beam separation.

The phase slip between pions and kaons is given by:

$$\Delta\phi = 2\,\pi\;f\,L\,\frac{1}{c}\left(\frac{1}{\beta_K} - \frac{1}{\beta_\pi}\right),$$

where f is the frequency of the rf-systems, L the distance between the two rf-systems, and β_K, β_π the normalized (with respect to c) velocities of the kaon and pion beams. For a momentum of 22 GeV/c the velocities are: $\beta_K = 0.999748$, $\beta_\pi = 0.99998$ and $\beta_p = 0.99909$ (protons). For the required phase slip of $2\,\pi$ between the pions and protons, the slip between the pions and kaons is $\sim \pi/2$. This leads to a condition for the product of the rf-frequency and the distance between the rf-systems

$$f \cdot L \approx \frac{\Delta\phi_p}{2\,\pi}\,2\,c\,\gamma_p^2 \approx 330\ \mathrm{GHz}\cdot\mathrm{m}.$$

Since the lifetime of kaons in their rest frame is only $\tau \cdot c = 3.7\,\mathrm{m}$ or about 200 m in the laboratory frame for 22 GeV/c kaons the distance L should be reasonably short, consistent with a fraction of the total beam line length and acceptable frequencies. The following choice fulfill the requirements:

$$f = 3.9 \text{ GHz}, \quad L \approx 86.5 \text{ m}.$$

Copper and niobium models of the transverse mode cavities have been built. Fig. 2 shows a one cell copper model with beam pipes and a one and two half cell niobium model between two shorting plates. Furthermore a five cell niobium model (shown in Fig. 3) has been built and tuned to the deflecting dipole mode.

Figure 2: Copper and niobium models of the transverse mode cavities. Two shorting plates have been added to the one cell and two half cell niobium model.

The radial kick per unit length θ' due the electric and magnetic field of the dipole mode is given as an integral of Lorentz force:

$$\theta' = \frac{e}{E}\,\frac{1}{L_{cav}}\int_0^{L_{cav}} dz\; \boldsymbol{e_r} \cdot \left(\boldsymbol{E}_\perp(r,\phi,z,t=z/c) + c\,\boldsymbol{e_z} \times \boldsymbol{B}(r,\phi,z,t=z/c)\right), \tag{1}$$

where e is the charge and E the energy of the kicked particle.

A 3D-view of the electric and magnetic field of the π-mode, which is used to deflect the beam, is shown in Fig. 4 and Fig. 5. The computer code MAFIA [2]

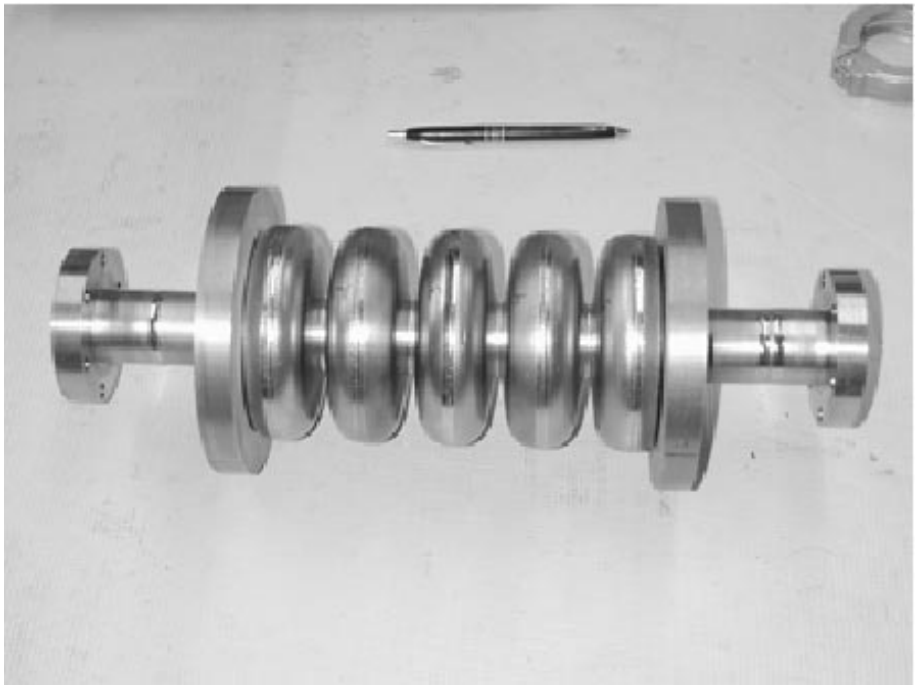

Figure 3: Five cell Niobium prototype transverse mode cavity.

has been used to obtain the fields which are shown in the figures. The boundary conditions correspond to the case shown in Fig. 2 where two shorting plates have been added to a configuration with one full and two half cells. This situation also represents the case of a periodic structure of cavities where no end-cell effects are present.

The geometrical properties of the considered cavity shapes are discussed in the next section, while basic design parameters of dipole (or deflecting) mode cavities are introduced in section 3. These parameters are compared for several cavity shapes in section 4. From the dispersion diagram two regimes can be distinguished: the weakly and the strongly coupled regime. The design of an end-cell is discussed in section 5 for both regimes. The results are applied to 7-cell and 13-cell cavities in section 6. It is demonstrated that, it is possible to obtain a good field flatness of the deflection π-mode for the weakly and the strongly coupled regime. Finally, an equivalent circuit model is presented in section 7. It is shown that the MAFIA results can be very well approximated by a two-chain equivalent circuit.

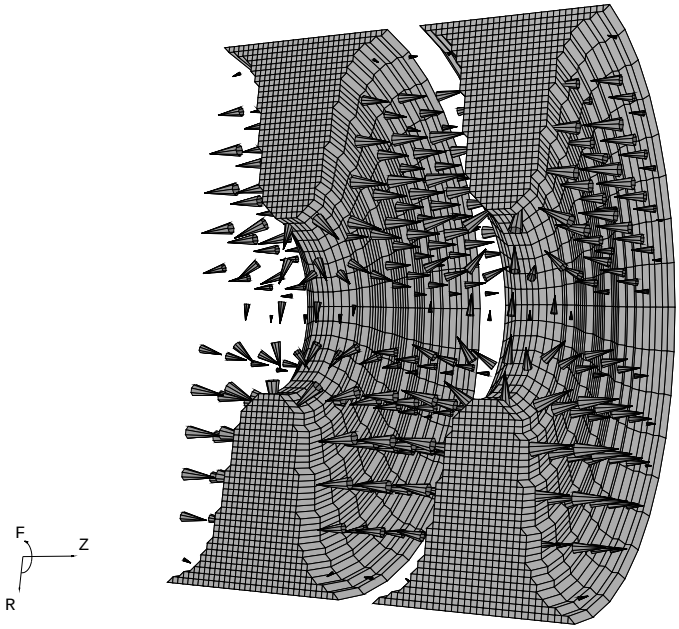

Figure 4: Cavity of shape C15, electric field of dipole π-mode

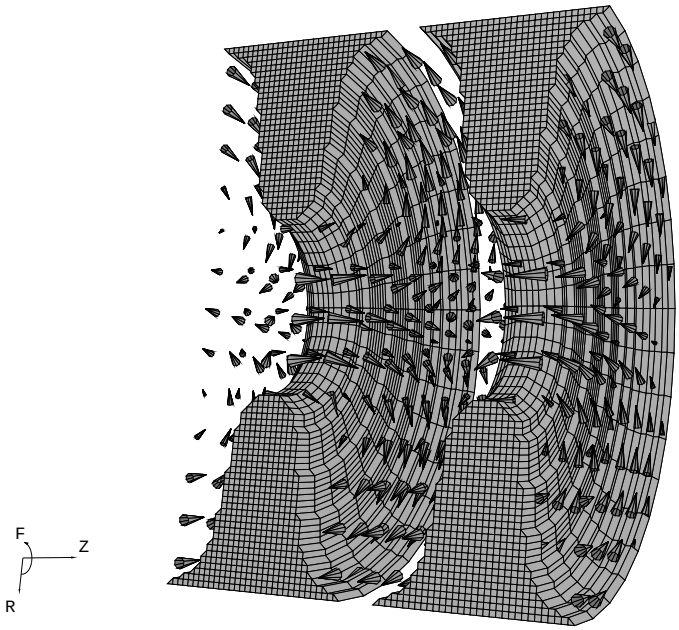

Figure 5: Cavity of shape C15, magnetic field of dipole π-mode

2 Cavity Shapes

The basic shape of a cavity half cell is schematically shown in Fig. 6. The curve in the (r, z)-plane consists out of two circle segments, which are smoothly connected by a straight line. The circle at the iris (center $(a + r_i, 0)$) is defined by the equation:

$$R_i(z) = a + r_i - r_i \sqrt{1 - \left(\frac{z}{r_i}\right)^2},$$

for $0 \leq z \leq z_1$, while the equator circle is defined by:

$$R_e(z) = b - r_e + r_e \sqrt{1 - \left(\frac{z - g/2}{r_e}\right)^2},$$

for $z_2 \leq z \leq g/2$. The connecting straight line is defined by the two mid-points (r_1, z_1) and (r_2, z_2):

$$R_c(z) = \frac{r_2 - r_1}{z_2 - z_1}\,(z - z_1) + r_1,$$

for $z_1 \leq z \leq z_2$, with $r_1 = R_i(z_1)$ and $r_2 = R_i(z_2)$. The mid-points can be

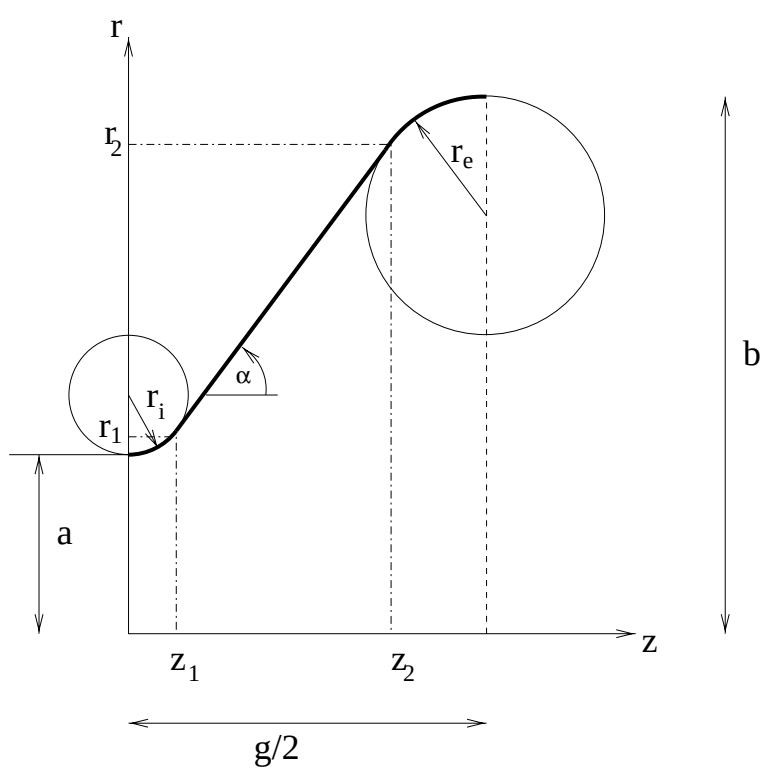

Figure 6: Schematic view of the cavity shape.

calculated from the basic cavity shape parameters a,b,r_i,r_e and $g/2$. Using the

angle α as an auxiliary parameter one obtains

$$z_1 = r_i \cos\alpha \tag{2}$$

$$z_2 = -r_e \cos\alpha + \frac{g}{2} \tag{3}$$

since the connecting straight line is tangential with respect to both circles. The angle α is related to the basic cavity shape parameters according to

$$\tan\alpha = \frac{(g/2)^2 - (r_i + r_e)^2}{(g/2)\ d + (r_i + r_e)\sqrt{d^2 + (g/2)^2 - (r_i + r_e)^2}}, \tag{4}$$

where $d = b - r_e - (a + r_i)$ is the radial distance between the two circle centers.(The details of that calculations are omitted here.)

An overview on all considered cavity shapes can be found in table 1. Three series (A,B and C) with different iris and equator curvatures are considered. Furthermore the cavities differ by their iris radius, which is used to label the different shapes.

The shape A15 (shown in Fig. 7) is used for the copper and niobium model cavity prototypes, which have been built for first measurements, while the shape C15 (also shown in Fig. 7) is the most recent (almost final) shape. In Fig. 8 all cavities of shape A and B are shown which are listed in table 1.

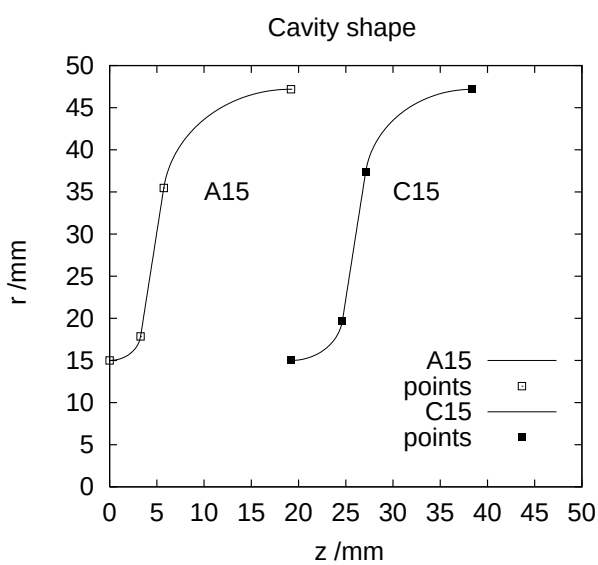

Figure 7: Shape of the deflecting mode prototype cavity half cell (shape A15) and the most recent cavity half cell design (shape C15). The midpoints are $(z_1, r_1) = (3.28, 17.85)$ mm and $(z_2, r_2) = (5.73, 35.47)$ mm for cavity A15, and $(z_1, r_1) = (5.45, 19.74)$ mm and $(z_2, r_2) = (7.90, 37.34)$ mm for cavity C15.

Label	3.9 GHz transverse mode cavities		
A	curvature radius:		
	at iris (r_i)	at equator (r_e)	
	3.31 mm	13.6 mm	
	Iris radius (a)	Equator radius (b)	a/b
A13	13 mm	47.875 mm	0.2715
A15	15 mm	47.19 mm	0.3179
A17	17 mm	46.437 mm	0.3661
A19	19 mm	45.874 mm	0.4141
A25	25 mm	45.7 mm	0.5470
B	curvature radius:		
	at iris (r_i)	at equator(r_e)	
	4.5 mm	12 mm	
	Iris radius (a)	Equator radius (b)	a/b
B15	15 mm	47.19 mm	0.3179
B18	18 mm	46.31 mm	0.3887
B19	19 mm	46.18 mm	0.4114
C	curvature radius:		
	at iris (r_i)	at equator(r_e)	
	5.5 mm	11.41 mm	
	Iris radius (a)	Equator radius (b)	a/b
C15	15 mm	47.18 mm	0.3179

Table 1: Geometrical parameters of the cavity shapes. The length of a cavity half cell is 19.2 mm for all cases.

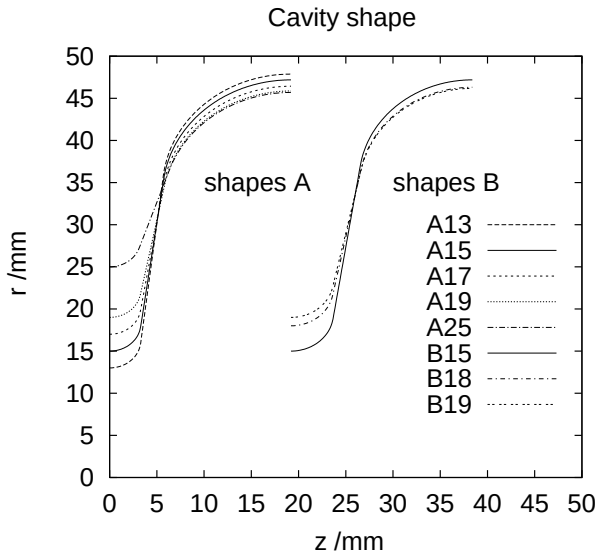

Figure 8: Half cell shapes of cavities A13 ... A25 and B15 ... B19.

3 Basic Design Parameters of a Transverse Mode Cavity

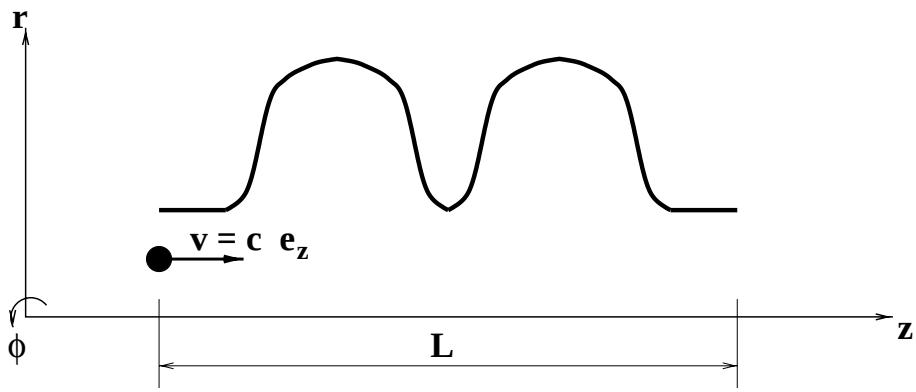

Figure 9: A test particle is traversing a cavity.

The effect of the electric and magnetic fields on a test particle traversing the cavity parallel to the cavity axis can be calculated from the following integrals of the Lorentz force:

$$\boldsymbol{V}_\perp(r,\phi) = \int_0^L dz\ \left(\boldsymbol{E}_\perp(r,\phi,z,t=z/c) + c\,\boldsymbol{e_z}\ \times\ \boldsymbol{B}(r,\phi,z,t=z/c)\right) \tag{5}$$

It is assumed that the test particle is moving with the velocity $\boldsymbol{v} = c\,\boldsymbol{e_z}$ at the transverse coordinate (r,ϕ) through the cavity of length L (see Fig. 9). A cylindrical coordinate system has been chosen, $\boldsymbol{e_z}$ is the unit vector in the direction of the z-axis. $\boldsymbol{E}_\perp = \boldsymbol{e_z} \times (\boldsymbol{E} \times \boldsymbol{e_z})$ is the transverse component of the electric field. The radial kick on the test particle is given by

$$\theta = \frac{e\,V_{\perp\,r}}{E}, \tag{6}$$

where E is the energy of the test particle, e the charge of an electron and $V_{\perp\,r}$ the radial component of the transverse voltage vector.

The integrated longitudinal effect of the cavity fields are given by the following integral:

$$V_{||}(r,\phi) = \int_0^L dz\ E_z(r,\phi,z,t=z/c). \tag{7}$$

Note that this approach describing the interaction between the test particle and the fields is not self consistent. Nevertheless this is a very good approximation for highly relativistic particles.

It is sufficient to calculate $V_{||}$ since the transverse voltage $\boldsymbol{V}_\perp$ is related to the longitudinal one by the Panofsky-Wenzel-Theorem [4] (see appendix A). Consider

especially a cavity mode ringing with the frequency $f = \omega/(2\,\pi)$. One obtains in complex notation for the electric field:

$$\boldsymbol{E}\,(r,\phi,z,t) = \widetilde{\boldsymbol{E}}\,(r,\phi,z)\,\exp(-i\,\omega\,t).$$

For the voltages the following relation are valid:

$$\begin{aligned} \boldsymbol{V}_{\perp}\,(r,\phi) &= \frac{-i}{\omega/c}\,\boldsymbol{\nabla}_{\perp}\,V_{\|}(r,\phi) \\ V_{\|}(r,\phi) &= \int_0^L dz\,\widetilde{E}_z(r,\phi,z)\,\exp(-i\,\omega\,z/c). \end{aligned} \tag{8}$$

Generally the fields $\widetilde{\boldsymbol{E}}\,(r,\phi,z)$ and $\widetilde{\boldsymbol{B}}\,(r,\phi,z)$ in geometries of cylindrical symmetry can be written as (multi-pole expansion):

$$\begin{aligned} \widetilde{\boldsymbol{E}}\,(r,\phi,z) &= \sum_m \Big(\widetilde{E_r^{(m)}}(r,z)\,\cos(m\,\phi)\quad \boldsymbol{e_r} \\ &\quad + \widetilde{E_\phi^{(m)}}(r,z)\,\sin(m\,\phi)\quad \boldsymbol{e_\phi} \\ &\quad + \widetilde{E_z^{(m)}}(r,z)\,\cos(m\,\phi)\quad \boldsymbol{e_z} \Big) \\ \widetilde{\boldsymbol{B}}\,(r,\phi,z) &= \sum_m \Big(\widetilde{B_r^{(m)}}(r,z)\,\sin(m\,\phi)\quad \boldsymbol{e_r} \\ &\quad + \widetilde{B_\phi^{(m)}}(r,z)\,\cos(m\,\phi)\quad \boldsymbol{e_\phi} \\ &\quad + \widetilde{B_z^{(m)}}(r,z)\,\sin(m\,\phi)\quad \boldsymbol{e_z} \Big). \end{aligned} \tag{9}$$

The computer codes URMEL [3] and MAFIA [2] can be used to calculate the field components $\widetilde{E_r^{(m)}}$, $\widetilde{E_\phi^{(m)}}$, etc. As shown in the appendix A one obtains for the radial component of the transverse voltage for a **m-pole mode**:

$$V_{\perp r}^{(m)}(r,\phi) = \frac{-i}{\omega/c}\,\frac{m}{r}\,V_{\|}(r,\phi)^{(m)}. \tag{10}$$

For a dipole mode (m=1) $V_{\perp r}^{(m)}(r,\phi)$ is independent of the radius r. The kick on the beam due to a dipole mode in the cavity does not depend on the radial position of the trajectory.

From the numerically calculated fields (using MAFIA [2]) the longitudinal voltage

$$V_L^{(1)}(r) = \int_0^L dz\,\widetilde{E_z^{(1)}}(r,z)\exp(-i\,\omega\,z/c), \tag{11}$$

and the total stored energy of the dipole mode

$$U = \frac{\epsilon_0}{2}\,\int d^3r\,\left|\widetilde{\boldsymbol{E}^{(1)}}\right|^2 \tag{12}$$

are calculated. Usually $V_L^{(1)}(r)$ is calculated at the iris radius ($r = a$) of the cavity. Note that the transverse voltage of a dipole mode is now simply:

$$V_{\perp r}^{(1)}(r, \phi = 0) = \frac{-i}{\omega/c} \frac{1}{r} V_L^{(1)}(r), \tag{13}$$

which is independent of r since $V_L^{(1)}(r)$ depends linearly on the radius.

From the voltage and stored energy the following important parameters can be calculated (this is usually done by the MAFIA post-processor):

$$\begin{aligned} k^{(1)}(r) &= \frac{\left|V_L^{(1)}(r)\right|^2}{4\,U} \\ \frac{R^{(1)}(r)}{Q} &= \frac{2\;k^{(1)}(r)}{\omega} \\ \left(\frac{R}{Q}\right)' &= \frac{R^{(1)}(r)}{Q} \frac{1}{(r\;\omega/c)^2}. \end{aligned} \tag{14}$$

$k^{(1)}(r)$ is the dipole loss parameter. A charge q transversing the cavity with radial offset r will lose the energy $q^2\;k^{(1)}(r)$ into the dipole mode. $R^{(1)}(r)/Q$ is the dipole mode shunt impedance of the cavity divided by the quality factor of the cavity.

An **important design parameter** of a dipole mode cavity is $\boldsymbol{(R/Q)'}$ which does not depend on the radius. If the power P is fed into the cavity the following transverse voltage is obtained:

$$V_T = \sqrt{2\left(\frac{R}{Q}\right)' P\,Q_{ext}} = \frac{1}{(r\;\omega/c)} V_L(r). \tag{15}$$

Q_{ext} is the external quality factor of the cavity, which is for a super-conducting cavity mainly determined by the coupler. Often the factor 2 is absorbed into the definition of $(R/Q)'$. Therefore parameters quoted in reference [1] does differ by a factor of two from results given in this report.

For a design of the cryogenic system it is important to know the power P_{sur} developed on the inner cavity due to the surface resistivity R_{sur}. The power dissipated into the surface can be calculated from the tangential magnetic field:

$$P_{sur} = \frac{1}{2} R_{sur} \int dA\,|H_\phi|^2\,. \tag{16}$$

For a super-conducting cavity the surface resistance is the sum of the BCS (Bardeen, Cooper, Schrieffer) resistance R_{BCS}, which depends on the frequency and the temperature, and a residual resistivity R_{res}.

The power which is dissipated into the cavity surface can also be characterized by the quality factor Q or the **parameter G_1** [5].

$$Q = \frac{\omega\ U}{P_{sur}} \tag{17}$$

$$G_1 = R_{sur}\ Q. \tag{18}$$

G_1 is independent of frequency and cavity material. Therefore G_1 will be quoted throughout this report for the different cavity shapes.

In the MAFIA post-processor by default the dissipated power P_{sur} is calculated for a copper cavity with the surface resistivity:

$$R_{Cu} = \sqrt{\frac{\omega\ \mu_0}{2\ \sigma_{Cu}}}, \qquad \sigma_{Cu} = 5.8 \cdot 10^7\ (\Omega\,\mathrm{m})^{-1}. \tag{19}$$

For a frequency of $\omega = 2\,\pi\,3.9\,\mathrm{GHz}$ the surface resistivity of copper is $R_{Cu} = 16.4\,\mathrm{m}\Omega$. From the quality factor for copper and R_{Cu} the parameter G_1 is obtained.

Furthermore the **peak magnetic surface field** B_{max} for a given transverse cavity voltage V_T is calculated by the MAFIA code for each cavity geometry. This parameter finally determines which deflecting voltage can be achieved. We assume that a peak magnetic surface field of 0.1 T is a safe upper limit.

4 Results for Single Cell Cavities

In this section results for single cell cavities are presented, which have been obtained from numerical calculations with the computer code MAFIA. In Fig. 10 the shape of the cavity C15 is shown together with the MAFIA grid (about 7300 grid points, 0.5 mm step size). No beam pipe is connected to the cavity. The left and right boundaries of the cavity are shorting plates in the equator plane of the cavity (i.e. *electric boundary conditions* in MAFIA). The eigenvalues and eigenvectors (modes) of that cavity are calculated. Table 2 summarized the results of the first 2 modes, listing not only the frequency but also the parameters $(R/Q)'$ and G_1. In the same table the results for the first 2 modes using *magnetic boundary conditions* are included, too.

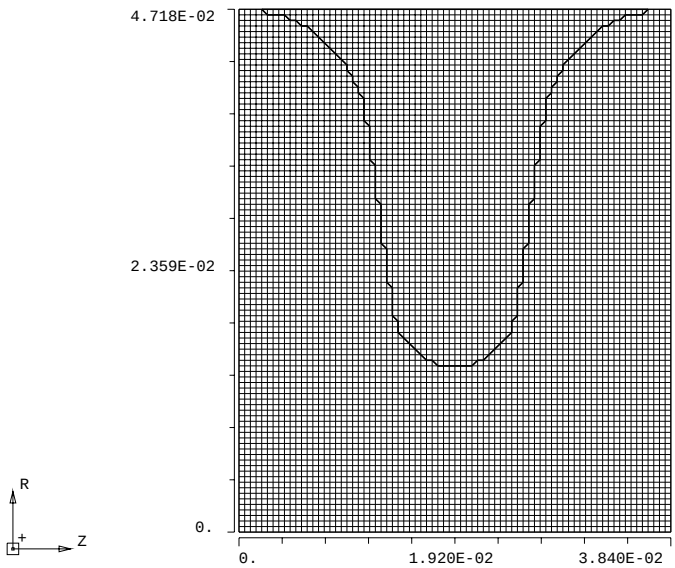

Figure 10: Single Cell Cavity shape C15 approximated on the MAFIA grid.

mode #	f / GHz	$(R/Q)'$ / Ohm	G_1 / Ohm	comment
EE-1	3.899	27.3	228	π-mode (band 1), TM-like
EE-2	4.061	10.9	287	0-mode (band 1),TM-like
MM-1	4.361	3.2	234	0-mode (band 2), TE-like
MM-1	5.349	0.74	508	π-mode (band 2), TE-like

Table 2: Results from the MAFIA eigenvalue solver and post-processor for a single cell of cavity C15. The value of G_1 is calculated without the shorting plates.

Plots of the electric field for these modes are shown in Fig. 11. The field is

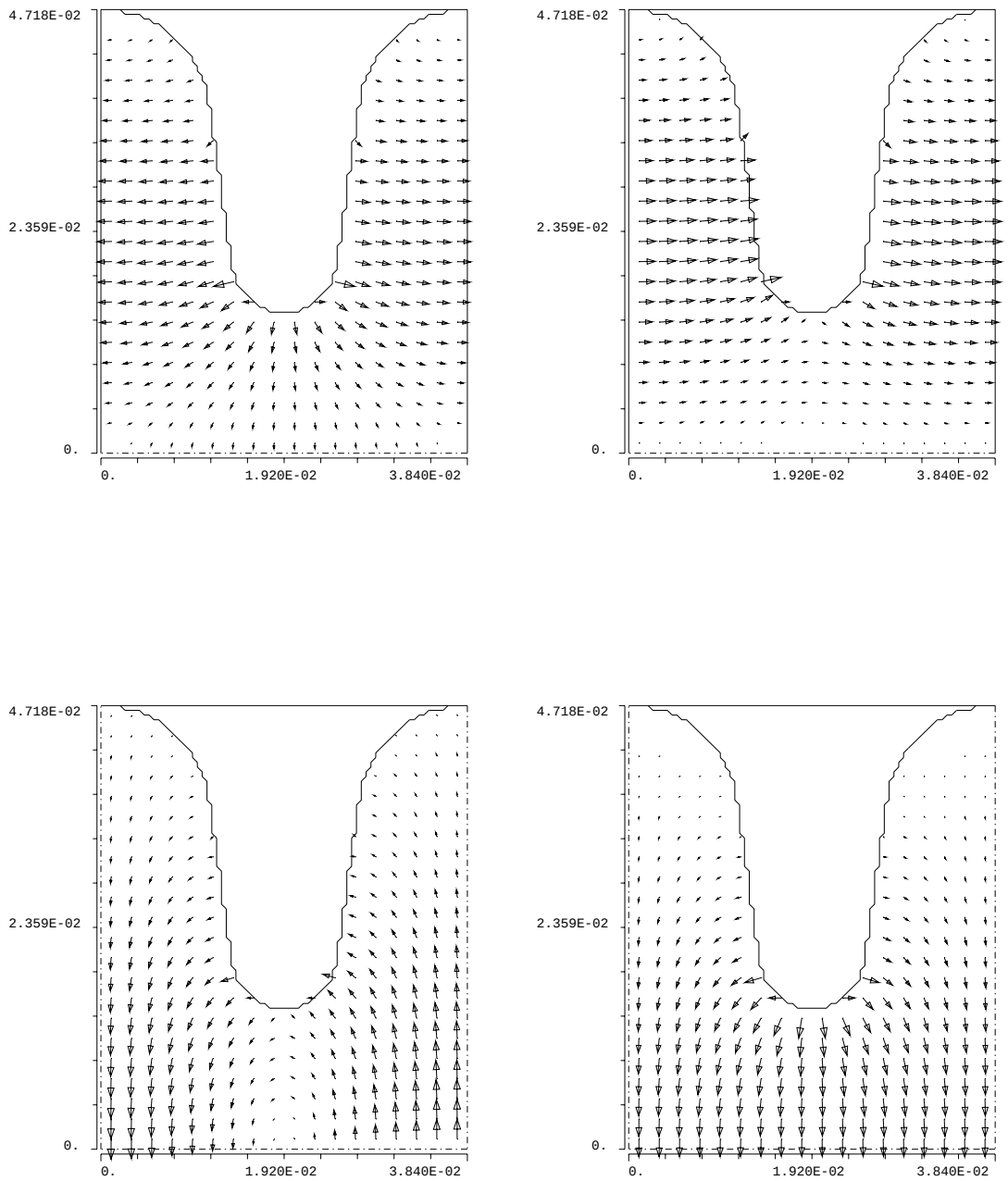

Figure 11: Results from a MAFIA [2] calculation: Electric field of the EE-1 (top left graph), the EE-2 (top right graph), the MM-2 (bottom left graph) and the MM-1 mode (bottom right graph), in the plane $\phi = 0$. (electric or magnetic (solid/dashed line) shorting plates at both ends of the cavity).

shown for an azimuthal angle of $\phi = 0$, i.e. the azimuthal electric field is zero in that plane. The first mode (top left graph of Fig. 11) is the π-mode, which will be used to deflect the particles. The cell length L_{cell} is chosen in such a way that a particle transversing the cavity with almost the velocity of light will always be synchronous with the field. The electric field of a π-mode in a periodic structure of cavities is schematically shown in Fig. 12. The dashed box marks one cell of the chain of cavities corresponding to the cell used for the MAFIA one cell calculations (Fig. 11). All modes of an infinite periodic chain of cavities can be

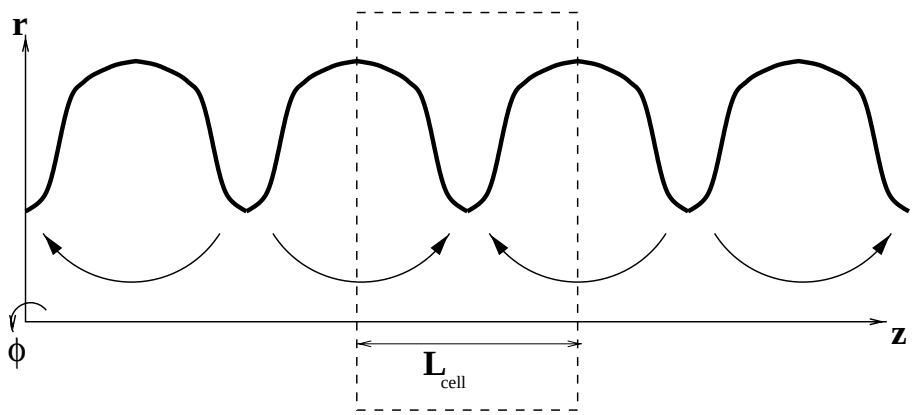

Figure 12: Periodic structure of cavities. The arrows indicate the direction of the electric field of a mode with a phase advance of π.

obtained from single cell calculations using periodic boundary conditions:

$$\widetilde{\boldsymbol{E}}^{(1)}(r, z + L_{cell}) = \widetilde{\boldsymbol{E}}^{(1)}(r, z)\ \exp(i\varphi), \tag{20}$$

φ is the phase advance per cell. A phase advance of 180° (or π) corresponds to the case shown in Fig. 11 (top left graph), where shorting plates are used at the left and right boundary of the cavity cell. The modes can be labeled by their phase advance φ per cell. Numerical calculations with the computer code MAFIA have been done for 13 different values for φ in the range from 0° to 180° (15° steps in φ). Modes with approximately that phase advance will be present in a 13-cell cavity. The frequencies of the lowest two pass-bands (see [7]) are graphically represented in form of dispersions curve in Fig. 13 for the cavity shape A15 and C15. The first passband is shown in Fig. 14 for the cavity shapes A13, A15, A17, A19 and A25. The slope of the dispersion curves is changing from negative values (backward wave structure, or negative group velocity) for the shapes A13 and A15 to positive values (forward wave structure, or positive group velocity) for the shapes A17, A19 and A25.

A 13-cell cavity will be harder to tune if the dispersion curve is very flat since more than one mode may be excited during the tuning procedure which is performed at room temperature. Therefore a **further design criteria** is the

total width of passband and especially the **frequency difference** of the modes with phase advances of 165° and 180°.

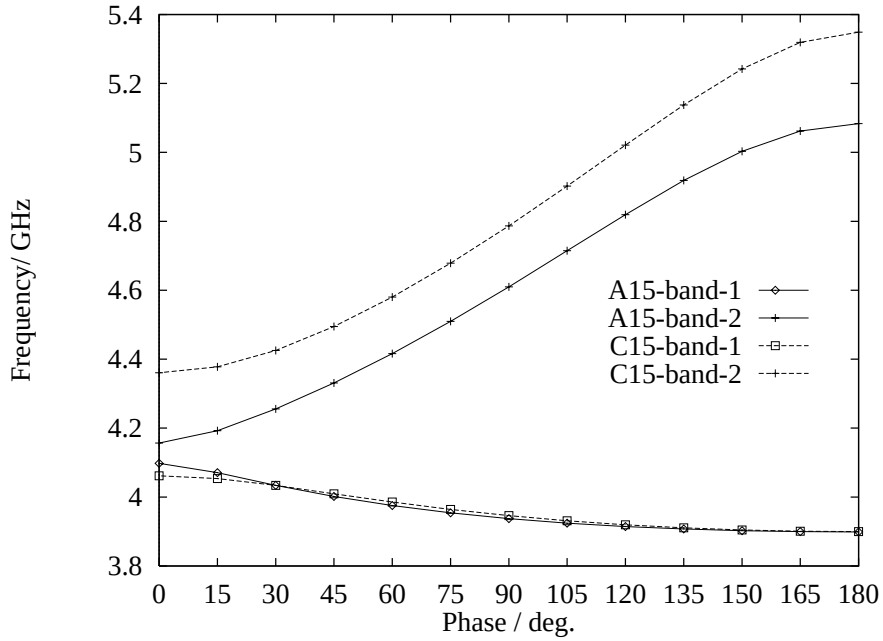

Figure 13: Dispersion curve of the first and second dipole passband of a cavity with shape A15 and C15.

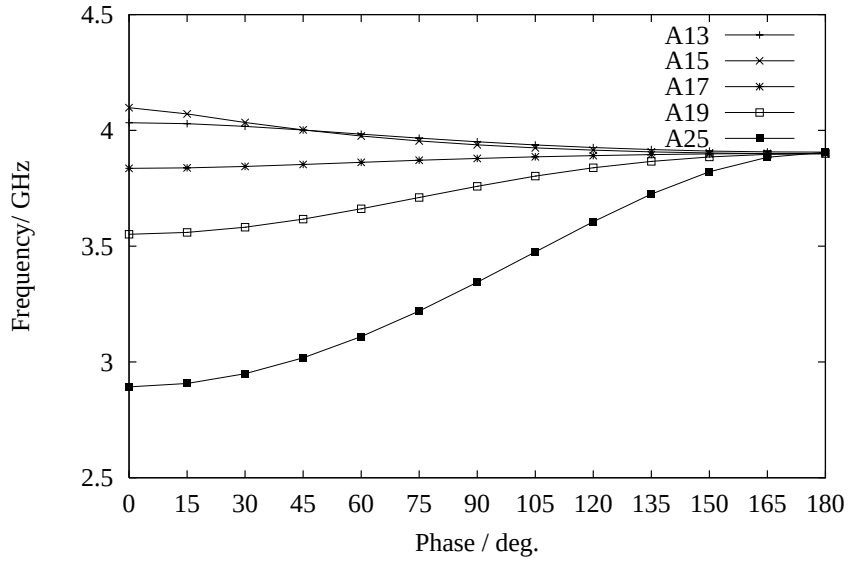

Figure 14: Dispersion curve of the first dipole passband of the cavities of shape A13 ... A25

The width of a resonance δf is determined by the quality factor Q: $\delta f = f/(2\,Q)$. The electric resistivity of Niobium at a temperature of 273 K is $15.2 \cdot 10^{-8}\ \Omega\,\mathrm{m}$ [8], which is about 10 times higher than the resistivity of copper. Therefore a unloaded Q of about 5000 is expected for the π-mode at room temperature, i.e. during tuning of the cavity. The relative mode separation of the π-mode and the $11\,\pi/12$-mode (165°-mode) should be at least three times the relative width of the resonance:

$$\frac{\Delta f}{f_\pi} = \frac{f_\pi - f_{11\,\pi/12}}{f_\pi} = 3\,\frac{\delta f}{f_\pi} = 3\,\frac{1}{2\,Q} \approx 3 \cdot 10^{-4}, \tag{21}$$

to ensure a clear separation of the two modes.

4.1 Comparison of the basic design parameters for different cavity shapes.

The basic design parameters $(R/Q)'$, G_1 and the peak magnetic field near the surface B_{max} have been calculated for all cavity shapes listed in table 1 using the MAFIA post-processor. The quantity $(R/Q)'$ depends linearly on the iris radius, see Fig. 15. The cavities of shape B, which have an larger iris curvature than the

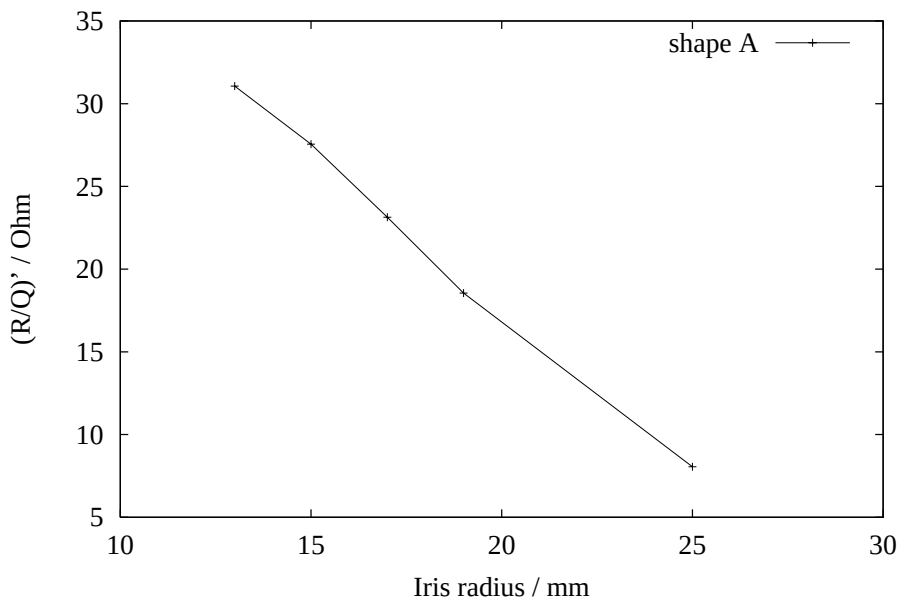

Figure 15: $(R/Q)'$ of the cavities of shape A13 ...A25. The iris radius, which labels the different cavity shapes, is used for the abscissa.

shape A cavities, have almost the same $(R/Q)'$ for the same iris radius. Table 3 summarized the results for all considered cavity shapes and shows the relative advantages of the C15 shape.

Label	f/MHz	$(R/Q)'$ /Ω	G_1 /Ω	B_{max}/T	$\delta f/f_\pi$ / 10^{-4}
A13	3905.9	31.1	253	0.077	−3.15
A15	3898.7	27.6	247	0.087	−2.36
A17	3900.6	23.1	237	0.097	1.53
A19	3900.1	18.6	238	0.107	9.4
A25	3905.6	8.1	261	0.135	55.7
B15	3904.7	27.3	236	0.077	−2.81
B18	3900.7	20.8	231	0.091	2.72
B19	3892.3	18.6	231	0.095	6.26
C15	3899.7	27.3	228	0.073	−3.04

Table 3: Summary of the results obtained from the MAFIA calculations for one-cell cavities. The magnetic field is calculated near the cavity surface (0.25 from the surface on the dual MAFIA mesh) for a transverse voltage of 5 MV/m. G_1 is calculated without the end shorting plates from the copper Q-values ($G_1 = 16.4 \cdot 10^{-3}\ \Omega\ Q_{Cu}$).

The parameter G_1 does not significantly depend on the iris radius. It is about $250\,\Omega$ for the cavities of shape A and about $230\,\Omega$ for shape B (without the end shorting plates). For a transverse voltage of 5 MV/m the maximum of

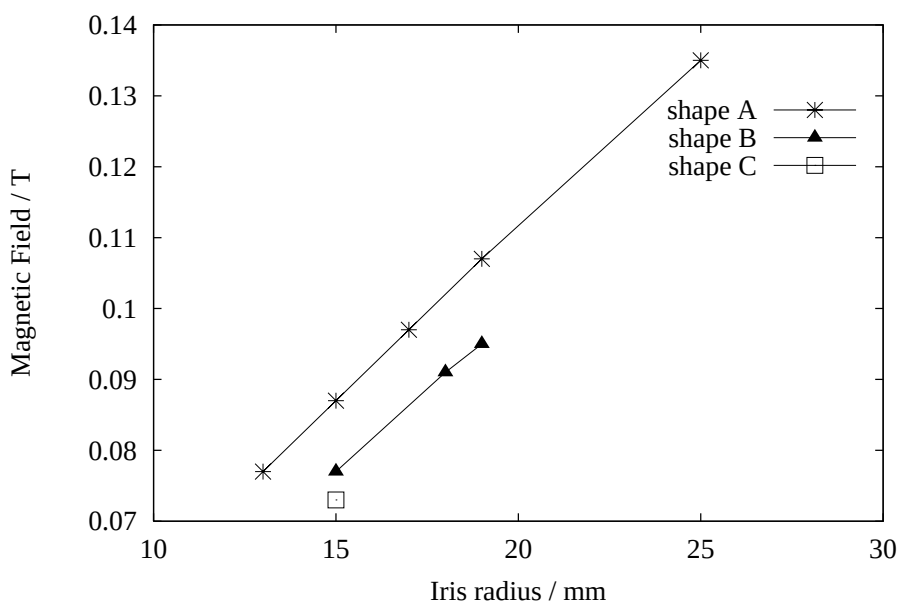

Figure 16: Maximum magnetic field near the surface for all considered cavity shapes at a transverse voltage of 5 MV/m.

the absolute magnetic field $B_{max} = \max \left| \widetilde{\boldsymbol{B}}(r, \phi = 90°, z) \right|$ has been calculated with the MAFIA post-processor. The results for the different cavity shapes are

shown in Fig. 16. Since the magnetic field is allocated in MAFIA to a dual mesh the peak field magnetic field B_{max} is found near the surface about 0.25 mm away from the surface. The magnetic field at the surface will be higher than calculated. To estimate the difference between the calculated field B_{max} and the the surface field the radial dependence of $\left|\widetilde{\boldsymbol{B}}(r, \phi = 90°, z \approx L_{cell}/2)\right|$ has been investigated for the cavity of shape A15 (see Fig. 17). Using the local slope of the function $\left|\widetilde{\boldsymbol{B}}(r, \phi = 90°, z \approx L_{cell}/2)\right|$ near $r = 14.5$ mm the surface magnetic field can be estimated to be 0.093 T for the cavity of shape A15 at 5 MV/m transverse voltage. That is about 7 % more than the value quoted in table 3. Nevertheless, the values quoted in table 3 and displayed in Fig. 16 are useful to compare the different cavity shapes since the same mesh step size of 0.5 mm have been used for all calculations.

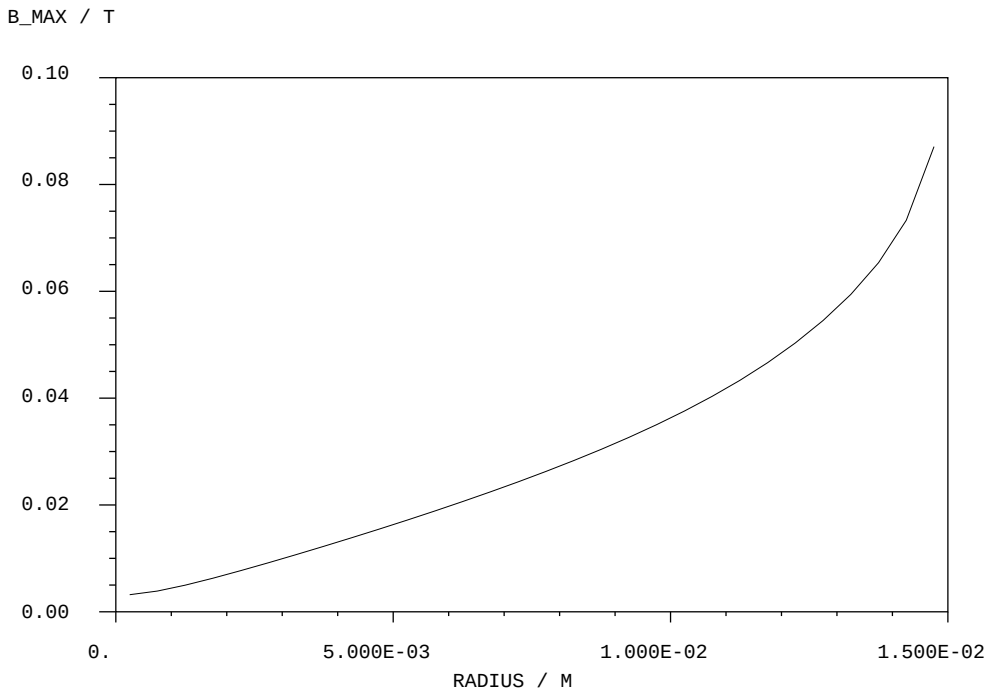

Figure 17: Radial dependence of the magnetic field in the cavity A15. The quantity $\left|\widetilde{\boldsymbol{B}}(r, \phi = 90°, z \approx L_{cell}/2)\right|$ is plotted for r from 0 to 15 mm, i.e. from the cavity axis to the cavity iris. The value for $r = 15$ mm is not calculated since the magnetic field is allocated to the dual MAFIA mesh.

The dispersion curves of the first passband of the cavities of shape A are shown in Fig. 14, while the corresponding curves for the cavities of shape B are shown in Fig. 18. Using this data the relative separation of the π-mode to the $11\,\pi/12$-mode has been calculated. The results are shown in Fig. 19 for the shapes A, B and C. The mode separation goes from negative to positive at about 17 mm iris radius and thus indicates two potential regions of iris selection (at or below

15 mm or above 18 mm). The relative mode separation exceeds the value of $3 \cdot 10^{-4}$ only for the cavities of shape A13, A19, A25, B19 and C15. Therefore only these cavities will have clearly separated modes at room temperature as have been previously calculated. The relevance of the mode separation (π from $11\,\pi/12$-mode) for the tuning of the cavities should be studied with Copper and Niobium model cavities.

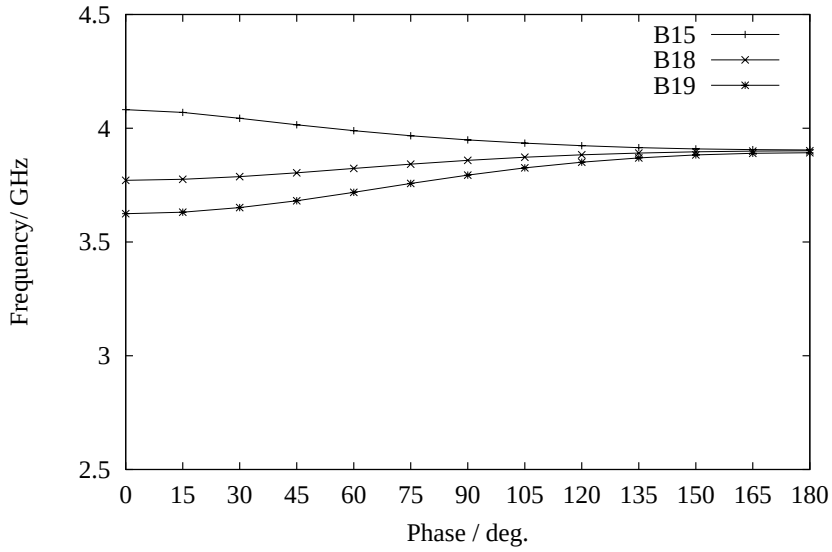

Figure 18: Dispersion curve of the first dipole passband of the cavities of shape B15, B18 and B19.

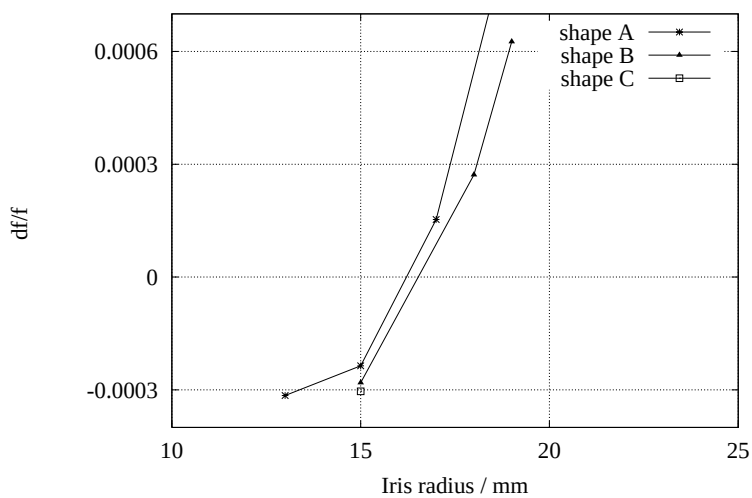

Figure 19: Relative separation $\delta f/f_\pi$ of the π-mode and the $11\pi/12$-mode for all considered cavity shapes.

The design of an end-cell is investigated for the cavities of shape A15 and B19 in the next section, while multi-cell cavities are considered in section 6. As a reference for those sections it is interesting to look at the longitudinal electric field as a function of the z-position for a fixed radius. The electric field $\widetilde{E_z}(r = 1\,\mathrm{cm}, \phi = 90°, z)$ is shown in Fig. 20 for the case of the π-mode of cavity shape C15 (Fig.11,top left graph). The electric field strength (in V/m) corresponds to the case of a transverse voltage of 5 MV/m, or

$$V_L = (r\,\frac{\omega}{c})\;V_T = 4.087\ \mathrm{MV/m} \tag{22}$$

for the longitudinal voltage at $r = 1\,\mathrm{cm}$ ($\omega = 2\pi\,3.9$ GHz), i.e. the integral of the electric field according to Eqn. 11. Note that the transit time factor is included in V_T and V_L.

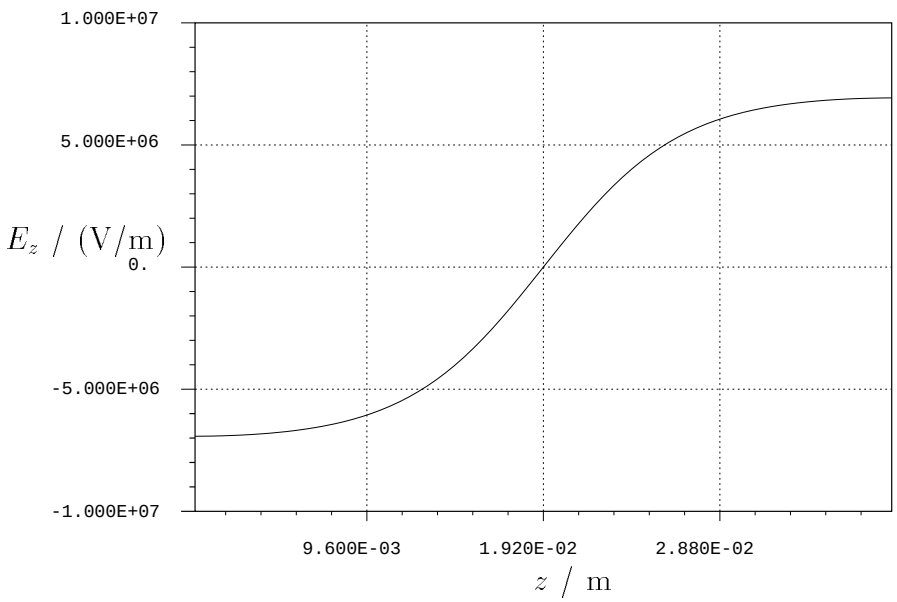

Figure 20: Longitudinal electric field (10 mm off axis) of the π-mode of cavity shape C15 at 5 MV/m transverse voltage.

5 End-cell Design

The results presented in the previous section are valid for infinite periodic structures or single cell cavities with shorting plates at both ends. If a beam pipe is connected to the cavity the field will be distorted resulting in a change in $(R/Q)'$, and the frequency is shifted. The goal is to re-tune the cavity by a variation of the end-cell geometry. The easiest way is to adjust the equator radius of the cell. The field in the end-cell will still be distorted but the field flatness of the other cells of the structure are hardly effected. Two different cavity shapes are considered: A15 and B19. While the cavity A15 can be easily re-tuned by a small change of the end-cell geometry it is much harder to re-tune the cavity of shape B19. Nevertheless it is interesting to study the effects of the end-cell for that somewhat extreme case. The re-tuning of cavity C15 is similar to A15. Appendix D shows an alternative end-cell design for cavity C15 which is especially well suited to mount a coupler.

The effects of the end-cells is studied by a one and one-half cell cavity geometry with a beam pipe as shown in Fig. 21 for a cavity of shape A15. At the left boundary of the cavity an electric boundary condition, corresponding to a shorting plate, is imposed for the numerical calculations with the MAFIA code. The results may also be interpreted as fields in a 3-cell cavity with a symmetry plane in the mid-cell. The values calculated for the transverse voltage, $(R/Q)'$ and the peak magnetic field are based on that symmetry condition. The longitudinal electric field at a fixed radius of the detuned cavity is shown in Fig. 22. The frequency of the detuned cavity is shifted by 13.6 MHz (shape A15) compared to the one-cell cavity with shorting plates. Within the resolution of the MAFIA grid the cavity is tuned back by a change of 0.4 mm of the equator radius of the end-cell of shape A15. The electric field and the longitudinal component of the electric field is shown in Fig. 23 and Fig. 24. The results for the design parameter are summarized in table 4.

A15	b /mm	f /GHz	$(R/Q)'$/cell /Ω	G_1 /Ω	B_{max}/T
periodic	47.19	3.8987	27.5	247	0.087
detuned	47.19	3.9123	24.3	249	0.116
tuned	47.59	3.8995	25.7	249	0.108

Table 4: MAFIA results for the cavity of shape A15. The case of a cavity with shorting plates and 3-cell cavities without and with tuned end-cells are presented. The magnetic field is calculated near the cavity surface (0.25 from the surface on the dual MAFIA mesh) for a transverse voltage of 5 MV/m.

The field of an end-cell reached only about 70 % of the field of a mid-cell, even after tuning (see Fig. 24). Therefore $(R/Q)'$/cell is smaller and B_{max} larger for a 3-cell cavity compared to the periodic case. This result is less relevant for a 13-cell cavity since the relative contribution of the end-cells to the mean transverse

voltage is significantly smaller, see the next section about multi-cell cavities. The field of the end-cell is almost 100 % of the field of a mid-cell for the alternative end-cell design for cavity C15 (see appendix D).

Cavity of shape A15 with an detuned end-cell.

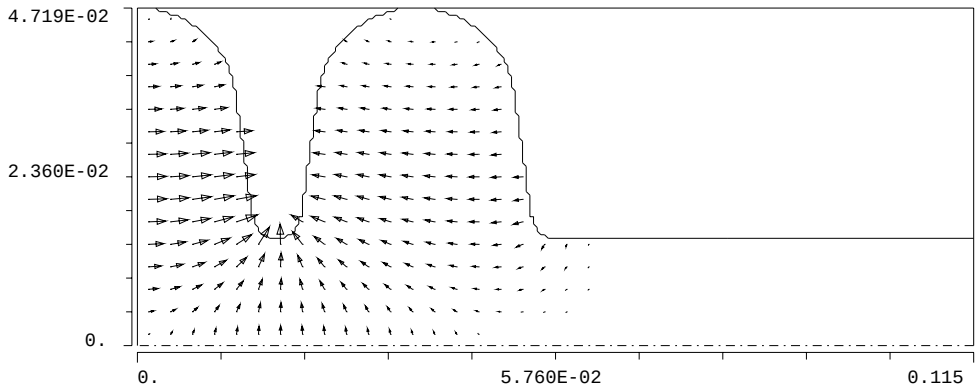

Figure 21: Cavity of shape A15 with an detuned end-cell ($f = 3.9123$ GHz). The electric field of the π-mode is shown.

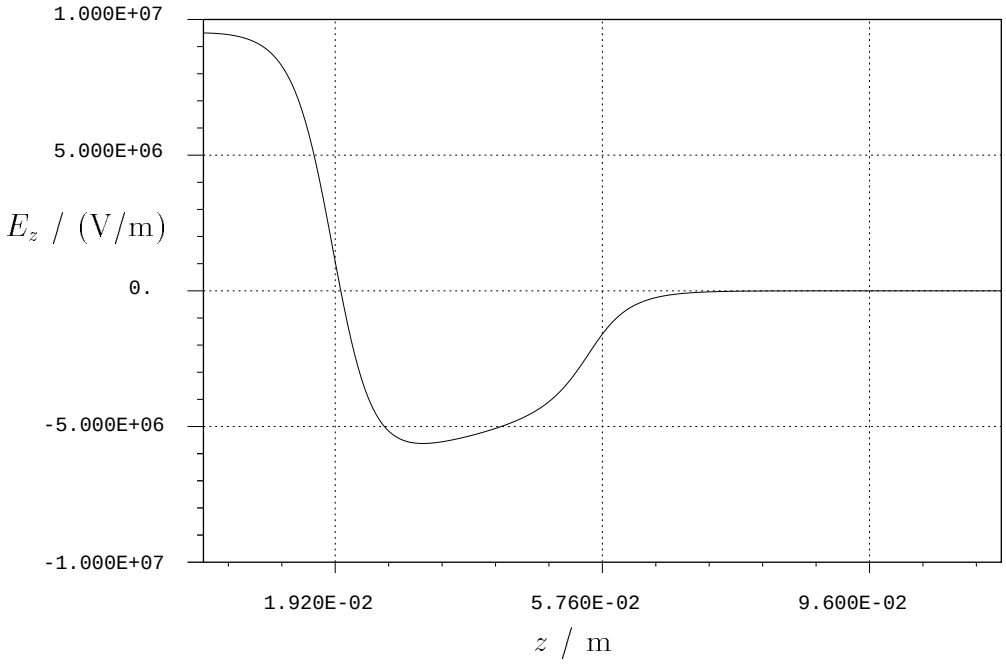

Figure 22: Cavity of shape A15 with a detuned end-cell ($f = 3.9123$ GHz). The longitudinal electric field of the π-mode at 5 MV/m transverse voltage is show at a fixed radius of 1 cm.

Cavity of shape A15 with a tuned end-cell.

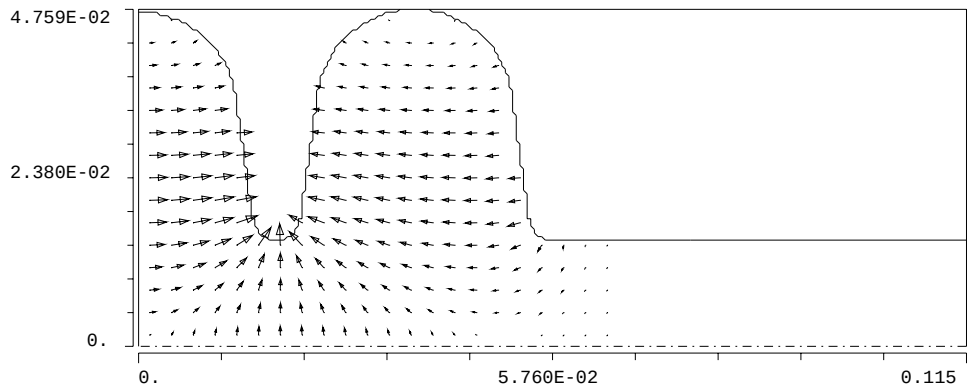

Figure 23: Cavity of shape A15 with a tuned end-cell (f = 3.8995 GHz). The electric field of the π-mode is shown.

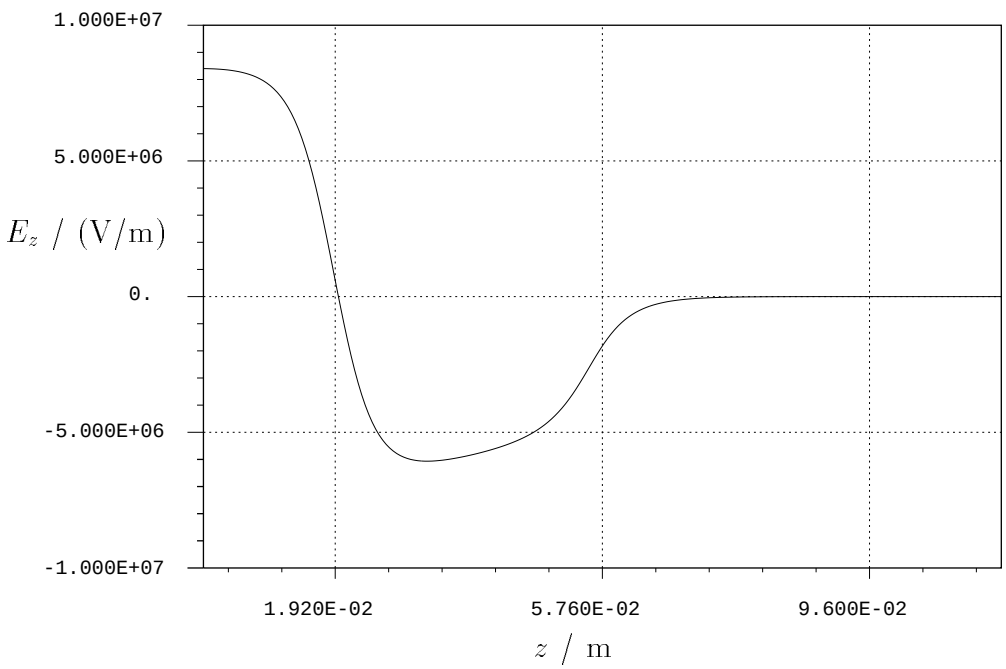

Figure 24: Cavity of shape A15 with a tuned end-cell (f = 3.8995 GHz). The longitudinal electric field of the π-mode at 5 MV/m transverse voltage is show at a fixed radius of 1 cm.

For a cavity of shape B19 the field of the end cell is significantly distorted due to the beam pipe. Fig. 25 shows the electric field of the distorted π-mode. The frequency of the detuned cavity is shifted by 52.6 MHz (shape B19) compared to the one-cell cavity with shorting plates. The cavity is tuned back by a change of 9.68 mm of the equator radius of the end-cell of shape B19. The electric field of the end cell is still distorted, see Fig. 26. The results for the cavity of shape B19 are summarized in table 5. From Fig. 27 it is obvious that the end-cell does practically not contribute to the field integral (see Eqn. (11)) and therefore to the kick. But this end-cell guarantees a good matching between the mid-cells and the beam pipe which will be shown in the next section for a 7-cell cavity. For the tuned 3-cell cavity one obtains $(R/Q)' = 15.69\,\Omega$, which results in a very small value per cell since the end-cells do not contribute.

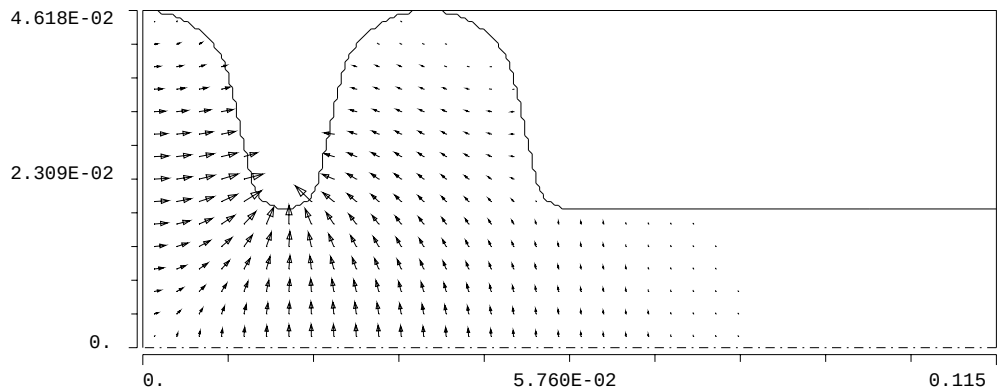

Figure 25: Cavity of shape B19 with a detuned end-cell ($f = 3.8398$ GHz). The electric field of the distorted π-mode is shown.

B19	b /mm	f /GHz	$(R/Q)'$/cell /Ω	G_1 /Ω	B_{max}/T
periodic	46.18	3.8924	18.6	231	0.096
detuned	46.18	3.8398	10.5	236	0.186
tuned	36.5	3.8881	5.23	246	0.245

Table 5: MAFIA results for the cavity of shape B19. The case of a cavity with shorting plates and 3-cell cavities without and with tuned end-cells are presented. The magnetic field is calculated near the cavity surface (0.25 from the surface on the dual MAFIA mesh) for a transverse voltage of 5 MV/m.

Cavity of shape B19 with a tuned end-cell.

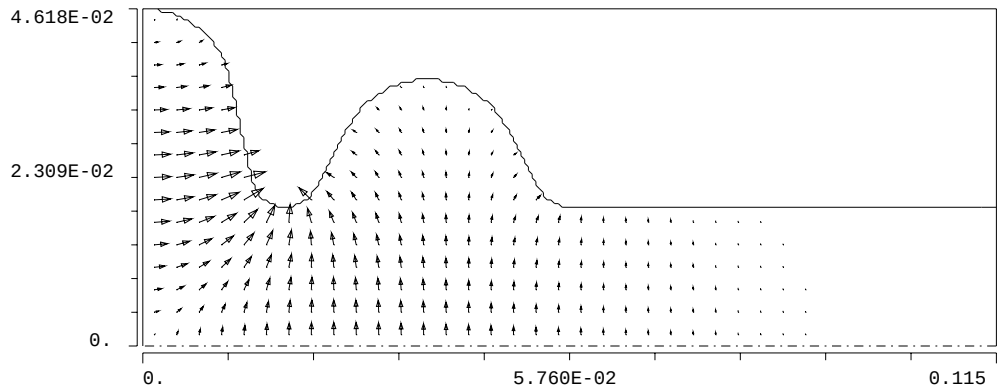

Figure 26: Cavity of shape B19 with a tuned end-cell (f = 3.8881 GHz). The electric field of the π-mode is shown.

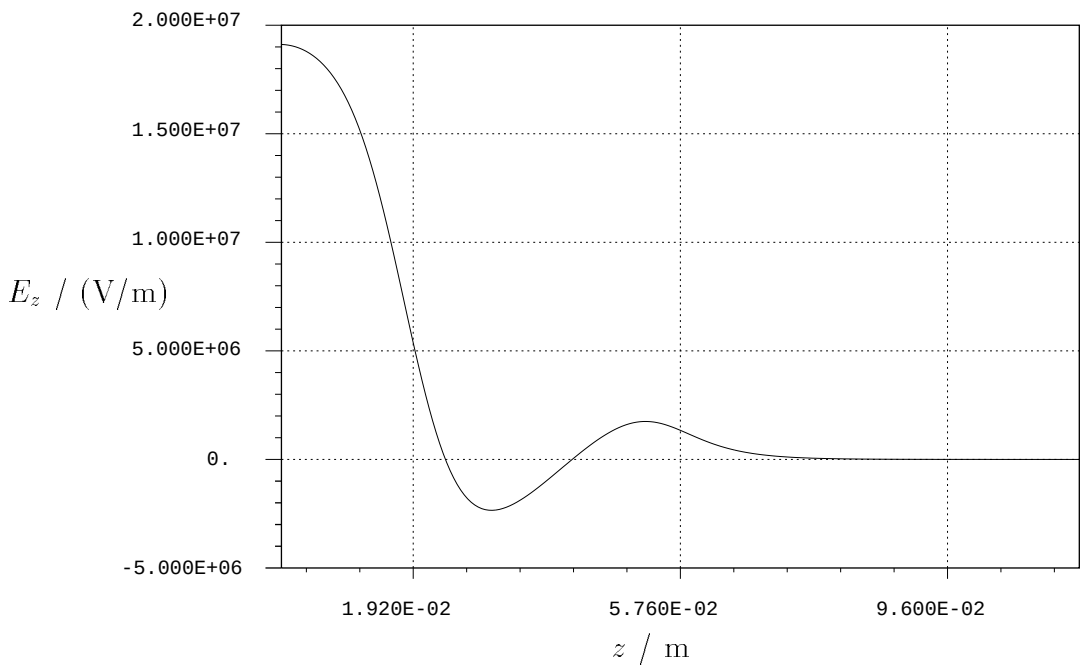

Figure 27: Cavity of shape B19 with a tuned end-cell (f = 3.8881 GHz). The longitudinal electric field of the π-mode at 5 MV/m transverse voltage is show at a fixed radius of 1 cm.

6 Multi-cell Results

The results from the previous section are now applied to a 7-cell and 13-cell of shape A15, a 7-cell cavity of shape B19 and a 13-cell cavity of shape C15. The goal is to investigate the field flatness of the π-mode and to determine the basic design parameters for these multi-cell cavities. Like in the previous section it is sufficient to study one half of the cavity with respect to a symmetry plane in the middle of the cavity (see Fig. 30). All modes are found if *electric (E)* or *magnetic (M)* boundary conditions are imposed at that symmetry plane using the MAFIA solver [2].

In a periodic structure the phase advance per cell φ is uniquely defined according to Eqn. 20. In a cavity with a finite number of cells a local phase advanced per cell can be defined. Using the following relations

$$\begin{aligned}
\widetilde{\boldsymbol{E}}^{(1)}(r,z)\ \exp(i\varphi) &= \widetilde{\boldsymbol{E}}^{(1)}(r,z+L_{cell}) \\
\widetilde{\boldsymbol{E}}^{(1)}(r,z)\ \exp(-i\varphi) &= \widetilde{\boldsymbol{E}}^{(1)}(r,z-L_{cell}) \\
2\ \widetilde{\boldsymbol{E}}^{(1)}(r,z)\ \cos(\varphi) &= \widetilde{\boldsymbol{E}}^{(1)}(r,z+L_{cell}) + \widetilde{\boldsymbol{E}}^{(1)}(r,z-L_{cell}),
\end{aligned} \tag{23}$$

which are strictly valid for a periodic structure, one can define a phase advance per cell at position z [9] as

$$\varphi(z) = \arccos\left(\frac{E_z^{(1)}(r,z+L_{cell}) + E_z^{(1)}(r,z-L_{cell})}{2\ E_z^{(1)}(r,z)}\right), \tag{24}$$

where $E_z^{(1)}(r,z)$ is the longitudinal electric field as calculated by MAFIA [2]. In the center cells of the cavities the above defined phase advance $\varphi(z)$ is almost independent from the longitudinal position z, which is demonstrated for a 7-cell cavity in the following section.

6.1 7-cell and 13-cell cavities of shape A15

The longitudinal electric field of the π-mode is shown in Fig. 28 for a 7-cell cavity of shape A15. The corresponding plot of the electric field is shown in Fig. 30, while the MAFIA results for the design parameter are summarized in table 6. Furthermore plots of the modes with the lowest frequency of the first dipole passband are show in Fig. 31 to Fig. 36. The frequency, $(R/Q)'$, G_1 of each mode are given in the caption below each plot. Furthermore the boundary conditions (b.cond.) are mentioned. E.g. *ME* means *magnetic (M)* boundary conditions at the left boundary (symmetry plane) and *electric (E)* at the end of the beam pipe. The phase advance per cell is 180° (or π) for the mode shown in Fig. 30, while the phase advance per cell is 148°, 120° ... 14° for the modes shown in Fig. 31 to Fig. 36. The frequencies of these modes are shown together with the dispersion curve of the first dipole passband of cavity A15 in Fig. 37. The phase advance

of the modes has been calculated according to Eqn. 24 for $z = 0.2 \cdot L_{cell}$. Fig. 29 shows the local phase advance $\varphi(z)$ of the π-mode. The phase advance per cell for that mode is actually 172° in the center cell ($|z| < L_{cell}/2$). The influence of the end cells is clearly visible in the graph but the local phase advance $\varphi(z)$ is remarkably constant within the three center cells ($|z| < 1.5 \cdot L_{cell}$. The local phase advance is singular at the zeros of the longitudinal field $E_z^{(1)}(r, z)$. The quoted value for the phase advance of the modes in Fig. 31 to Fig. 36 is always the local phase advance of the center cell ($z = 0.2 \cdot L_{cell}$, some modes have zero electric field at $z = 0$), well away from any singularity.

A15	b /mm	f /GHz	$(R/Q)'$/cell /Ω	G_1 /Ω	B_{max}/T
periodic	47.19	3.8987	27.5	247	0.087
7-cell	47.19 (47.59)	3.8987	26.5	248	0.098
13-cell	47.19 (47.59)	3.8988	26.8	247	0.097

Table 6: MAFIA results for the cavity of shape A15. The case of a cavity with shorting plates, a 7-cell cavity and a 13-cell cavity with tuned end-cells are presented. The magnetic field is calculated near the cavity surface (0.25 from the surface on the dual MAFIA mesh) for a transverse voltage of 5 MV/m. The radius b is given for a mid-(end-)cell.

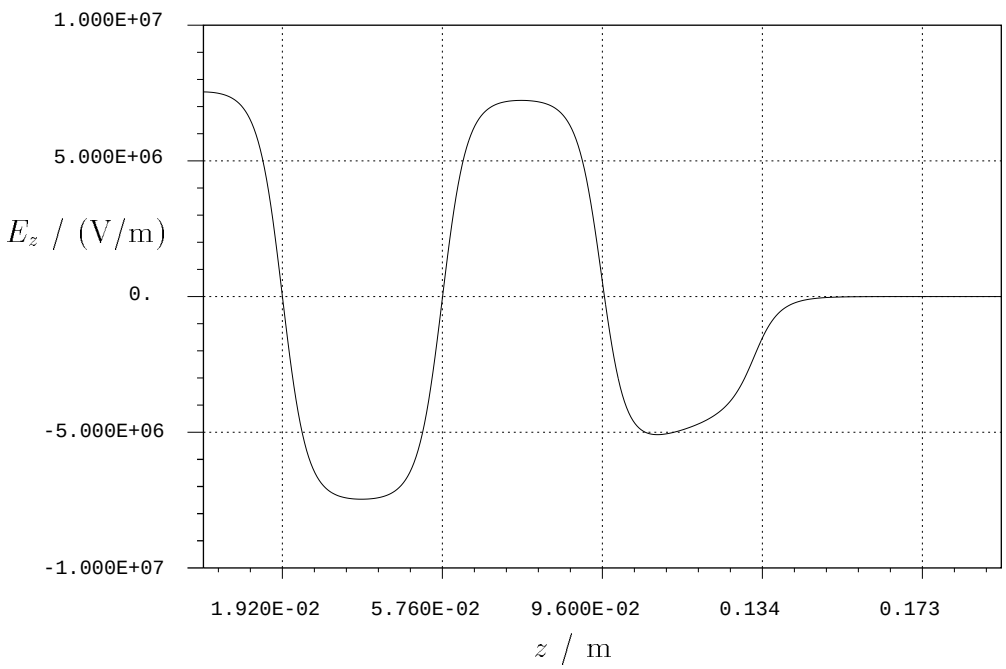

Figure 28: 7-cell cavity of shape A15 with a tuned end-cell (f = 3.8987 GHz). The longitudinal electric field of the π-mode at 5 MV/m transverse voltage is show at a fixed radius of 1 cm.

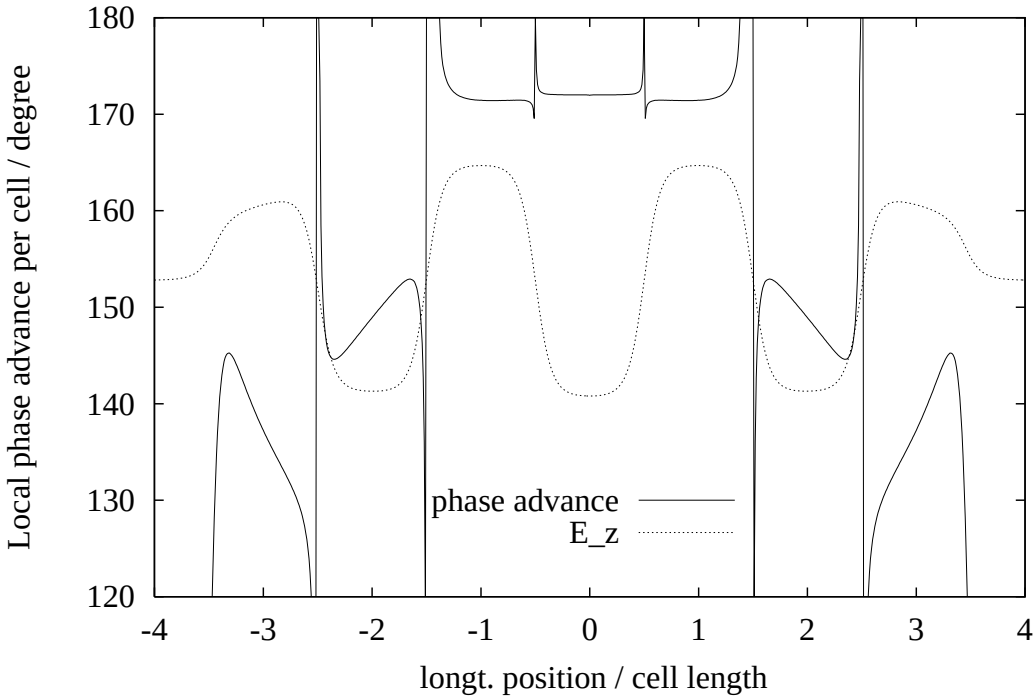

Figure 29: 7-cell cavity of shape A15 with a tuned end-cell. The solid line shows the local phase advance $\varphi(z)$ of the π-mode ($f = 3.8987$ GHz), while the dashed line presents the longitudinal electric field at a fixed radius of 1 cm in arbitrary units. The symmetry condition at $z = 0$ has been used to supplement the electric field values for $z < 0$.

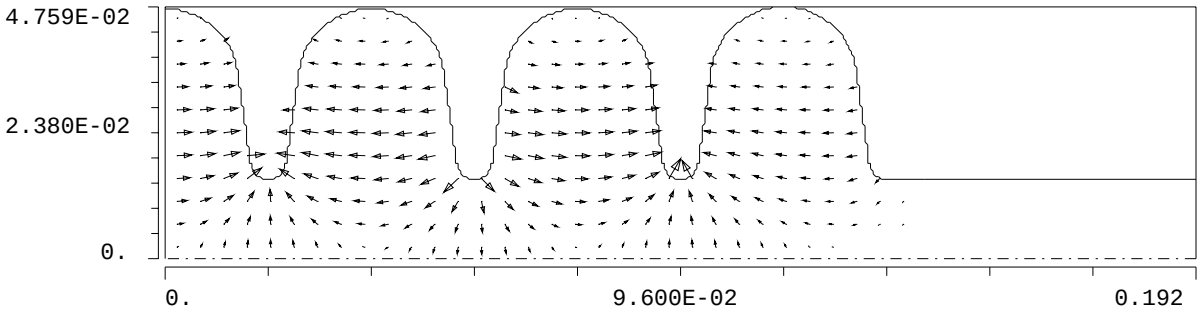

Figure 30: 7-cell cavity of shape A15, electric field of the mode $f = 3.8987$ GHz (b.cond. EE), $(R/Q)' = 185.5\ \Omega$, $G_1 = 248\ \Omega$; phase advance $\varphi = 172°$.

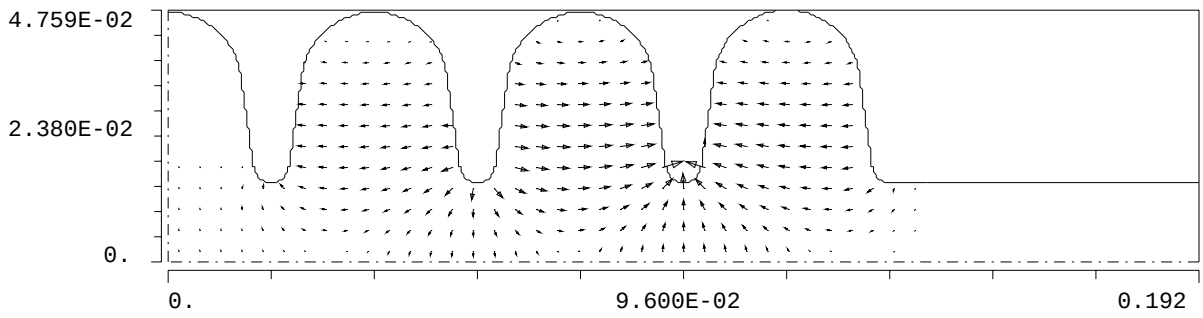

Figure 31: 7-cell cavity of shape A15, electric field of the mode $f = 3.9029$ GHz (b.cond. *ME*), $(R/Q)' = 0.02\ \Omega$, $G_1 = 249\ \Omega$; phase advance $\varphi = 148°$.

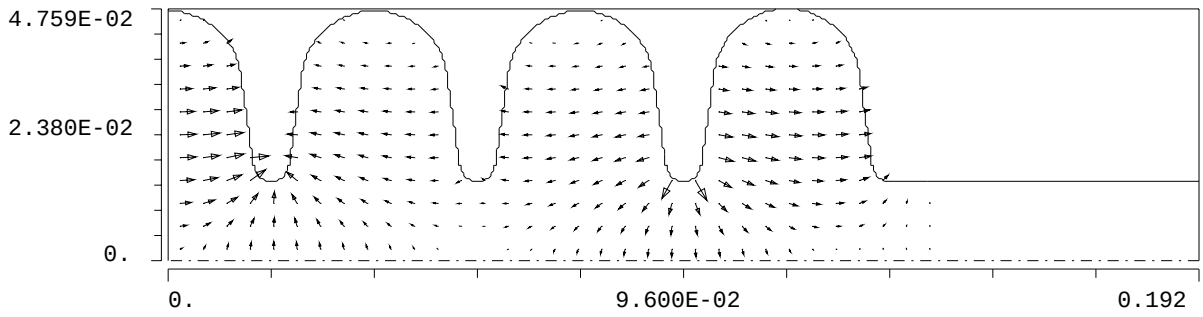

Figure 32: 7-cell cavity of shape A15, electric field of the mode $f = 3.9146$ GHz (b.cond. *EE*), $(R/Q)' = 1.9\ \Omega$, $G_1 = 251\ \Omega$; phase advance $\varphi = 120°$.

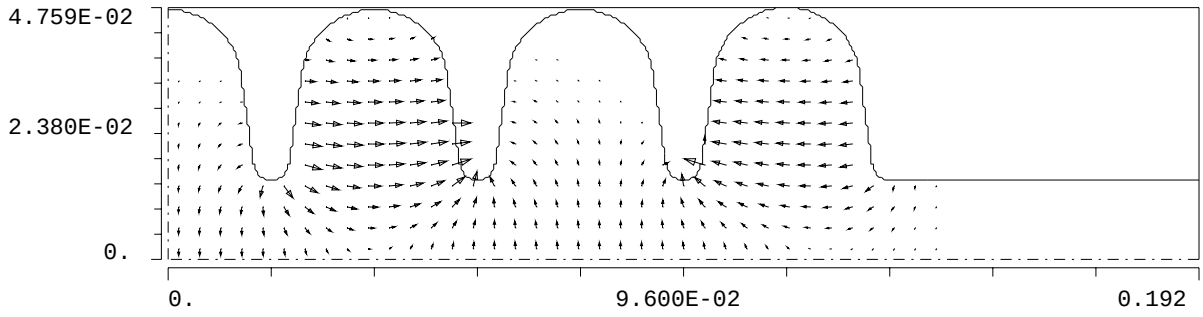

Figure 33: 7-cell cavity of shape A15, electric field of the mode $f = 3.9360$ GHz (b.cond. *ME*), $(R/Q)' = 0.14\ \Omega$, $G_1 = 256\ \Omega$; phase advance $\varphi = 91°$.

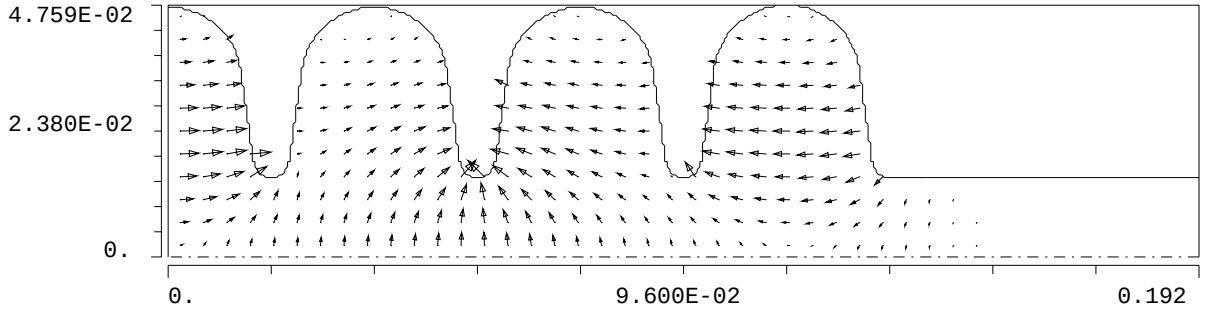

Figure 34: 7-cell cavity of shape A15, electric field of the mode $f = 3.9696$ GHz (b.cond. *EE*), $(R/Q)' = 1.2\ \Omega$, $G_1 = 264\ \Omega$; phase advance $\varphi = 64°$.

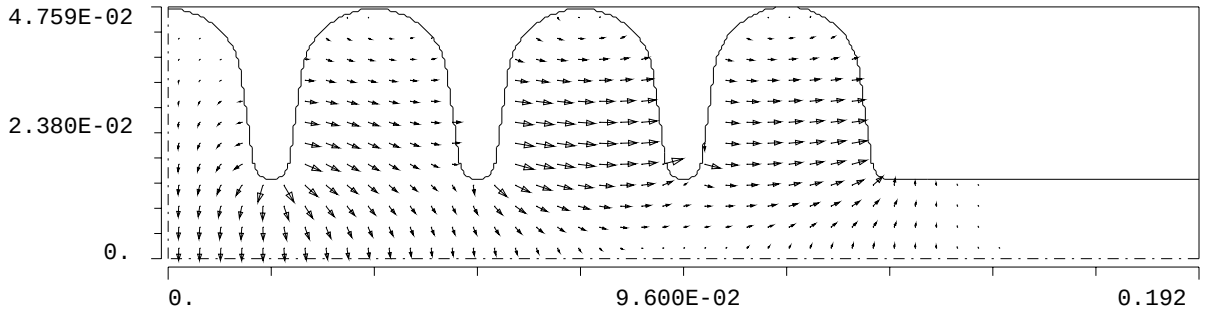

Figure 35: 7-cell cavity of shape A15, electric field of the mode $f = 4.0173$ GHz (b.cond. *ME*), $(R/Q)' = 0.49\ \Omega$, $G_1 = 279\ \Omega$; phase advance $\varphi = 37°$.

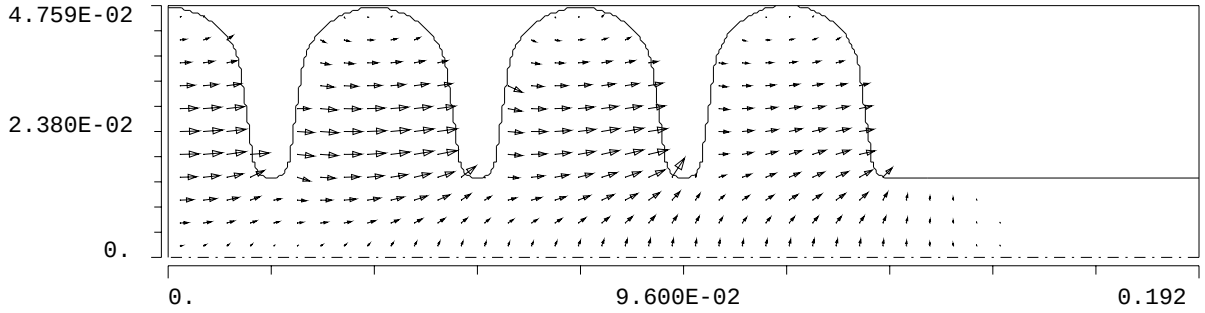

Figure 36: 7-cell cavity of shape A15, electric field of the mode $f = 4.0735$ GHz (b.cond. *EE*), $(R/Q)' = 0.39\ \Omega$, $G_1 = 311\ \Omega$; phase advance $\varphi = 14°$.

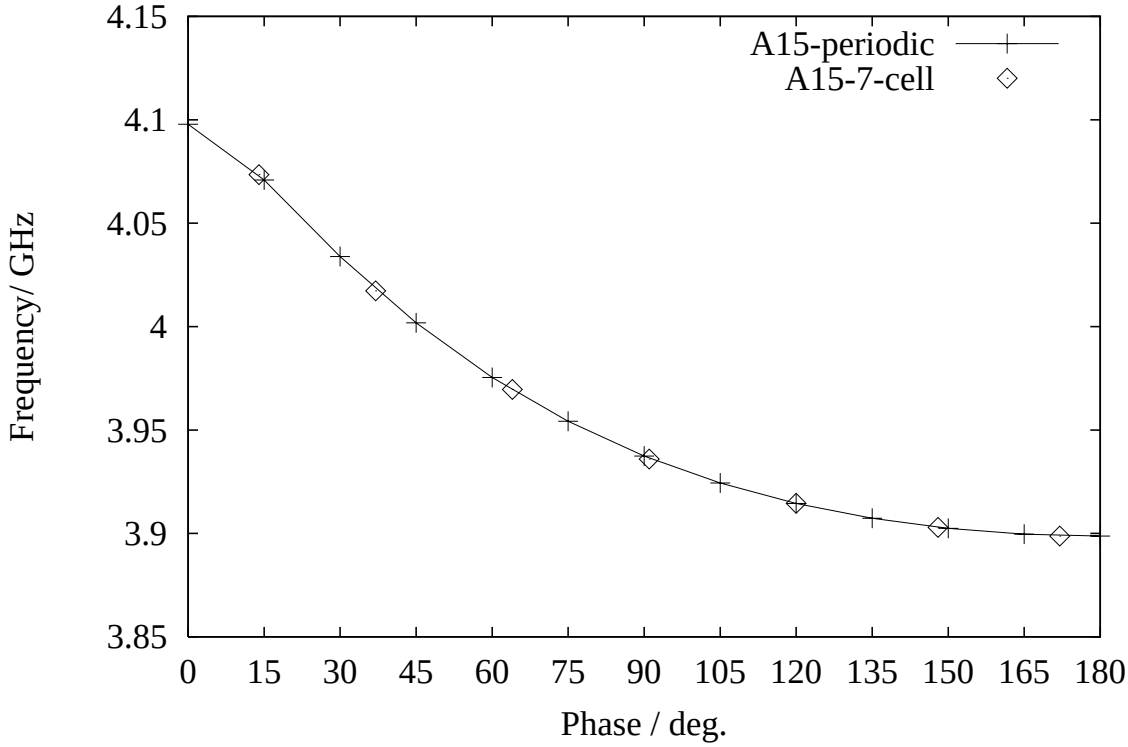

Figure 37: Dispersion curve of the first dipole passband of a cavity of shape A15: the solid line shows the results obtained for an infinite periodic structure (see also Fig. 14), while the points marked with diamonds represents the modes obtained from a 7-cell cavity using the calculated local phase advance of the center cell as an abscissa.

The electric field of the π-mode of a **13-cell cavity of shape A15** is shown in Fig. 39. The longitudinal component is shown separately in Fig. 38 to demonstrate the achieved field-flatness.

The frequency of the $12\pi/13$-mode (often also called the $\pi - 1$-mode) differs only by 1 MHz (or $-2.56 \cdot 10^{-4}$) from the π-mode frequency. The electric field of that mode is show in Fig. 40. The tuning of the π-mode of a warm Niobium cavity seems to be difficult since the field distribution of the $\pi - 1$-mode is similar to the π-mode in the four cells at the ends of cavity and the frequencies differ only by 1 MHz. Further plots of the other modes of a 13-cell cavity are not shown since the 7-cell results already demonstrate the field pattern in principle.

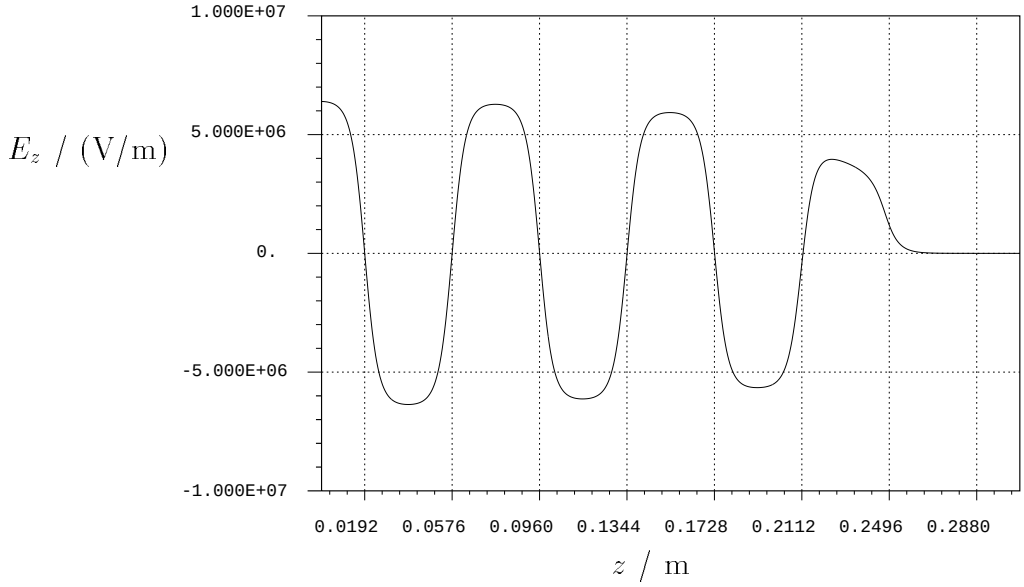

Figure 38: 13-cell cavity of shape A15 with a tuned end-cell ($f = 3.8987$ GHz). The longitudinal electric field of the π-mode at 5 MV/m transverse voltage is show at a fixed radius of 1 cm.

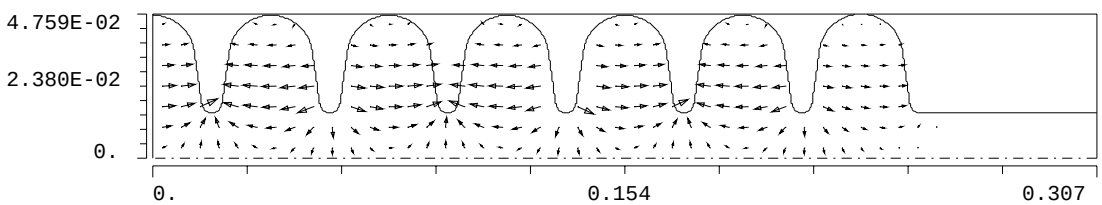

Figure 39: 13-cell cavity of shape A15, electric field of the π-mode $f = 3.8988$ GHz (b.cond. EE), $(R/Q)' = 349.1\ \Omega$, $G_1 = 247\ \Omega$.

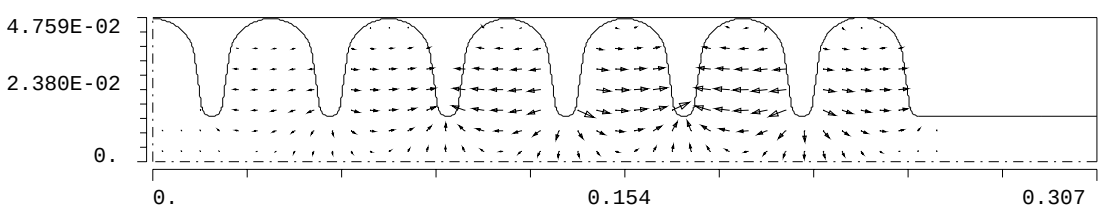

Figure 40: 13-cell cavity of shape A15, electric field of the mode $f = 3.8998$ GHz (b.cond. EE), $(R/Q)' = 0.01\ \Omega$, $G_1 = 247\ \Omega$; corresponds to a $12\,\pi/13$-mode (or "$\pi - 1$-mode").

6.2 7-cell cavity of shape B19

Furthermore, results for a **7-cell cavity of shape B19** are presented. This type of cavity with strongly coupled cells require a significant change of the geometry of the end-cell to re-tune it. Nevertheless a good field-flatness of the π-mode can be achieved. A plot of the electric field of that mode is shown in Fig. 47 and the main design parameter are summarized in table 7. The longitudinal electric field is shown in Fig. 41 to demonstrated the field-flatness in the inner cells. All

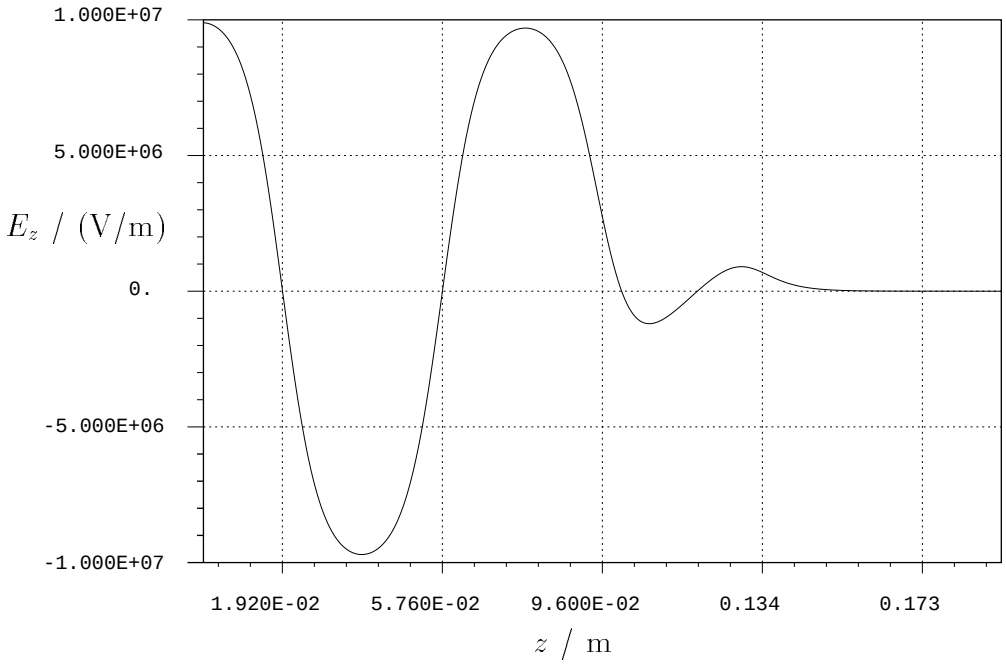

Figure 41: 7-cell cavity of shape B19 with a tuned end-cell (f = 3.8912 GHz). The longitudinal electric field of the π-mode at 5 MV/m transverse voltage is show at a fixed radius of 1 cm.

modes of the first dipole mode passband and the 0-mode of the second passband are show in Fig. 42 to Fig. 48. The frequency, $(R/Q)'$, G_1 of each mode can be found in the caption of the figures. There are only six modes in the first dipole passband. Some modes look more like TE-modes while others look more like TM-modes.

B19	b /mm	f /GHz	$(R/Q)'$/cell /Ω	G_1 /Ω	B_{max}/T
periodic	46.18	3.8924	18.6	231	0.096
7-cell	46.18 (36.5)	3.8911	12.7	235	0.133

Table 7: MAFIA results for the cavity of shape B19. The case of a cavity with shorting plates and a 7-cell cavities with tuned end-cells are presented. The value of $(R/Q)'$/cell is smaller for the 7-cell cavities compared to the periodic case since the end-cell do not contribute to the transverse voltage. The magnetic field is calculated near the cavity surface (0.25 from the surface on the dual MAFIA mesh) for a transverse voltage of 5 MV/m.

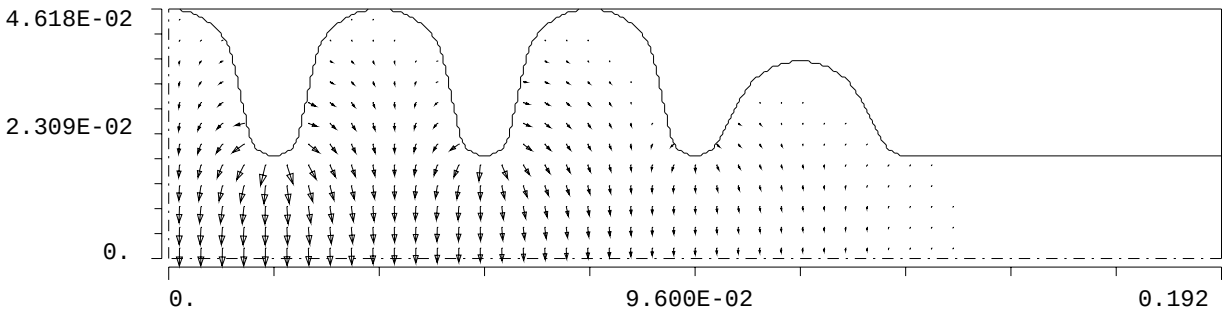

Figure 42: 7-cell cavity of shape B19, electric field of the mode $f = 3.6483$ GHz (b.cond. *ME*), $(R/Q)' = 0.01\ \Omega$, $G_1 = 242\ \Omega$.

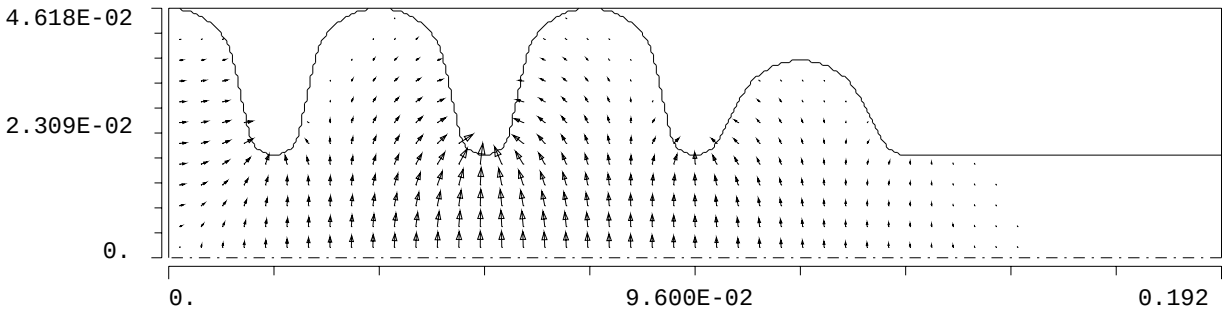

Figure 43: 7-cell cavity of shape B19, electric field of the mode $f = 3.7109$ GHz (b.cond. *EE*), $(R/Q)' = 0.58\ \Omega$, $G_1 = 245\ \Omega$.

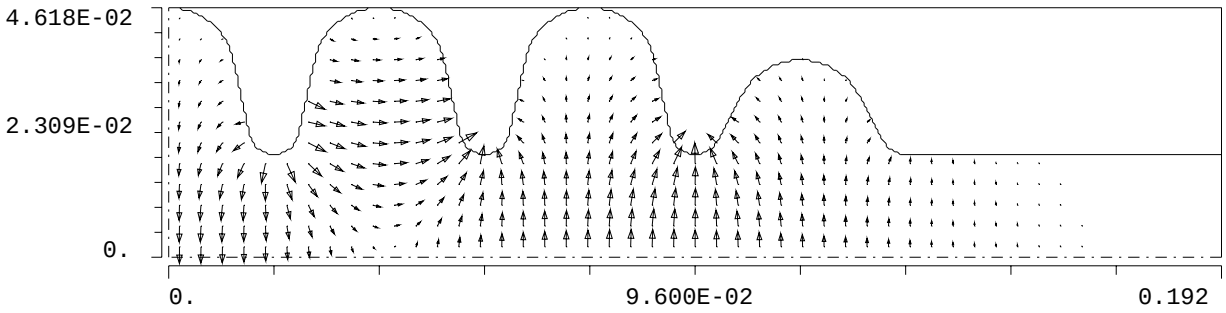

Figure 44: 7-cell cavity of shape B19, electric field of the mode $f = 3.7857$ GHz (b.cond. *ME*), $(R/Q)' = 0.05\ \Omega$, $G_1 = 245\ \Omega$.

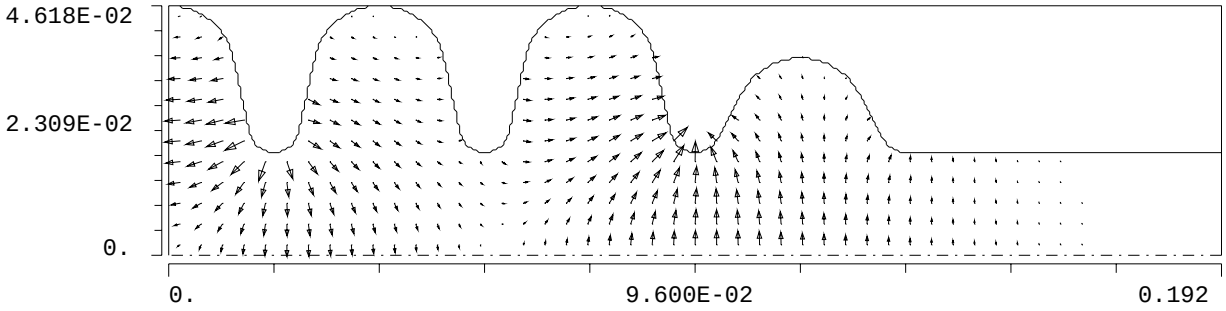

Figure 45: 7-cell cavity of shape B19, electric field of the mode $f = 3.8453$ GHz (b.cond. *EE*), $(R/Q)' = 0.95\ \Omega$, $G_1 = 243\ \Omega$.

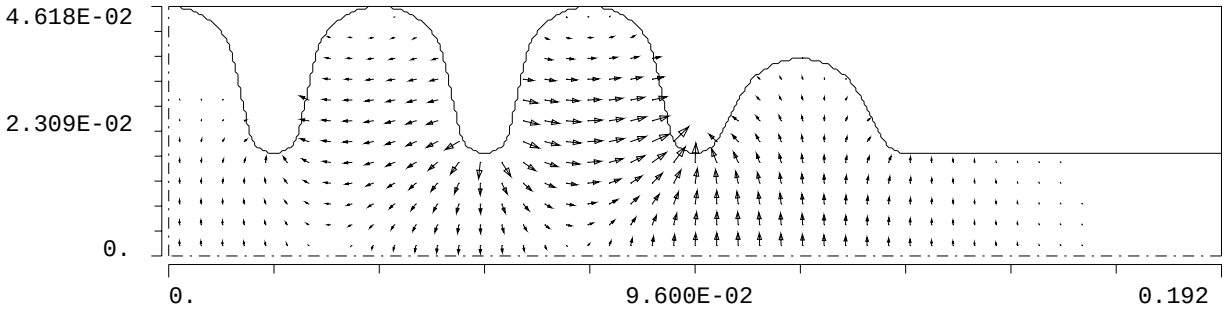

Figure 46: 7-cell cavity of shape B19, electric field of the mode $f = 3.8792$ GHz (b.cond. *ME*), $(R/Q)' = 0.26\ \Omega$, $G_1 = 240\ \Omega$.

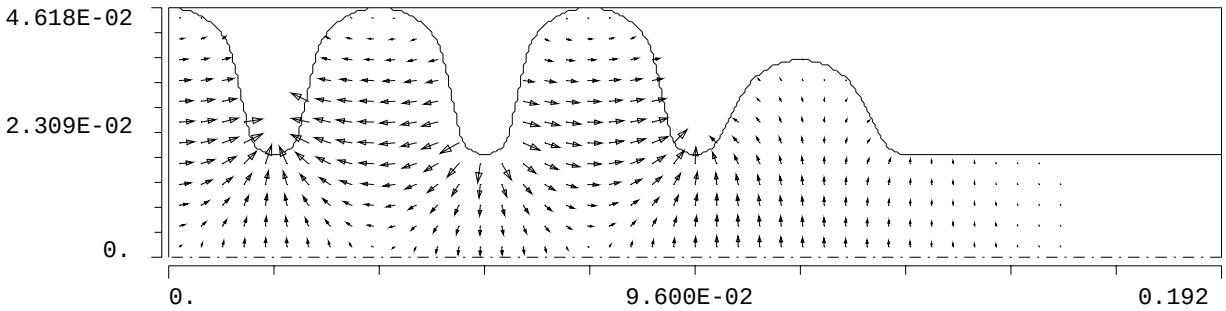

Figure 47: 7-cell cavity of shape B19, electric field of the mode $f = 3.8911$ GHz (b.cond. EE), $(R/Q)' = 89.0\ \Omega$, $G_1 = 235\ \Omega$ (π-mode).

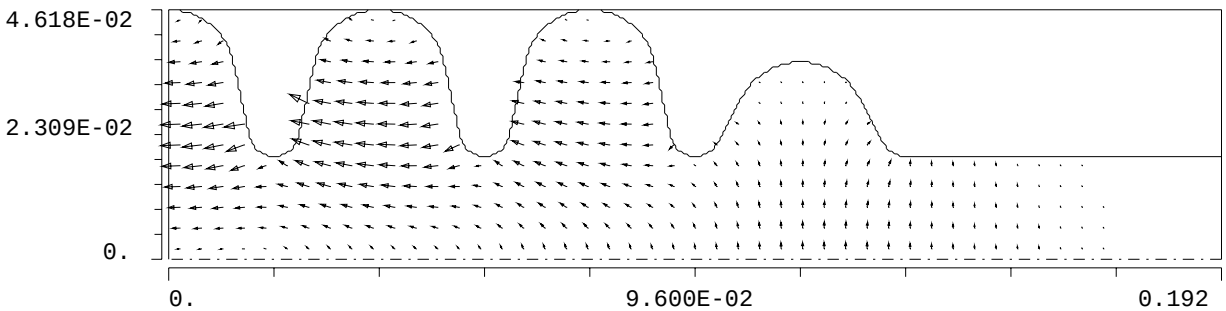

Figure 48: 7-cell cavity of shape B19, electric field of the mode $f = 4.2387$ GHz (b.cond. EE), $(R/Q)' = 0.08\ \Omega$, $G_1 = 328\ \Omega$. First mode from the second passband.

6.3 13-cell cavity of shape C15

The field pattern of a cavity of shape C15 are similar to the pattern obtained for a A15 cavity. The electric field of the π-mode of a 13-cell cavity of shape C15 is shown in Fig. 50 and the main design parameter are summarized in table 8. The end-cell has been tuned by an increase of the equator radius by 0.37 mm. The longitudinal component of the electric field 10 mm off axis is shown separately in Fig. 49 to demonstrate the achieved field-flatness. A complete list of all modes of the first dipole passband can be found in appendix C. The frequency of the $\pi - 1$-mode differs by 1.2 MHz (or $-3.04 \cdot 10^{-4}$) from the π-mode frequency. The tuning of the π-mode of a warm Niobium cavity seems to be still difficult but probably just possible. The selection of the C15 cavity shape seems best as the modification of the end cell radius is minimal (compared to B19) and the modes of the passband behave in a predictable way (all modes are TM-like modes). Results for the cavity C15 with an alternative end-cell design are shown in appendix D.

The phase advance of each mode has been calculated according to Eqn. 24 in the center cell for $z = 0.2 \cdot L_{cell}$. The frequencies of all modes from the first

dipole passband are shown together with the dispersion curve of the first dipole passband of cavity C15 in Fig. 51.

C15	b /mm	f /GHz	$(R/Q)'$/cell /Ω	G_1 /Ω	B_{max}/T
periodic	47.18	3.8997	27.3	228	0.073
13-cell	47.18 (47.55)	3.8998	27.0	228	0.077

Table 8: MAFIA results for the cavity of shape C15. The case of a cavity with shorting plates, and a 13-cell cavity with tuned end-cells are presented. The magnetic field is calculated near the cavity surface (0.25 from the surface on the dual MAFIA mesh) for a transverse voltage of 5 MV/m. The radius b is given for a mid-(end-)cell.

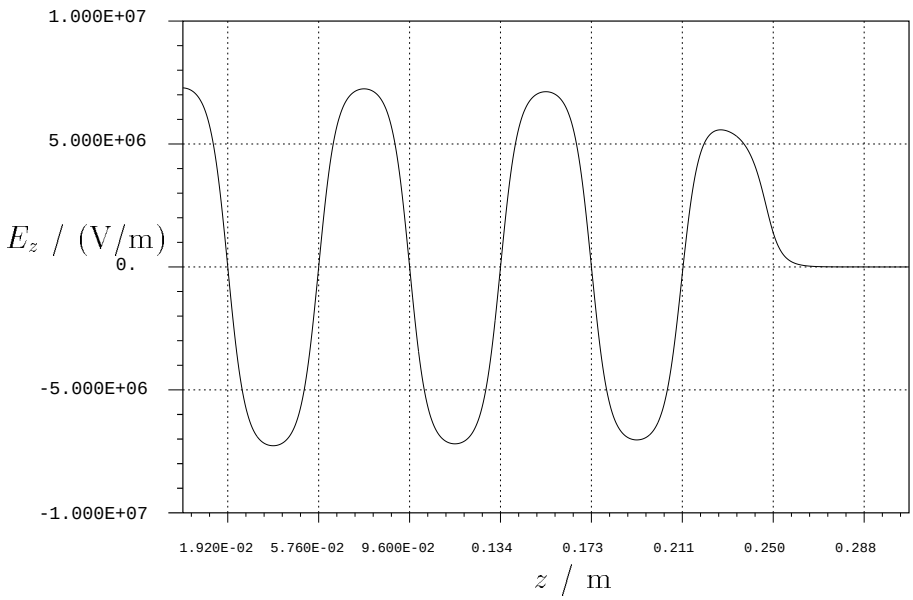

Figure 49: 13-cell cavity of shape C15 with a tuned end-cell (f = 3.8998 GHz). The longitudinal electric field of the π-mode at 5 MV/m transverse voltage is show at a fixed radius of 1 cm.

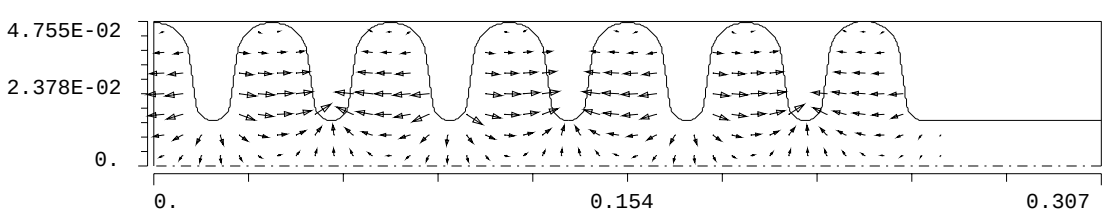

Figure 50: 13-cell cavity of shape C15, electric field of the mode f = 3.8998 GHz (b.cond. EE), $(R/Q)'$ = 351 Ω, G_1 = 228 Ω; phase advance $\varphi = 177°$ (π-mode).

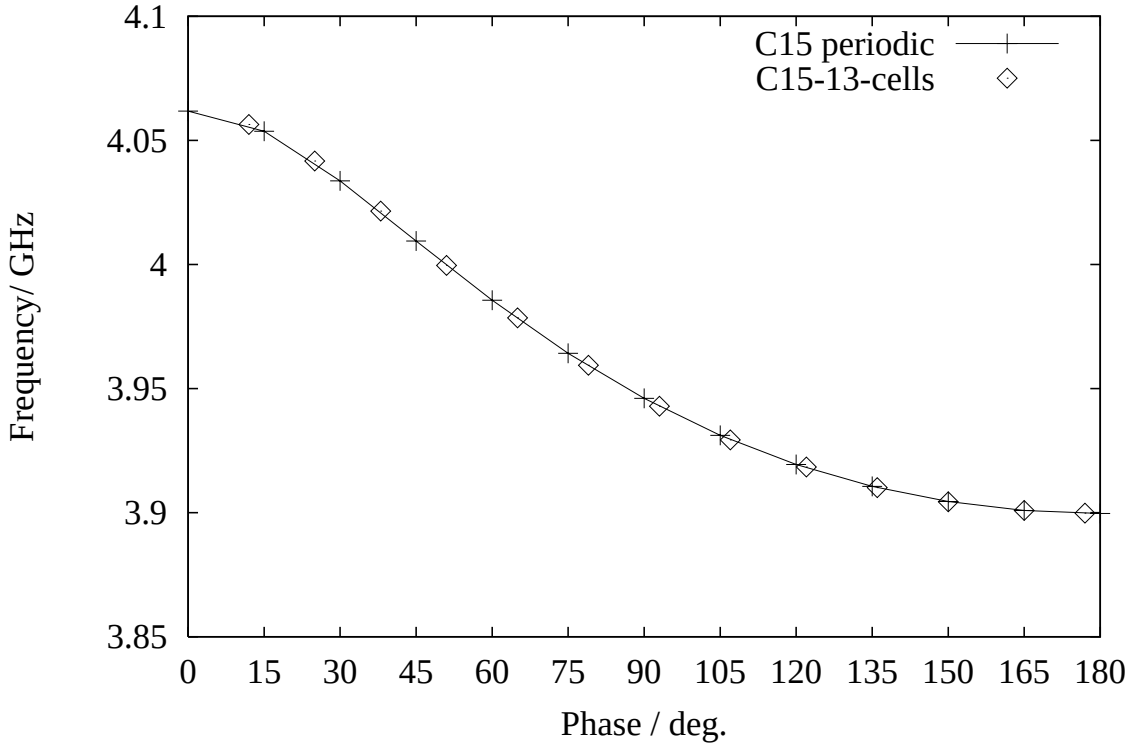

Figure 51: Dispersion curve of the first dipole passband of a cavity of shape C15: the solid line shows the results obtained for an infinite periodic structure, while the points marked with diamonds represents the modes obtained from a 13-cell cavity using the calculated local phase advance of the center cell as an abscissa.

7 Equivalent-Circuit Modeling of Transverse-Mode Structures

7.1 Introduction

From the earliest days of microwave technology lumped equivalent circuit models for extended resonant structures have been used to define relevant parameters and aid intuition in device design [10]. The modeling of accelerator structures by chains of coupled lumped-circuit tanks [11, 12] has become an essential tool of linac design [13]. For superconducting linacs short, standing-wave structures operating in the π-mode have become the norm [14]. In the realization of these systems, equivalent circuit models are employed in modeling power flow and structure filling [16, 17], and most importantly they are used in tuning the individual cells of the π-mode structure to improve cell-to-cell field flatness and to minimize peak fields [14, 18]. This tuning process involves bead pulling to measure a field profile and from this calculation of a vector of corrections to cell frequencies.

In making the step from superconducting linac to a superconducting deflection system for particle separation many issues are involved. These are discussed in a previous paper [1]. and the argument is made to retain the architecture of short, π-mode deflectors. Because in the transverse modes the peak magnetic field is the limiting factor in the achievable deflecting gradient, tuning will remain an essential step in producing structures with good performance. Therefore it is necessary to know about any candidate deflecting structure design how its fields can be well enough understood for bead measurements to be reliably interpreted and accurately enough modeled to allow a reasonably efficient tuning procedure.

In an accelerating structure the TE-like modes of the deflecting band lie lower in frequency than the TM-like modes, but in the deflecting structure with π-mode length cells, the opposite is true, and the TM-like band is the lower of the two. In the strongly-coupled regime, the deflection band is of the forward-wave type, with the π-mode at the high-frequency end of the band, and in the weakly-coupled regime the deflection band has a backward wave, and the π-mode is the lowest frequency in the TM band [1]. The progression from one regime to the other is illustrated in Figure 14 above. Cells of shape A13 and A15 are of backward wave type; and cells of shape A19 and A25 are of forward wave type. Cell A17 though of forward wave type is near to the dividing line.

7.2 Equivalent-Circuit Modeling of the Forward-Wave Deflection Structure

Appendix B.1 of this document shows arrow plots of E-field for the lowest 8 modes of a uniform 7-cell structure with beam pipes the same diameter as the cell irises. The cells in this structure have the shape B19. Mafia orders modes by

frequency, and the modes are classed by the boundary conditions and numbered by frequency. Thus the lowest mode, Figure 58, has a magnetic boundary on the left, an electric boundary on the right, is the first such mode, and is designated ME-1. The lowest two modes, Figures 58 and 59 , appear to have a transverse electric character. The second two of the modes, Figures 60 and 61, have both transverse and longitudinal electric fields. The third pair of the modes, Figures 62 and 63, have predominately longitudinal electric fields in the cells and transverse fields in the irises, which is characteristic of TM modes with large phase shift per cell. And in fact the sixth mode, EE-3, is the π-like mode appropriate for particle deflection.

The mode illustrated in Figure 64 is one of a pair of beam-pipe modes not clearly a part of the TEM bands. The mode of Figure 65 can be taken as the lowest mode of the second TEM passband which has eight modes. The frequencies of the first seven TEM modes are given in Appendix B.2. Higher modes in this passband leak into the beam pipe and so are not strictly characteristic of the structure.

It is difficult to understand the complicated structure of the modes of the first passband of this structure in the same terms that apply to a single, isolated band, and the models that have been applied to accelerator structures do not work for this case. A model for the deflection modes of the NLC waveguide by Bane and Gluckstern [6] can, however, be successfully applied.

This model includes two chains of coupled resonant circuits that are inter cross coupled at each iris. One of these chains models the coupled TM modes of the structure, and the other the coupled TE modes. In addition, the two chains are coupled by means of the fields associated with the iris which are common to both TM and TE branches.

The circuit equation for the nth cell of this model is written in the author's notation:

$$
\begin{aligned}
(x-\lambda)\, f_m - \frac{\kappa}{2}\, f_{m+1} - \frac{\kappa}{2}\, f_{m-1} &= -\frac{\sqrt{\kappa\hat{\kappa}}}{2}\, \hat{f}_{m+1} + \frac{\sqrt{\kappa\hat{\kappa}}}{2} \hat{f}_{m-1} \\
(\hat{x}-\lambda)\, \hat{f}_m - \frac{\hat{\kappa}}{2}\, \hat{f}_{m+1} - \frac{\hat{\kappa}}{2}\, \hat{f}_{m-1} &= \frac{\sqrt{\kappa\hat{\kappa}}}{2}\, f_{m+1} - \frac{\sqrt{\kappa\hat{\kappa}}}{2}\, f_{m-1}
\end{aligned}
\tag{25}
$$

Here the quantities are:

$f,\ \hat{f}$	amplitude variables
$\lambda = \frac{1}{\nu^2}$	eigenvalue
ν	frequency, GHz
$x,\ \hat{x} = \frac{1}{\nu_c^2},\ \frac{1}{\hat{\nu}_c^2}$	where $\nu_c,\ \hat{\nu}_c = \frac{1}{2\pi\sqrt{LC}},\ \frac{1}{2\pi\sqrt{\hat{L}\,\hat{C}}}$
$\kappa,\ \hat{\kappa}$	intra-chain coupling factors
$\sqrt{\kappa\hat{\kappa}}$	inter-chain coupling factor

The quantity ν_c is the unloaded frequency of the model cell with capacitance C and inductance L.

The left-hand side of these equations are the circuit equations for two chains of resonators. In the right-hand sides the cross coupling between the chains is introduced. The demonstration that the cross-coupling factor must have the form in these equations is the authors major result. This paper deals with a structure that is both tapered and detuned for the deflection modes, and the x and κ and their hatted equivalents vary along the cavity chain and so are indexed along with the amplitudes. For this application it is more convenient to treat these quantities as constants and enter adjustments to their value explicitly into the system matrix.

In Appendix B.3 below the system matrix is written down from Equation 25 for a 7-cell structure terminated in whole cells, following Bane and Gluckstern's prescription for the boundary conditions. Both chains are made antisymmetric with respect to the iris at each end of the structure. The quantities γ and $\hat{\gamma}$ are corrections to the frequency of the end cells for the impedance of the beam pipe [14] which is connected at these last irises. Written in this form the gamma are related to cell frequency as indicated in Equation 24. MAFIA simulations on a single cell of B19 shape shows that the beam pipe raises the TM mode in the cell by something just under 70 MHz and lowers TE mode by about 3 times that amount. This provides estimates for the gamma which are also shown in Equation 26.

$$\frac{\Delta\nu}{\nu} = -\frac{\gamma}{2} \approx .0175 \quad \text{and} \quad \Delta\hat{\nu} \approx -3\,\Delta\nu \quad \text{or} \quad \hat{\gamma} = -3\,\gamma\sqrt{\frac{\hat{x}}{x}} \tag{26}$$

The paper also shows that for the double chain equations in Equation 25, the dispersion curve is given by the quadratic:

$$\begin{aligned} \lambda^1 &= b + \sqrt{b^2 - c} \;\text{ where }\; b = \frac{1}{2}\left(x + \hat{x} + (\hat{\kappa} - \kappa)\cos\phi\right) \\ \lambda^2 &= b - \sqrt{b^2 - c} \;\text{ and where }\; c = x\hat{x} - \kappa\hat{\kappa} + (x\hat{\kappa} - \hat{x}\kappa)\cos\phi \end{aligned} \tag{27}$$

Here ϕ is the phase shift per cell and as above $\lambda = 1/\nu^2$, the two branches of the solution being indicated by the superscripts. These dispersion curves can be found in MAFIA from single-cavity calculations with periodic boundary conditions. If frequencies are found for the lowest two modes with dipole symmetry at two values of the phase shift, say 0 and 180 degrees, then Equation 27 can be solved for values for the four model constants,x and κ both hatted and unhatted. There are four such solutions. Two are written below. The other two are the same with branches 1 and 2 interchanged.

$$
\begin{array}{ll}
\text{Solution 1} & \text{Solution 2} \\
x = \frac{1}{2}\left(\lambda_\pi^1 + \lambda_0^2\right) & x = \frac{1}{2}\left(\lambda_\pi^1 + \lambda_0^1\right) \\
\hat{x} = \frac{1}{2}\left(\lambda_0^1 + \lambda_\pi^2\right) & \hat{x} = \frac{1}{2}\left(\lambda_0^2 + \lambda_\pi^2\right) \\
\kappa = \frac{1}{2}\left(\lambda_\pi^1 - \lambda_0^2\right) & \kappa = \frac{1}{2}\left(\lambda_\pi^1 - \lambda_0^1\right) \\
\hat{\kappa} = \frac{1}{2}\left(\lambda_0^1 - \lambda_\pi^2\right) & \hat{\kappa} = \frac{1}{2}\left(\lambda_0^2 - \lambda_\pi^2\right)
\end{array}
\tag{28}
$$

In these solutions a quantity like λ_0^2 is one over the square of the 0-mode frequency of the second branch. In writing these solutions we have taken the first branch to be of lower frequency and associated with the unhatted variables. It is somewhat confusing to see two solutions, but note that in the second solution the value of κ will be positive only for the backward wave cases. The form of Equation 25 requires that the model constants be positive, so in dealing with the forward wave case, Solution 1 must be chosen.

MAFIA simulation of the dispersion curve for shape B19 gives the following results.

$$
\begin{array}{ll}
\nu_0^1 = 3.618490 & x = 0.0610025 \\
\nu_\pi^1 = 3.894703 & \hat{x} = 0.0579295 \\
\nu_0^2 = 4.222761 & \kappa = 0.00492265 \\
\nu_\pi^2 = 5.032554 & \hat{\kappa} = 0.0184453
\end{array}
\tag{29}
$$

With these values for the model constants together with values for the beam pipe correction given in Equation 26, the eigenvalues and eigenvectors of the matrix B.3 can be found. The result is shown in Appendix B.4. The 14 modes are ordered by frequency decreasing left to right, are interpreted as separated into upper and lower bands with modes 14-7 forming the upper band and modes 6-1 in the lower band. Each mode is presented as a column, the frequency eigenvalue listed first, the eigenvector of the unhatted variables below the frequency, and the eigenvalue of the hatted variables below that. The unhatted and hatted variables are referred to as of TM and TE type respectively because in weak-coupled cases, this identification can be made. As is clear from the form of the system matrix, Appendix B.3, the column eigenvectors as calculated are 14 values in length, normalized, with the odd numbered terms giving the values of the unhatted and the even terms the hatted variables. For display the odd and even numbered

values have been separated and separately renormalized. The norm that is given for each type is the divisor required for that renormalization. Thus the original eigenvector can be reconstituted by putting the TM variables times the TM norm in the odd numbered positions and the TE variables times the TE norm in the even positions in a column of 14. For each mode the sum of the squares of the TM and TE norms is unity, and the relative values give an idea of the relative makeup of the mode.

Looking at these TM and TE norms for the first six modes of the solution, one can see that modes 1 and 2 have TE norm greater than 0.9, modes 3 and 4 have TM and TE norms approximately equal, and modes 5 and 6 have a TM norm greater than 0.9. This is consistent with the qualitative impressions drawn from the arrow plots that are discussed above.

In order to quantitatively compare the results of the model with the MAFIA simulation that is illustrated in Appendix B.1, it is necessary to extract eigenvectors from the MAFIA field tables. This can be done in a rather ad hoc manner as shown in Appendix B.2. Variables are defined for each cell by means of integration paths. The path for the TM variable integrates the z-component of the electric field parallel to the axis at the radius of the iris. The path for the TE variable integrates the radial component of the electric field at the center of the cell from the axis to the outer wall. Both of these paths lie at the zero of the azimuth.

The values of the integrals, normalized and reflected according to the symmetry of the boundary at the center of the structure, are shown in Appendix B.2 together with the frequency eigenvalues found by MAFIA. The method that is used here does not give values for the norms, but the normalized eigenvectors can be compared with those found from the model solution listed in Appendix B.4. This is done for the TM variables in Figure 52 for the TE variables in Figure 53. Here the MAFIA-derived values for modes 1-7 are plotted against the values calculated from the two-chain model. Overall signs of the MAFIA eigenvectors are not significant and have been adjusted to match the model solution.

It is clear that the eigenvectors of the model solution are strongly correlated with the MAFIA simulation. The frequencies are accurately predicted by the model. The frequencies of modes 1-6 are compared in Figure 54, and the values are given in Appendix B.2 and B.4.

7.3 Discussion

It is clear that the two-chain model accounts very well for the structure of the modes in the lower TEM band in the strongly coupled case, and it has considerable explanatory and predictive power as well. It is possible to claim that a satisfactory model for the strongly-coupled deflection structure is available. Two questions remaining are: what is there still to do in this area of modeling; and is the strongly coupled be preferred to the weakly coupled structure?

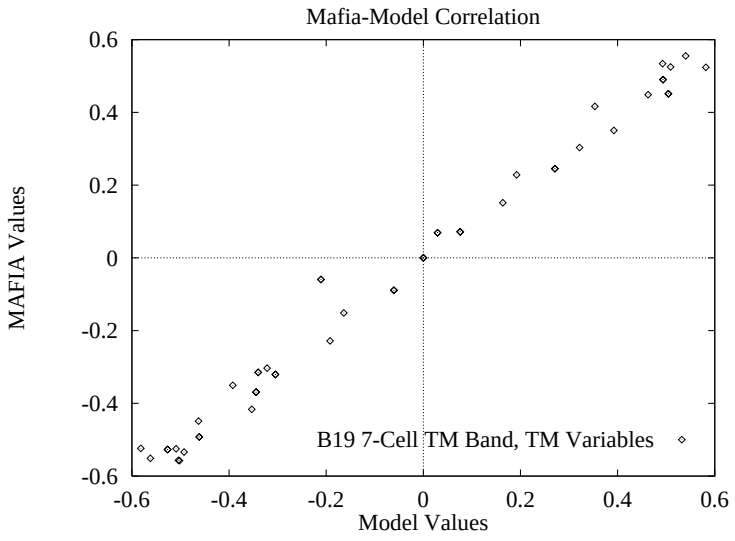

Figure 52: MAFIA-Model Correlation, 7-cell cavity of shape B19, TM-band, TM-variables.

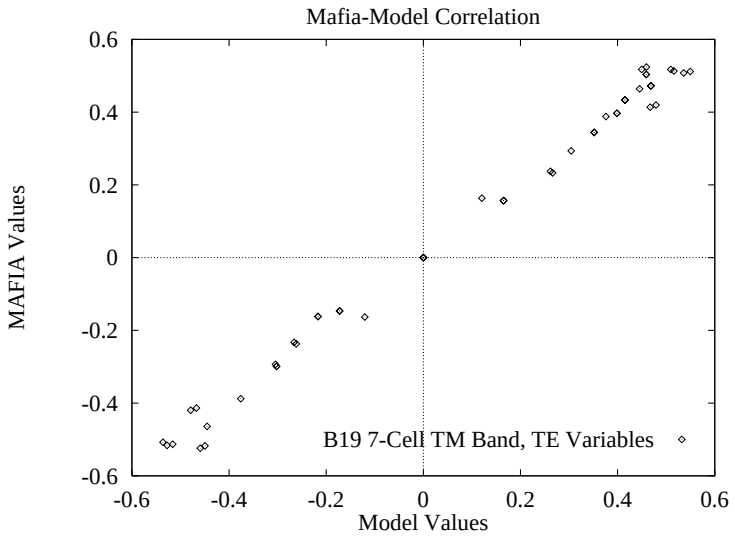

Figure 53: MAFIA-Model Correlation, 7-cell cavity of shape B19, TM-band, TE-variables.

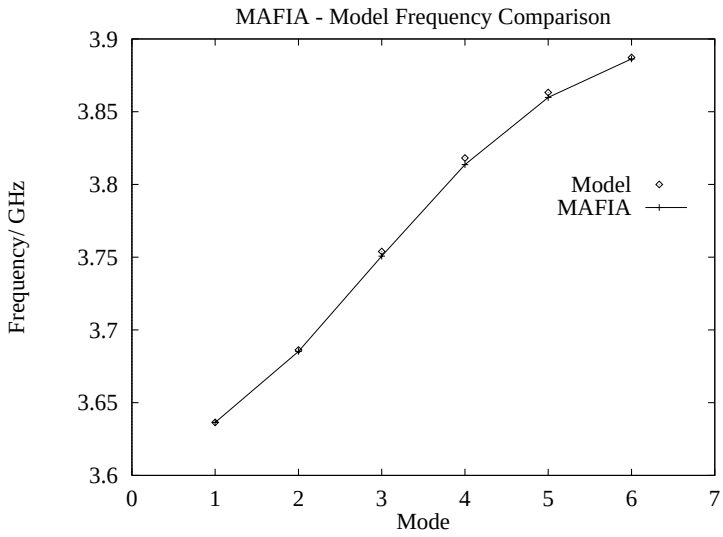

Figure 54: MAFIA-Model Frequency comparison, 7-cell cavity of shape B19, TM-band.

There are some modeling issues left. The first is the structure end-cell tuning for field flatness. This is studied by means of MAFIA simulations in Section 6.2 of this paper with the result that with a large increase in end-cell frequency, it is possible to arrive at nearly flat deflection voltage and magnetic surface field in the body cells. The price of this is that the deflection voltage of the end cell is greatly reduced and the shunt impedance of the structure is lowered. Studies with the model show that something like a flat π-mode can be produced in the strongly-coupled case, but only with significant tuning of the body cells as well as the end cells. This situation appears to be a characteristic of deflection mode structures since it is seen also in weakly-coupled structures. It is likely that the cure for this is worse than the disease, and that a flat π-mode in the sense used in talking about accelerator structures is not a practical possibility.

There is more work to do in this area of structure design. More work also in getting a satisfactory procedure for finding appropriate gamma values for the beam pipe correction, and more work in setting up the model to be used in tuning [14]. Trials with the two-chain model have shown that no problems of a practical mathematical kind stand in the way of structure tuning. It seems likely that the process can be carried out of making bead measurements of some structure quantity, calculating from those measurements a set of cell corrections, and correcting one or more cell. A repetition of this process can adjust this structure quantity to have any profile that is desired. The problem remains of relating the quantity that is adjusted in this process to the quantity that you want to adjust. Suppose that the goal is to tune a structure so that the peak magnetic field on each iris is the same. This is quite likely to be the most useful criterion to use in a superconducting deflector. Now some quantity must be selected to

measure in order to have the information needed to do the tuning. Choose for example to measure the transverse magnetic field along the axis with a metal bead. For the pure TM π-mode this quantity will have a fixed relation to the peak magnetic field that can be determined from MAFIA simulation. However, there will be a small component of TE $5\pi/6$ mode (according to the model - see Appendix B.4, mode 6) which will have a transverse electric field on axis that is different in each cell. The bead will measure the quantity $(E^2-(cB)^2/2)$, and this is what is flattened in the tuning, distorting the flatness of peak magnetic field. Problems of this kind can be overcome, but a lot of simulation work together with structure measurement is required. Developing a workable and accurate tuning method for the strongly-coupled transverse mode structure will require considerable effort.

Now what are the advantages of the strongly-coupled structure and should it be used for this application? The B19 shape has about twice the bandwidth as the C15 shape, and a larger iris diameter. However it has a lower $(r/Q)'$ and a significantly higher normalized peak magnetic field, and we have just argued that it has a longer development time. Issues of multipacting have not been evaluated but may be important. The flatness criterion for the π-mode [12, 15] varies inversely as the bandwidth and directly as the square of the number of cells in the structure. Therefore the greater bandwidth is worth the difference between a 13 cell and 9 cell structure. This is an advantage, but it is a not a make-or-break one. Further, the final choice of the number of cells in the structure can come after the first model structures have been built and does not affect the design of the basic parts or the tooling, whereas the choice of the strongly-coupled structure is much more difficult to retreat from. If it were a very large system that was being planned here the development effort of the new structure type would not bulk so large in the program. Since it is a small system, it is attractive to keep the development cost as small as possible. It is not clear at this time whether the larger aperture is an advantage, but it is clear that the higher $(r/Q)'$ is an advantage from a system and operating point of view, and it is clear that the peak magnetic field is an important consideration. The conclusion is, then, that the technical advantages of the strongly-coupled structure do not outweigh the disadvantages in this application, and it is not worth the additional risk to the project.

7.4 Equivalent-Circuit Modeling of the Backward-Wave Deflection Structure

7.4.1 The Two-Chain Model

The two-chain model can be applied to the backward-wave case with the same procedure that is described for the forward-wave case above. For this study a 13-cell structure of the B15 shape is taken. This structure is not uniform, but

instead has end cells that have been lowered in frequency by increasing the outer cavity radius from 47.2 to 47.627 mm. This change from the body cavity shape is made by changing the circle with radius r_e, see Figure 6 above, to an oblate ellipse leaving point r_2, z_2 fixed. Arrow plots for the modes of this structure are not discernibly different than those for he C15 structure shown in Appendix C.

As before the 4 constants of the model are determined from single-cell calculations, but for this case the four frequencies that are used are the π, $11\pi/12$, and 0 modes of the TM band and the 0 mode of the TE band. That this gives a very good representation of the dispersion curves calculated by MAFIA is shown in Figure 55. It is to be expected that the greatest deviation of the model dispersion curves from the MAFIA simulation will occur at the highest frequencies. The model does not include the frequency dependence of the coupling. In addition, the main region of concern here is the TM band, so it is reasonable to replace the π mode of the TE band with another fit point.

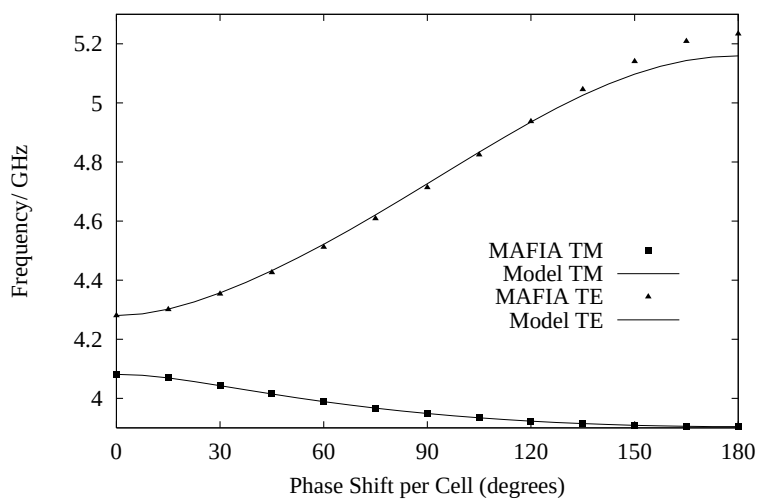

Figure 55: Adjusted Dispersion Curves, 13-Cell B15 Shape.

Using these four points an adjusted value for the TE π-mode frequency is found, and Solution 2 in Equation 28 is used to determine the four model constants. These are:

$$\begin{aligned} x &= 0.0628238 \\ \hat{x} &= 0.0460754 \\ \kappa &= 0.00278398 \\ \hat{\kappa} &= 0.00850956 \\ \gamma &= 0.027778 \\ \hat{\gamma} &= -0.06 \end{aligned} \tag{30}$$

The gamma and the gamma hat in this list were set originally to estimated values, gamma to 0.03 and gamma hat to -0.06 and the model was developed and solved. Recall that this structure has tuned end cells, and this tuning as well as the beam pipe correction enter the model via the gammas. Later the value for gamma was adjusted a small amount to set the frequency of mode 1 to match the MAFIA value. This was done for convenience in comparing the rest of the frequencies in the band. The gamma hat was observed to have almost no effect on the solution and remains where it was originally set. We should say, therefore that the model has five constants. More needs to be done to understand what the values of these corrections should be, particularly for the tuned end cells.

With these constants and a system matrix like that in Appendix B.3 but expanded from 14 to 26 equations, the frequency eigenvalues and the eigenvectors can be found and compared to eigenvectors extracted from the MAFIA field tables by the integrations described in Appendix B.2. Only a part of this material is presented here. Figure 56 shows a correlation plot of the TM eigenvectors in the TM band. The agreement of the model with the MAFIA simulation is very good. The plot for the TE vectors is not included here, but it shows good agreement also. Appendix B.5 compares the model and the MAFIA eigenvectors of mode 1, which is the TM π mode. Also in Appendix B.5 is a list of the MAFIA frequencies and those found from the model. These two are very close. Mode 1 frequency from the model is set to match the MAFIA frequency as mentioned above, and the difference between the two generally increases with mode number. The largest difference in the TM band is less than 5 MHz.

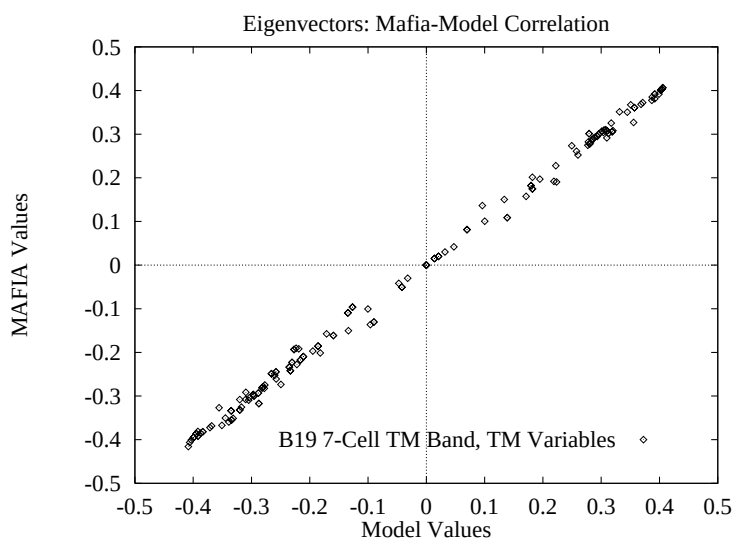

Figure 56: Eigenvectors, MAFIA-Model correlation, 13-cell cavity of shape B15, TM-band.

It is interesting to note that all of the TM norms are greater than 0.95 for modes in the TM band and all of the TE norms are greater than 0.95 for the

modes in the TE band. For mode 1 the TM norm is 0.998 which is the largest in the TM band. Thus mode 1 is very close to a pure TM π-mode. Looking at the TM vector for mode 1, one can see that the largest variable values are in the two cells next to the end cell. This means that the structure is slightly overcompensated, and that the tuning in the end cell should be reduced slightly for the flattest field. The end cell even in this overcompensated state has a reduced value. Increasing the compensation can raise this value, but only at the cost of increasing the values in the two cells inboard from the end cell. This is the same situation, to a lesser degree, that is seen in the strongly coupled structure except that in that case the end cell is compensated by raising the frequency whereas for the weakly coupled structure the end cell frequency is lowered.

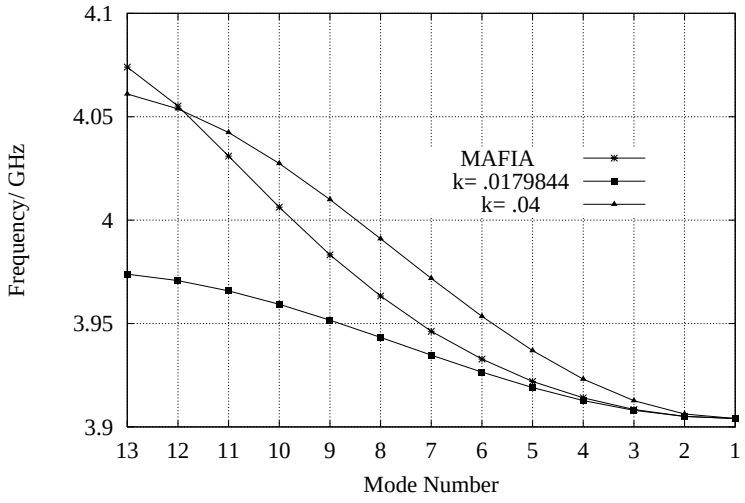

Figure 57: TM Band Frequencies of a MAFIA 13-Cell B15 Structure Compared to a Single-Chain Model with Flat π-Mode

7.4.2 The Single Chain Model

It might be expected that the weakly-coupled deflecting structure can modeled by a single chain of resonators like that used for accelerator structures. The effects of the adjacent TE band might not be too strong. An effort has been made to judge the usefulness of a simple model for tuning. Figure 57 shows the MAFIA TM frequencies plotted against mode number. Also plotted are frequencies from a single chain model. The first of these has the value of the coupling adjusted so that the modes 1 and 2 agree with the MAFIA frequencies. The second case sets k equal to 0.04. It can be seen that the curves for the single chain model are of quite a different shape from the simulated values, and there is no way to choose the best approximation. Further, correlation of the model and MAFIA eigenvectors is much less complete than with the two-chain model but still lie in

only two quadrants of the plot. Clearly the single chain provides a less accurate description of the deflection band than the double-chain, but a description that is qualitatively correct.

Further, if a first order perturbation matrix for mode 1 is calculated from both the single-chain and the double chain models, they are very close to being the same. For this calculation the k = 0.0179844 case is used. This choice correctly models the frequencies of the first few modes in the band, and these are the ones that have the strongest influence on the perturbation matrix. The perturbation matrix calculated from the double-chain model has four times as many terms as that from the single chain. This can be reduced in a straightforward way by taking alternate rows and columns, a procedure which is checked by computing a Jacobian for the TM variables and the TM eigenvalues. The conclusion that is drawn from this is that the single chain model to first order will serve in a tuning procedure just as well as the double chain model. This has recently been demonstrated by tuning a five cell deflector in this way. If, however, it is the intention to solve in higher order or to use measurements on multiple modes to improve the convergence of the tuning process [18], then further work must be done to confirm the usefulness of the single-chain model for these purposes.

One might try to construct a single chain model directly from the TM eigenvalues and eigenvectors derived from MAFIA. Textbooks in matrix analysis show that the eigenvalue problem can be put into the inverse form $A = QDQ^{-1}$ where A is a system matrix, Q is the matrix of its column eigenvectors, and D is the diagonal matrix of the eigenvalues. Note that when A is symmetric, Q inverse is equal to Q transpose. However, a check of the matrix Q of the eigenvectors derived from MAFIA shows that it is not quite unitary, and A is not quite symmetric. A is not displayed here, but there are three interesting things about it that will be mentioned. The diagonal terms are all equal to a part in a thousand except for the first and last. This indicates a uniform structure with tuned end cells. All of the nearest neighbor coupling terms are equal to a few parts in a thousand except again the first and last pair. The members of these pairs are different from the other nearest neighbor coupling terms and different from each other. This suggests that the coupling in the end irises is not the same as in the body irises and that the stored energy in the end cell is not the same as in the body cells. The coupling in the body cells is approximately 0.04, a reasonable value. All of this makes some kind of sense, but the problem here is that there are higher order coupling terms in the matrix all the way out to the corners. These fall in size by only about a factor of three with each increasing order, and all are negative. This is what it takes to make a single-chain model describe a TEM mode band, but it is absolutely unphysical. One does see, however, that a little next-nearest-neighbor coupling is not going to fix up this model. The question to be answered next is whether or not the perturbation matrices calculated from A are correct. This matrix properly describes the band, but it may not properly describe the derivatives that are needed for tuning.

7.4.3 Modeling Problems

The basic tasks of equivalent circuit modeling are to support first the design and then the construction of an RF system. It is clear that there are a good stock of modeling tools available for these tasks in the separator project. There is more work to do to get routine structure tuning under way. And a few things have come up that are different from the parallel activity with an accelerator structure. It is very important to be alert to these differences. One issue that requires thinking about is the proper handling of the situation in which the cell impedance varies down the length of a structure. When is longitudinal variation a perturbation, and when must it be treated in lowest order? Models tend to be derived from infinite, uniform structures by procedures that are not very rigorous, and unfortunately these standing-wave deflection structures are by their nature non-uniform.

A second issue has to do with model reduction. How should a MAFIA simulation be reduced in a fully consistent way to an equivalent circuit? It has been done in this paper in an ad hoc way, but the limits of this way of proceeding are being seen. For example take the problems that arise when we would like to derive the parameters of a two-chain model from MAFIA field tables. Any number of integral paths or bead measurements can be used to extract eigenvectors, but cell impedance is left undefined in this process, and doing it this way doesn't give the relationship between vectors of different modes. It is not clear how to get the equivalent circuit from MAFIA of the norms that were found from the two-chain model solution. The question of how to measure eigenvectors or determine them from field tables keeps coming up. A bead measurement to define a vector is not different from a path integral to define a vector, and there is the same confusion.

Gluckstern has worked out a procedure [15] for expanding cavity fields in terms of normal modes that is ideally suited to operating with MAFIA field tables. The coefficients of this expansion are volume integrals over the cell of products of field vectors. The fields in chains of cells can be expanded in terms of the normal modes of closed cells plus the fields associated with coupling holes, and coupling is defined by surface integrals over the holes. The question of non-uniform chains is not explicitly dealt with, but the normalization scheme used seems to solve this problem. Working out and applying this method for the construction of models for the deflecting cavities will clear away confusions and provide stronger working methods. This is an interesting and worthwhile project.

8 Conclusion

The passband structure of deflecting mode cavities with π-mode cell length, which mainly differ by the cell-to-cell coupling, has been investigated. In the strongly-coupled regime, the deflection band is of the forward-wave type, with the π-mode at the high-frequency end of the band, and in the weakly-coupled regime the deflection band has a backward wave, and the π-mode is the lowest frequency in the band. The deflecting modes are of hybrid (TM and TE) character like any dipole mode in an accelerating structure. But at least in the weakly coupled case the TM-like modes of the deflecting band lie lower in frequency than the TE-like modes, which form the second passband. In the strongly coupled regime TM-*and* TE-like modes can be found in the lowest passband (see B).

The progression from the weakly coupled to the strongly coupled regime is illustrated in Figure 14 above. Cells of shape A13 and A15 are of backward wave type; and cells of shape A19 and A25 are of forward wave type. Cell A17 though of forward wave type is near to the dividing line. The advantages of the strongly-coupled structures is a larger iris diameter and the larger bandwidth; the B19 shape has about twice the bandwidth as the C15 shape. However it has a lower $(r/Q)'$ and a significantly higher normalized peak magnetic field (see Figure 16). For both coupling regimes it is possible to find an end-cell design, which provides a good field flatness within the body cells. For the cavities of shape A15, B19 and C15 solutions have been work out in detail using the computer code MAFIA. In the strongly coupled case the price of the field flatness is that the deflecting voltage of the end cell is greatly reduced and the shunt impedance of the structure is lowered. Therefore the cavities of shape A15 and C15 have a clear advantage with respect to $(r/Q)'$ and peak magnetic field against cavity B19 or similar cavities within the strongly coupled regime. The somewhat modified shape of the iris region (larger curvature) of cavity C15 compared with A15 provides a even lower peak magnetic field for the same deflection gradient and a larger bandwidth.

Equivalent circuit models have been used to compare with Mafia calculations. Both one and two chain models have been investigated. It is shown that the one chain model provides only a qualitatively description of the dispersion curve in both the weak and strong coupling cases. In addition for the strong case the two chain model represents not only the dispersion curve well but also gives eigenvectors in good agreement with those derived from Mafia. Mixtures of TE and TM like modes are clearly indicated.

To minimize the peak fields and to improve the cell-to-cell field flatness during the tuning procedure of a multi-cell cavity a equivalent circuit model is an important tool to process data from a bead pull measurement. Simulations with a model of two chains of coupled resonant circuits with cross coupling have shown that no problems of a practical mathematical kind stand in the way of structure tuning. It seems likely that the process can be carried out of making bead mea-

surements of some structure quantity, calculating from those measurements a set of cell corrections, and correcting one or more cell. Whether the one chain model will be adequate or it will be necessary to use the two chain model still needs to be determined. . The goal is to tune a structure so that the peak magnetic field on each iris is the same for the π-mode. Therefore it is important to distinguish the field of the π-mode and the next lowest mode in the same passband during the bead pulling measurements.

Finally the weakly coupled cavity shape C15 has been selected as the shape to use in the R&D program contingent on favorable multipacting results. Strongly coupled shapes with large irises seem inappropriate because of the complexity of their mode patterns, the lower $(R/Q)'$, and higher peak magnetic field all of which offset any advantages of greater bandwidth. C15 with its larger curvature in the iris is an improvement over the original A15 in that B_{max} is reduced and df/f increased.

A Properties of the Longitudinal and Transverse Voltage of a Cavity

The purpose of this appendix is to derive the formulas used in the section 3, which relate the transverse voltage vector $\boldsymbol{V}_\perp(r,\phi)$ to the longitudinal voltage $V_\parallel(r,\phi)$.

The longitudinal effect of the cavity fields are given by the **longitudinal voltage** - defined as:

$$V_\parallel(r,\phi) = \int_0^L dz\, E_z(r,\phi,z,t=z/c), \tag{31}$$

while the **transverse voltage vector** is the integral of the Lorentz force:

$$\boldsymbol{V}_\perp(r,\phi) = \int_0^L dz\ \left(\boldsymbol{E}_\perp(r,\phi,z,t=z/c) + c\,\boldsymbol{e_z}\ \times\ \boldsymbol{B}(r,\phi,z,t=z/c)\right). \tag{32}$$

The following two subsections demonstrate in detail the relationship between $\boldsymbol{V}_\perp(r,\phi)$ and $V_\parallel(r,\phi)$ based on the Panofsky-Wenzel Theorem [4] and on the fact that $V_\parallel(r,\phi)$ is a harmonic function of the transverse coordinates.

A.1 The relation between $\boldsymbol{V}_\perp$ and $V_\parallel$

From the Maxwell equation $\boldsymbol{\nabla}\times\boldsymbol{E} = -\frac{\partial}{\partial t}\boldsymbol{B}$ it follows:

$$\boldsymbol{e_z}\times\frac{\partial}{\partial t}\boldsymbol{B} = \frac{\partial}{\partial z}\boldsymbol{E}_\perp - \boldsymbol{\nabla}_\perp E_z. \tag{33}$$

The contribution to the transverse voltage due to magnetic field can be written in terms of the electric field:

$$\begin{aligned}\int_0^L dz\, c\,\boldsymbol{e_z}\ \times\ \boldsymbol{B}(r,\phi,z,z/c)\ &= C_0 + \\ &\int_0^L dz\ c\int_{t_0}^{z/c} d\tau\ \left(\frac{\partial}{\partial z}\boldsymbol{E}_\perp(r,\phi,z,\tau) - \boldsymbol{\nabla}_\perp E_z(r,\phi,z,\tau),\right)\end{aligned} \tag{34}$$

with a steady function $C_0(r,\phi)$ due to the time integration ($C_0(r,\phi) = \int_0^L dz\, c\,\boldsymbol{e_z}\times \boldsymbol{B}(r,\phi,z,t_0)$). This expression (Eqn. (34)) can be simplified if one calculates the total derivative of $\int d\tau\,\boldsymbol{E}_\perp$ with respect to z:

$$c\,\frac{d}{dz}\int_{t_0}^{z/c} d\tau\ \boldsymbol{E}_\perp(r,\phi,z,\tau) = \boldsymbol{E}_\perp(r,\phi,z,z/c) + c\int_{t_0}^{z/c} d\tau\,\frac{\partial}{\partial z}\boldsymbol{E}_\perp(r,\phi,z,\tau). \tag{35}$$

Combining Eqn. (34) and (35) yields:

$$\begin{aligned}\int_0^L dz\, c\,\boldsymbol{e_z}\ \times\ \boldsymbol{B}(r,\phi,z,z/c)\ \ =\ \ & -c\,\boldsymbol{\nabla}_\perp\int_0^L dz\int_{t_0}^{z/c} d\tau\, E_z(r,\phi,z,\tau) \\ & +C_0(r,\phi) \\ & -\int_0^L dz\ \boldsymbol{E}_\perp(r,\phi,z,z/c) \\ & c\int_0^L dz\ \left(\frac{d}{dz}\int_{t_0}^{z/c} d\tau\,\boldsymbol{E}_\perp(r,\phi,z,\tau)\right).\end{aligned} \tag{36}$$

The last term gives the contribution from the boundaries, which is zero for a closed cavity due to the boundary conditions for the electric field on a metallic surface. This term can also be neglected if the length L is large enough that the electric field is very small at the boundaries of the integration, which may be located in the beam pipe.

Therefore one obtains for the transverse voltage:

$$\boldsymbol{V}_\perp(r,\phi) = -c\,\boldsymbol{\nabla}_\perp \int_0^L dz \int_{t_0}^{z/c} d\tau\, E_z(r,\phi,z,\tau) + C_0(r,\phi). \tag{37}$$

This result is essentially the Panofsky-Wenzel Theorem, which was originally formulated in terms of the vector potential [4]. The integral of the Lorentz force can be totally expressed as a transverse gradient of an integral of the longitudinal electric field.

The further considerations are now restricted to a **cavity mode** ringing with the revolution frequency ω, i.e. one obtains in complex notation for the electric field:

$$E_z(r,\phi,z,t) = \widetilde{E_z}(r,\phi,z)\,\exp(-i\,\omega\,t).$$

In this case it is possible to solve the integral on the time variable τ in Eq. (37). The contribution from the lower boundary at t_0 is exactly canceled by $C_0(r,\phi)$, and the following expression is obtained:

$$\boldsymbol{V}_\perp(r,\phi) = \frac{-i}{\omega/c}\,\boldsymbol{\nabla}_\perp \int_0^L dz\,\widetilde{E_z}(r,\phi,z)\,\exp(-i\,\omega\,z/c), \tag{38}$$

which can also be rewritten in terms of the longitudinal voltage.

The final result for any cavity mode is therefore:

$$\begin{aligned} \boldsymbol{V}_\perp(r,\phi) &= \frac{-i}{\omega/c}\,\boldsymbol{\nabla}_\perp V_\parallel(r,\phi) \\ V_\parallel(r,\phi) &= \int_0^L dz\,\widetilde{E_z}(r,\phi,z)\,\exp(-i\,\omega\,z/c). \end{aligned} \tag{39}$$

The next short subsection established an important property of the longitudinal voltage, which will finally show that the transverse voltage does not depend on the radius r for any *dipole* mode.

A.2 Properties of $V_\parallel(r,\phi)$ and the Dependence of $\boldsymbol{V}_\perp$ on the radius.

In the pipe region of the cavity (radius smaller than the cavity iris radius) it is possible to expand the electric field in terms of waves (Fourier transformation in t and z) :

$$E_z(r,\phi,z,t) = \frac{1}{(2\pi)^2}\int_{-\infty}^{\infty} d\omega \int_{-\infty}^{\infty} dk_z\;\widetilde{E_z}(r,\phi,k_z,\omega)\;\exp(-i(\omega\,t - k_z\,z)). \tag{40}$$

For a cavity mode the electric field is a solution of the wave equation. The Fourier component $\widetilde{E_z}(r,\phi,k_z,\omega)$ fulfills therefore the equation:

$$\nabla_\perp^2 \widetilde{E_z}(r,\phi,k_z,\omega) = \left(k_z^2 - (\frac{\omega}{c})^2\right) \widetilde{E_z}(r,\phi,k_z,\omega). \tag{41}$$

This can be used to show that the longitudinal voltage is a harmonic function of the transverse coordinates (r,ϕ):

$$\begin{aligned}
& \nabla_\perp^2 \; V_{||}(r,\phi) \\
= \; & \frac{1}{(2\pi)^2} \int_0^L dz \int_{-\infty}^{\infty} d\omega \int_{-\infty}^{\infty} dk_z \; \nabla_\perp^2 \widetilde{E_z}(r,\phi,k_z,\omega) \; \mathrm{e}^{-i(\omega \; z/c - k_z \; z)} \\
= \; & \frac{1}{(2\pi)^2} \int_{-\infty}^{\infty} d\omega \int_{-\infty}^{\infty} dk_z \, \widetilde{E_z}(r,\phi,k_z,\omega) \int_0^L dz \left(k_z^2 - (\frac{\omega}{c})^2\right) \; \mathrm{e}^{-i(\omega \; z/c - k_z \; z)} \\
= \; & 0,
\end{aligned} \tag{42}$$

since the integration with respect to z yields a δ - function and $\widetilde{E_z}(r,\phi,k_z,\omega)$ has no poles with respect to the variables k_z and ω. The property

$$\nabla_\perp^2 V_{||}(r,\phi) = \left(\frac{1}{r}\frac{\partial}{\partial r}(r \; \frac{\partial}{\partial r}) + \frac{1}{r^2}\frac{\partial^2}{\partial \phi^2})\right) \; V_{||}(r,\phi) = 0 \tag{43}$$

of the longitudinal voltage enables one to determine how $V_{||}(r,\phi)$ varies with respect to r for a given azimuthal dependence of the the cavity mode.

Suppose the electric field is periodic in ϕ, i.e.

$$E_z \sim \cos(m\,\phi)$$

then a solution of the Eqn.(43), which is regular at $r = 0$, is

$$V_{||}(r,\phi)^{(m)} = V_m \; r^m \; \cos(m\,\phi), \tag{44}$$

with a constant V_m. The transverse voltage is according to the results of the previous section (see Eqn. (39)):

$$\boldsymbol{V}_\perp(r,\phi) = \frac{-i}{\omega/c} \left(\frac{\partial}{\partial r} V_{||}(r,\phi) \; \boldsymbol{e_r} + \frac{1}{r}\frac{\partial}{\partial \phi} V_{||}(r,\phi) \; \boldsymbol{e_\phi}\right), \tag{45}$$

with the unit vectors $\boldsymbol{e_r}$ and $\boldsymbol{e_\phi}$ in the radial and azimuthal direction.

Finally one obtains for the radial component of the transverse voltage for a **m-pole mode**:

$$V_{\perp r}^{(m)}(r,\phi) = \frac{-i}{\omega/c} \frac{m}{r} V_{||}(r,\phi)^{(m)}. \tag{46}$$

For a dipole mode (m=1) $V_{\perp r}^{(m)}(r,\phi)$ is independent of the radius r. The kick on the beam due to a dipole mode in the cavity does not depend on the radial position of the trajectory.

B A 7-cell cavity of shape B19 with an uncompensated end-cell

B.1 Modes from a MAFIA calculation

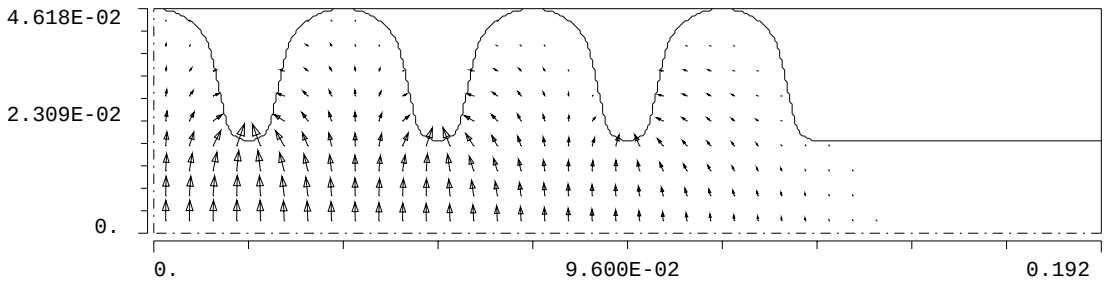

Figure 58: 7-cell cavity of shape B19, electric field of dipole mode *ME*-1.

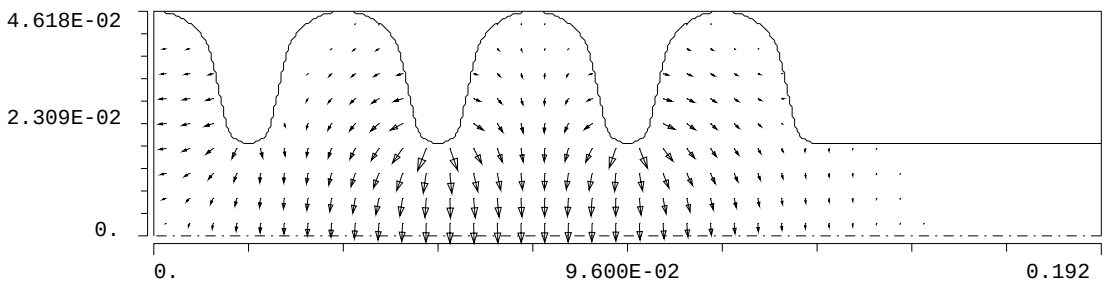

Figure 59: 7-cell cavity of shape B19, electric field of dipole mode *EE*-1.

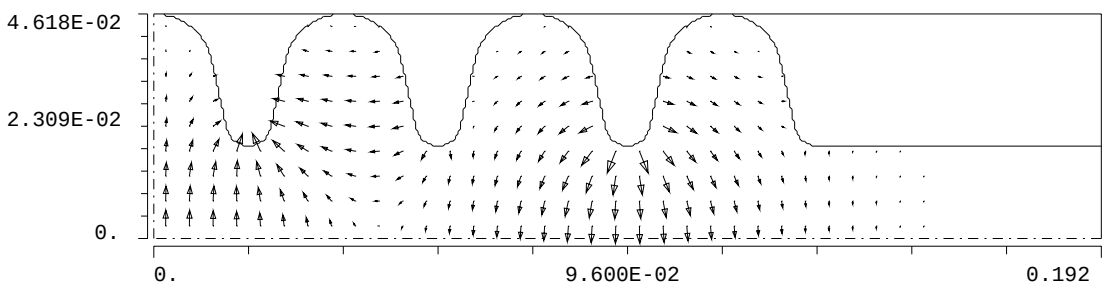

Figure 60: 7-cell cavity of shape B19, electric field of dipole mode *ME*-2.

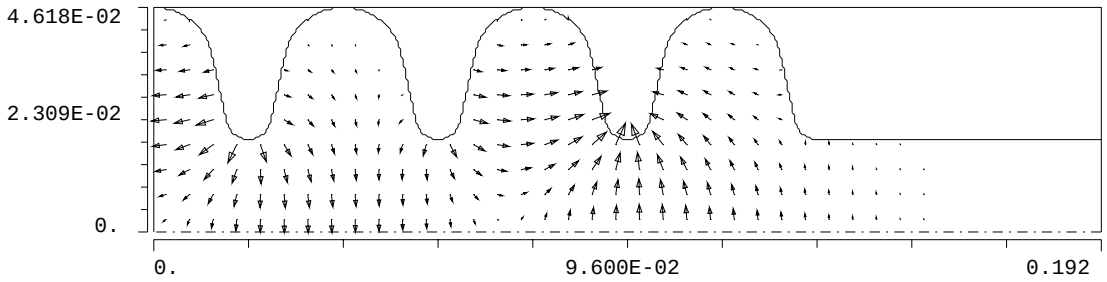

Figure 61: 7-cell cavity of shape B19, electric field of dipole mode *EE*-2.

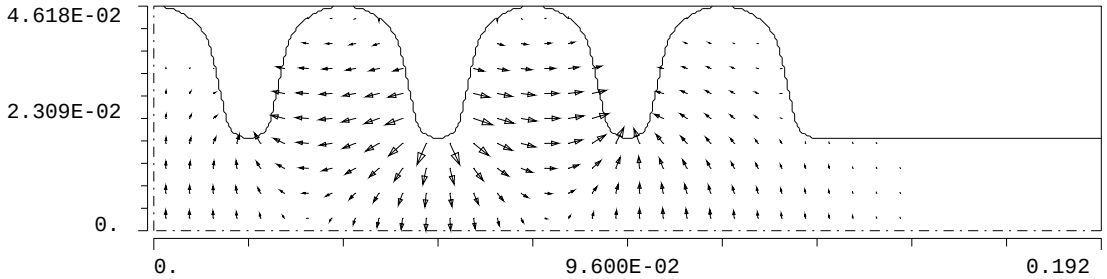

Figure 62: 7-cell cavity of shape B19, electric field of dipole mode *ME*-3.

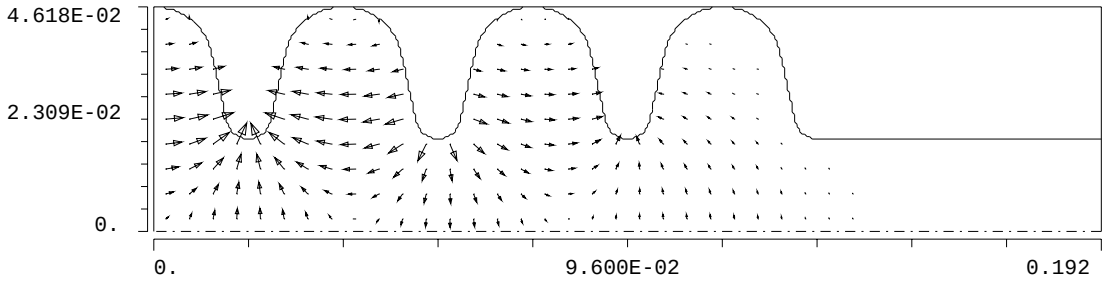

Figure 63: 7-cell cavity of shape B19, electric field of dipole mode *EE*-3.

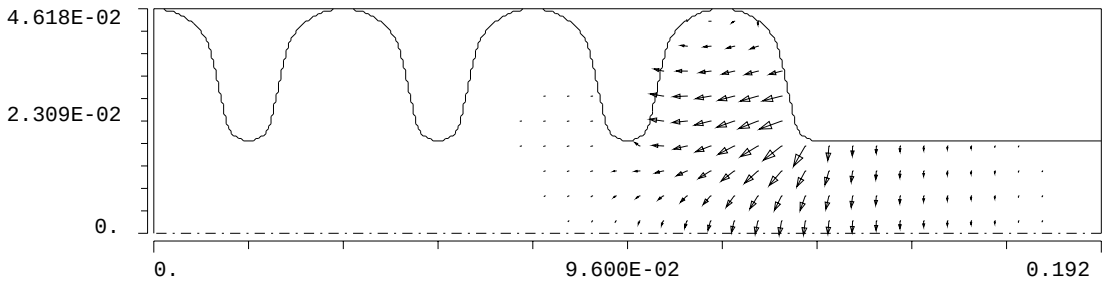

Figure 64: 7-cell cavity of shape B19, electric field of dipole mode *EE*-4 or *ME*-4. This is a trapped mode.

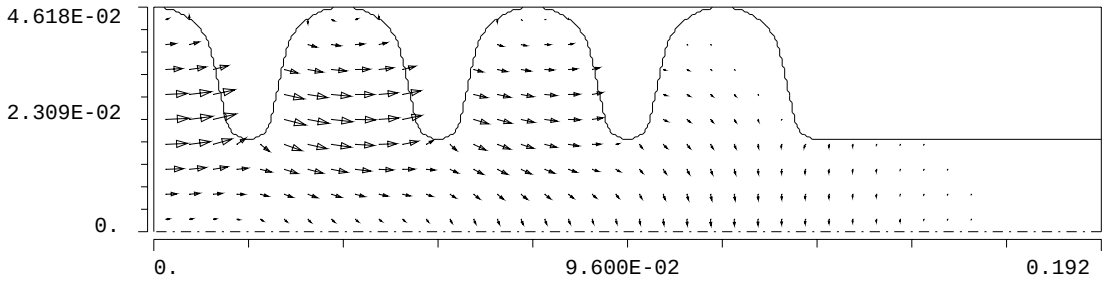

Figure 65: 7-cell cavity of shape B19, electric field of dipole mode *EE*-5. This is the first mode of the second passband.

B.2 Eigenvalues and Eigenvectors from a MAFIA Calculation

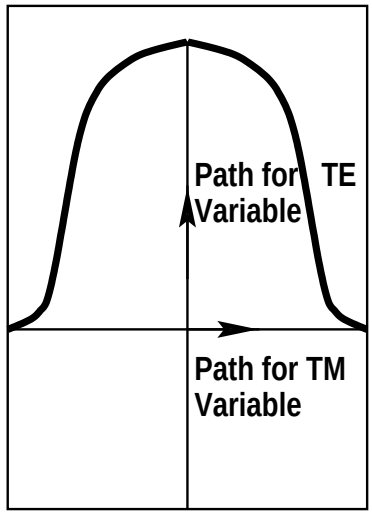

Figure 66: Integration Paths for the TM and TE Variables

Mode 7	Mode 6	Mode 5	Mode 4	Mode 3	Mode 2	Mode 1
Frequency						
4.2406	3.8873	3.8632	3.8182	3.7539	3.6862	3.6365
TM Variables						
-0.0595	0.0760	0.1636	0.2709	0.3923	0.5045	0.5817
-0.3148	-0.3046	-0.5091	-0.5264	-0.3216	0.0294	0.3531
-0.4924	0.4935	0.4627	-0.0607	-0.4926	-0.3444	0.1921
-0.5566	-0.5620	0.0000	0.5400	0.0000	-0.5020	0.0000
-0.4924	0.4935	-0.4627	-0.0607	0.4926	-0.3444	-0.1921
-0.3148	-0.3046	0.5091	-0.5264	0.3216	0.0294	-0.3531
-0.0595	0.0760	-0.1636	0.2709	-0.3923	0.5045	-0.5817
TE Variables						
-0.5173	0.4594	0.4589	0.4452	0.3986	0.3043	0.1651
-0.4196	-0.4671	-0.2169	0.1204	0.4151	0.5158	0.3517
-0.2373	0.2660	-0.3023	-0.5360	-0.1722	0.3759	0.4683
0.0000	0.0000	0.5495	0.0000	-0.5275	0.0000	0.5094
0.2373	-0.2660	-0.3023	0.5360	-0.1722	-0.3759	0.4683
0.4196	0.4671	-0.2169	-0.1204	0.4151	-0.5158	0.3517
0.5173	-0.4594	0.4589	-0.4452	0.3986	-0.3043	0.1651

B.3 System Matrix

$$
\begin{bmatrix}
x(1+\gamma)-\frac{\kappa}{2} & \frac{\sqrt{\kappa\hat{\kappa}}}{2} & \frac{\kappa}{2} & -\frac{\sqrt{\kappa\hat{\kappa}}}{2} & \frac{\sqrt{\kappa\hat{\kappa}}}{2} & -\frac{\kappa}{2} & -\frac{\sqrt{\kappa\hat{\kappa}}}{2} & \frac{\sqrt{\kappa\hat{\kappa}}}{2} & \frac{\kappa}{2} & -\frac{\sqrt{\kappa\hat{\kappa}}}{2} & \frac{\sqrt{\kappa\hat{\kappa}}}{2} & -\frac{\kappa}{2} & -\frac{\sqrt{\kappa\hat{\kappa}}}{2} & \frac{\sqrt{\kappa\hat{\kappa}}}{2} & \frac{\kappa}{2} & -\frac{\sqrt{\kappa\hat{\kappa}}}{2} \\
\frac{\sqrt{\kappa\hat{\kappa}}}{2} & \hat{x}(1+\hat{\gamma})-\frac{\hat{\kappa}}{2} & -\frac{\sqrt{\kappa\hat{\kappa}}}{2} & \frac{\hat{\kappa}}{2} & -\frac{\sqrt{\kappa\hat{\kappa}}}{2} & \frac{\hat{\kappa}}{2} & \frac{\sqrt{\kappa\hat{\kappa}}}{2} & -\frac{\hat{\kappa}}{2} & -\frac{\sqrt{\kappa\hat{\kappa}}}{2} & \frac{\hat{\kappa}}{2} & -\frac{\sqrt{\kappa\hat{\kappa}}}{2} & \frac{\hat{\kappa}}{2} & \frac{\sqrt{\kappa\hat{\kappa}}}{2} & -\frac{\hat{\kappa}}{2} & -\frac{\sqrt{\kappa\hat{\kappa}}}{2} & \frac{\hat{\kappa}}{2} \\
\frac{\kappa}{2} & -\frac{\sqrt{\kappa\hat{\kappa}}}{2} & x & \frac{\kappa}{2} & -\frac{\sqrt{\kappa\hat{\kappa}}}{2} & \frac{\kappa}{2} & -\frac{\sqrt{\kappa\hat{\kappa}}}{2} & \frac{\kappa}{2} & x & -\frac{\sqrt{\kappa\hat{\kappa}}}{2} & \frac{\kappa}{2} & -\frac{\sqrt{\kappa\hat{\kappa}}}{2} & \frac{\kappa}{2} & -\frac{\sqrt{\kappa\hat{\kappa}}}{2} & x(1+\gamma)-\frac{\kappa}{2} & -\frac{\sqrt{\kappa\hat{\kappa}}}{2} \\
-\frac{\sqrt{\kappa\hat{\kappa}}}{2} & \frac{\hat{\kappa}}{2} & -\frac{\sqrt{\kappa\hat{\kappa}}}{2} & \hat{x} & -\frac{\sqrt{\kappa\hat{\kappa}}}{2} & \frac{\hat{\kappa}}{2} & \frac{\sqrt{\kappa\hat{\kappa}}}{2} & -\frac{\hat{\kappa}}{2} & -\frac{\sqrt{\kappa\hat{\kappa}}}{2} & \frac{\hat{\kappa}}{2} & -\frac{\sqrt{\kappa\hat{\kappa}}}{2} & \frac{\hat{\kappa}}{2} & \frac{\sqrt{\kappa\hat{\kappa}}}{2} & -\frac{\hat{\kappa}}{2} & -\frac{\sqrt{\kappa\hat{\kappa}}}{2} & \frac{\hat{\kappa}}{2} \\
\frac{\kappa}{2} & -\frac{\sqrt{\kappa\hat{\kappa}}}{2} & \frac{\kappa}{2} & -\frac{\sqrt{\kappa\hat{\kappa}}}{2} & x & -\frac{\kappa}{2} & -\frac{\sqrt{\kappa\hat{\kappa}}}{2} & \frac{\kappa}{2} & -\frac{\sqrt{\kappa\hat{\kappa}}}{2} & \frac{\kappa}{2} & -\frac{\sqrt{\kappa\hat{\kappa}}}{2} & \frac{\kappa}{2} & -\frac{\sqrt{\kappa\hat{\kappa}}}{2} & \frac{\kappa}{2} & -\frac{\sqrt{\kappa\hat{\kappa}}}{2} & x(1+\gamma)-\frac{\kappa}{2} \\
-\frac{\sqrt{\kappa\hat{\kappa}}}{2} & \frac{\hat{\kappa}}{2} & -\frac{\sqrt{\kappa\hat{\kappa}}}{2} & \frac{\hat{\kappa}}{2} & -\frac{\sqrt{\kappa\hat{\kappa}}}{2} & \hat{x} & -\frac{\sqrt{\kappa\hat{\kappa}}}{2} & \frac{\hat{\kappa}}{2} & -\frac{\sqrt{\kappa\hat{\kappa}}}{2} & \frac{\hat{\kappa}}{2} & -\frac{\sqrt{\kappa\hat{\kappa}}}{2} & \frac{\hat{\kappa}}{2} & \frac{\sqrt{\kappa\hat{\kappa}}}{2} & -\frac{\hat{\kappa}}{2} & -\frac{\sqrt{\kappa\hat{\kappa}}}{2} & \frac{\hat{\kappa}}{2} \\
\frac{\kappa}{2} & -\frac{\sqrt{\kappa\hat{\kappa}}}{2} & \frac{\kappa}{2} & -\frac{\sqrt{\kappa\hat{\kappa}}}{2} & \frac{\kappa}{2} & -\frac{\sqrt{\kappa\hat{\kappa}}}{2} & x & -\frac{\kappa}{2} & -\frac{\sqrt{\kappa\hat{\kappa}}}{2} & \frac{\kappa}{2} & -\frac{\sqrt{\kappa\hat{\kappa}}}{2} & \frac{\kappa}{2} & -\frac{\sqrt{\kappa\hat{\kappa}}}{2} & \frac{\kappa}{2} & -\frac{\sqrt{\kappa\hat{\kappa}}}{2} & x(1+\gamma)-\frac{\kappa}{2} \\
-\frac{\sqrt{\kappa\hat{\kappa}}}{2} & \frac{\hat{\kappa}}{2} & -\frac{\sqrt{\kappa\hat{\kappa}}}{2} & \frac{\hat{\kappa}}{2} & -\frac{\sqrt{\kappa\hat{\kappa}}}{2} & \frac{\hat{\kappa}}{2} & -\frac{\sqrt{\kappa\hat{\kappa}}}{2} & \hat{x} & -\frac{\sqrt{\kappa\hat{\kappa}}}{2} & \frac{\hat{\kappa}}{2} & -\frac{\sqrt{\kappa\hat{\kappa}}}{2} & \frac{\hat{\kappa}}{2} & \frac{\sqrt{\kappa\hat{\kappa}}}{2} & -\frac{\hat{\kappa}}{2} & -\frac{\sqrt{\kappa\hat{\kappa}}}{2} & \frac{\hat{\kappa}}{2} \\
\frac{\kappa}{2} & -\frac{\sqrt{\kappa\hat{\kappa}}}{2} & \frac{\kappa}{2} & -\frac{\sqrt{\kappa\hat{\kappa}}}{2} & \frac{\kappa}{2} & -\frac{\sqrt{\kappa\hat{\kappa}}}{2} & \frac{\kappa}{2} & -\frac{\sqrt{\kappa\hat{\kappa}}}{2} & x & -\frac{\kappa}{2} & -\frac{\sqrt{\kappa\hat{\kappa}}}{2} & \frac{\kappa}{2} & -\frac{\sqrt{\kappa\hat{\kappa}}}{2} & \frac{\kappa}{2} & -\frac{\sqrt{\kappa\hat{\kappa}}}{2} & x(1+\gamma)-\frac{\kappa}{2} \\
-\frac{\sqrt{\kappa\hat{\kappa}}}{2} & \frac{\hat{\kappa}}{2} & -\frac{\sqrt{\kappa\hat{\kappa}}}{2} & \frac{\hat{\kappa}}{2} & -\frac{\sqrt{\kappa\hat{\kappa}}}{2} & \frac{\hat{\kappa}}{2} & -\frac{\sqrt{\kappa\hat{\kappa}}}{2} & \frac{\hat{\kappa}}{2} & -\frac{\sqrt{\kappa\hat{\kappa}}}{2} & \hat{x} & -\frac{\sqrt{\kappa\hat{\kappa}}}{2} & \frac{\hat{\kappa}}{2} & \frac{\sqrt{\kappa\hat{\kappa}}}{2} & -\frac{\hat{\kappa}}{2} & -\frac{\sqrt{\kappa\hat{\kappa}}}{2} & \frac{\hat{\kappa}}{2} \\
\frac{\kappa}{2} & -\frac{\sqrt{\kappa\hat{\kappa}}}{2} & \frac{\kappa}{2} & -\frac{\sqrt{\kappa\hat{\kappa}}}{2} & \frac{\kappa}{2} & -\frac{\sqrt{\kappa\hat{\kappa}}}{2} & \frac{\kappa}{2} & -\frac{\sqrt{\kappa\hat{\kappa}}}{2} & \frac{\kappa}{2} & -\frac{\sqrt{\kappa\hat{\kappa}}}{2} & x & -\frac{\kappa}{2} & -\frac{\sqrt{\kappa\hat{\kappa}}}{2} & \frac{\kappa}{2} & -\frac{\sqrt{\kappa\hat{\kappa}}}{2} & x(1+\gamma)-\frac{\kappa}{2} \\
-\frac{\sqrt{\kappa\hat{\kappa}}}{2} & \frac{\hat{\kappa}}{2} & -\frac{\sqrt{\kappa\hat{\kappa}}}{2} & \frac{\hat{\kappa}}{2} & -\frac{\sqrt{\kappa\hat{\kappa}}}{2} & \frac{\hat{\kappa}}{2} & -\frac{\sqrt{\kappa\hat{\kappa}}}{2} & \frac{\hat{\kappa}}{2} & -\frac{\sqrt{\kappa\hat{\kappa}}}{2} & \frac{\hat{\kappa}}{2} & -\frac{\sqrt{\kappa\hat{\kappa}}}{2} & \hat{x} & \frac{\sqrt{\kappa\hat{\kappa}}}{2} & -\frac{\hat{\kappa}}{2} & -\frac{\sqrt{\kappa\hat{\kappa}}}{2} & \frac{\hat{\kappa}}{2} \\
\frac{\kappa}{2} & -\frac{\sqrt{\kappa\hat{\kappa}}}{2} & \frac{\kappa}{2} & -\frac{\sqrt{\kappa\hat{\kappa}}}{2} & \frac{\kappa}{2} & -\frac{\sqrt{\kappa\hat{\kappa}}}{2} & \frac{\kappa}{2} & -\frac{\sqrt{\kappa\hat{\kappa}}}{2} & \frac{\kappa}{2} & -\frac{\sqrt{\kappa\hat{\kappa}}}{2} & \frac{\kappa}{2} & -\frac{\sqrt{\kappa\hat{\kappa}}}{2} & x & -\frac{\kappa}{2} & -\frac{\sqrt{\kappa\hat{\kappa}}}{2} & x(1+\gamma)-\frac{\kappa}{2} \\
-\frac{\sqrt{\kappa\hat{\kappa}}}{2} & \frac{\hat{\kappa}}{2} & -\frac{\sqrt{\kappa\hat{\kappa}}}{2} & \frac{\hat{\kappa}}{2} & -\frac{\sqrt{\kappa\hat{\kappa}}}{2} & \frac{\hat{\kappa}}{2} & -\frac{\sqrt{\kappa\hat{\kappa}}}{2} & \frac{\hat{\kappa}}{2} & -\frac{\sqrt{\kappa\hat{\kappa}}}{2} & \frac{\hat{\kappa}}{2} & -\frac{\sqrt{\kappa\hat{\kappa}}}{2} & \frac{\hat{\kappa}}{2} & -\frac{\sqrt{\kappa\hat{\kappa}}}{2} & \hat{x} & \frac{\sqrt{\kappa\hat{\kappa}}}{2} & -\frac{\hat{\kappa}}{2} \\
\frac{\kappa}{2} & -\frac{\sqrt{\kappa\hat{\kappa}}}{2} & \frac{\kappa}{2} & -\frac{\sqrt{\kappa\hat{\kappa}}}{2} & \frac{\kappa}{2} & -\frac{\sqrt{\kappa\hat{\kappa}}}{2} & \frac{\kappa}{2} & -\frac{\sqrt{\kappa\hat{\kappa}}}{2} & \frac{\kappa}{2} & -\frac{\sqrt{\kappa\hat{\kappa}}}{2} & \frac{\kappa}{2} & -\frac{\sqrt{\kappa\hat{\kappa}}}{2} & \frac{\kappa}{2} & -\frac{\sqrt{\kappa\hat{\kappa}}}{2} & x & -\frac{\kappa}{2} \\
-\frac{\sqrt{\kappa\hat{\kappa}}}{2} & \frac{\hat{\kappa}}{2} & -\frac{\sqrt{\kappa\hat{\kappa}}}{2} & \frac{\hat{\kappa}}{2} & -\frac{\sqrt{\kappa\hat{\kappa}}}{2} & \frac{\hat{\kappa}}{2} & -\frac{\sqrt{\kappa\hat{\kappa}}}{2} & \frac{\hat{\kappa}}{2} & -\frac{\sqrt{\kappa\hat{\kappa}}}{2} & \frac{\hat{\kappa}}{2} & -\frac{\sqrt{\kappa\hat{\kappa}}}{2} & \frac{\hat{\kappa}}{2} & -\frac{\sqrt{\kappa\hat{\kappa}}}{2} & \frac{\hat{\kappa}}{2} & -\frac{\sqrt{\kappa\hat{\kappa}}}{2} & \hat{x}(1+\hat{\gamma})-\frac{\hat{\kappa}}{2}
\end{bmatrix}
$$

Figure 67: System matrix.

B.4 Table of Eigenvalues and Eigenvectors from Double-Chain Model

B.4.1 Upper Band

Mode 14	Mode 13	Mode 12	Mode 11	Mode 10	Mode 9	Mode 8	Mode 7
Frequency/ GHz							
4.9749	4.8266	4.6451	4.4903	4.3935	4.3316	4.2762	4.2362
TM norm							
0.1010	0.2220	0.3818	0.5905	0.8022	0.9221	0.9621	0.9880
TM Variables							
0.367	-0.188	0.076	-0.380	0.587	0.603	0.442	-0.211
-0.531	0.023	-0.418	0.486	-0.175	0.207	0.449	-0.340
0.288	0.478	0.565	0.012	-0.354	-0.167	0.321	-0.461
0.000	-0.687	0.000	-0.487	0.000	-0.362	0.000	-0.504
-0.288	0.478	-0.565	0.012	0.354	-0.167	-0.321	-0.461
0.531	0.023	0.418	0.486	0.175	0.207	-0.449	-0.340
-0.367	-0.188	-0.076	-0.380	-0.587	0.603	-0.442	-0.211
TE norm							
0.9949	0.9750	0.9242	0.8070	0.5970	0.3869	0.2728	0.1547
TE Variables							
0.195	-0.367	-0.495	0.560	-0.511	-0.229	0.242	-0.450
-0.348	0.491	0.340	0.022	-0.372	-0.454	0.014	-0.479
0.463	-0.353	0.173	-0.431	0.105	-0.492	-0.467	-0.262
-0.503	0.000	-0.468	0.000	0.424	0.000	-0.668	0.000
0.463	0.353	0.173	0.431	0.105	0.492	-0.467	0.262
-0.348	-0.491	0.340	-0.022	-0.372	0.454	0.014	0.479
0.195	0.367	-0.495	-0.560	-0.511	0.229	0.242	0.450

B.4.2 Lower Band

Mode 6	Mode 5	Mode 4	Mode 3	Mode 2	Mode 1
Frequency/ GHz					
3.8873	3.8632	3.8182	3.7539	3.6862	3.6365
TM norm					
0.9827	0.9228	0.8022	0.6190	0.4080	0.2002
TM Variables					
0.076	0.164	0.271	0.392	0.505	0.582
-0.305	-0.509	-0.526	-0.322	0.029	0.353
0.493	0.463	-0.061	-0.493	-0.344	0.192
-0.562	0.000	0.540	0.000	-0.502	0.000
0.493	-0.463	-0.061	0.493	-0.344	-0.192
-0.305	0.509	-0.526	0.322	0.029	-0.353
0.076	-0.164	0.271	-0.392	0.505	-0.582
TE norm					
0.1854	0.3852	0.5970	0.7854	0.9130	0.9797
TE Variables					
0.459	0.459	0.445	0.399	0.304	0.165
-0.467	-0.217	0.120	0.415	0.516	0.352
0.266	-0.302	-0.536	-0.172	0.376	0.468
0.000	0.549	0.000	-0.528	0.000	0.509
-0.266	-0.302	0.536	-0.172	-0.376	0.468
0.467	-0.217	-0.120	0.415	-0.516	0.352
-0.459	0.459	-0.445	0.399	-0.304	0.165

B.5 Some Results from the Modeling and MAFIA Studies of a 13-Cell Structure of B15 Shape with a Tuned End Cell

	Frequencies			Eigenvector of Mode 1	
	Model	MAFIA		Model	MAFIA
Mode	TE Band		TM norm	0.9978	
26	5.24409	5.21510		-0.2170	-0.2229
25	5.24371	5.16365		0.2952	0.2950
24	5.13532	5.08871		-0.2902	-0.2932
23	5.07492	4.99978		0.2864	0.2872
22	4.99223	4.90444		-0.2836	-0.2813
21	4.89604	4.80710		0.2820	0.2775
20	4.79324	4.71166		-0.2814	-0.2782
19	4.68957	4.61988		0.2820	0.2775
18	4.58967	4.53434		-0.2836	-0.2813
17	4.49717	4.45638		0.2864	0.2872
16	4.41515	4.38822		-0.2902	-0.2932
15	4.34705	4.33252		0.2952	0.2950
14	4.29868	4.29423		-0.2170	-0.2229
	TM Band		TE norm	0.0665	
13	4.07615	4.07400		-0.7068	-0.7065
12	4.05985	4.05519		-0.0145	-0.0011
11	4.03545	4.03099		0.0115	0.0133
10	4.00943	4.00625		-0.0086	-0.0193
9	3.98540	3.98317		0.0057	0.0158
8	3.96461	3.96328		-0.0029	-0.0035
7	3.94729	3.94624		0.0000	0.0000
6	3.93329	3.93278		0.0029	0.0035
5	3.92232	3.92197		-0.0057	-0.0158
4	3.91411	3.91405		0.0086	0.0193
3	3.90843	3.90842		-0.0115	-0.0133
2	3.90509	3.90505		0.0145	0.0011
1	3.90405	3.90405		0.7068	0.7065

C Modes of a 13-cell cavity of shape C15 with a tuned end-cell

C15		mid-cell	end-cell
half cell length	$g/2$	19.2 mm	19.2 mm
iris radius	a	15.0 mm	15.0 mm
iris curvature	r_i	5.5 mm	5.5 mm
equator radius	b	47.18 mm	47.55 mm
equator curvature	r_e	11.41 mm	11.41 mm
Mid-points	z_1	5.447 mm	5.449 mm
	r_1	19.74 mm	19.76 mm
	z_2	7.899 mm	7.895 mm
	r_2	37.34 mm	37.68 mm

Table 9: Geometrical parameters of the cavity input shapes. The input shapes are approximated on a mesh, with about 7300 points per cell.

mode #	f / MHz	$(R/Q)'$ / Ohm	G_1 / Ohm
1	3899.8	351	228
2	3900.9	0.001	229
3	3904.4	0.709	230
4	3910.1	0.033	232
5	3918.4	0.394	234
6	3929.3	0.071	236
7	3942.9	0.296	239
8	3959.4	0.132	244
9	3978.5	0.183	250
10	3999.6	0.188	257
11	4021.5	0.062	266
12	4041.7	0.126	275
13	4056.4	0.004	284

Table 10: Results from the MAFIA eigenvalue solver and post-processor for 13-cell cavity of shape C15 with a tuned end-cell.

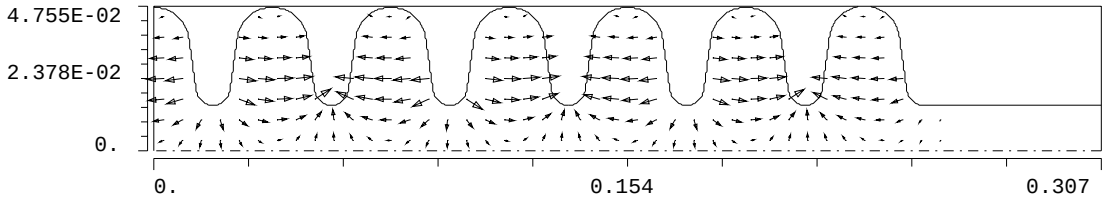

Figure 68: 13-cell cavity of shape C15, electric field of the mode $f = 3.8998$ GHz (b.cond. *EE*); phase advance $\varphi = 177°$ (π-mode).

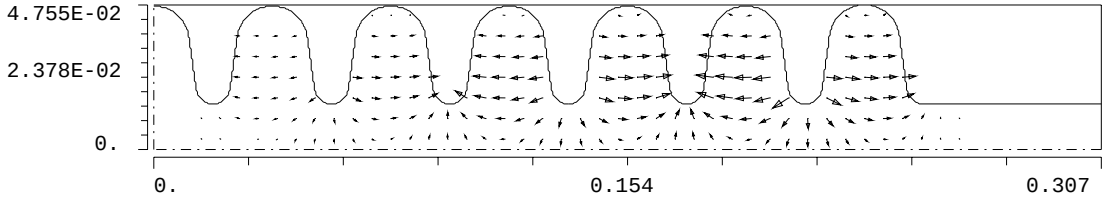

Figure 69: 13-cell cavity of shape C15, electric field of the mode $f = 3.9009$ GHz (b.cond. *ME*); phase advance $\varphi = 165°$ ($11\,\pi/12$- mode).

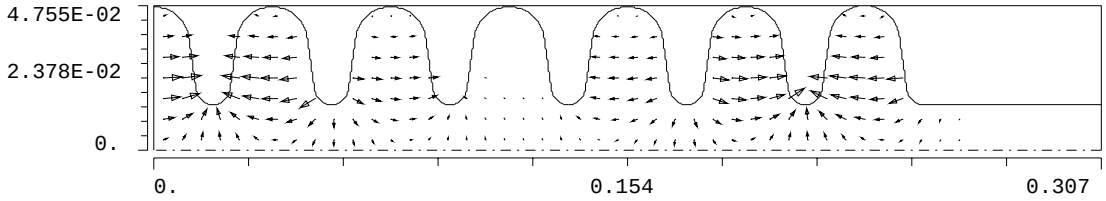

Figure 70: 13-cell cavity of shape C15, electric field of the mode $f = 3.9044$ GHz (b.cond. *EE*); phase advance $\varphi = 150°$.

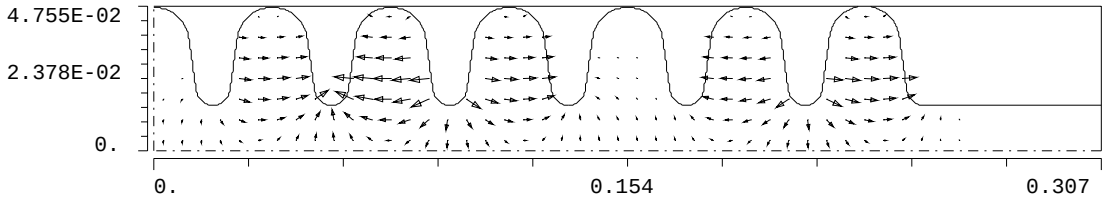

Figure 71: 13-cell cavity of shape C15, electric field of the mode $f = 3.9101$ GHz (b.cond. *ME*); phase advance $\varphi = 136°$.

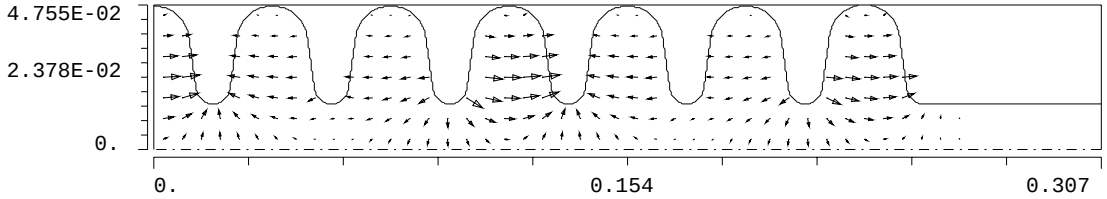

Figure 72: 13-cell cavity of shape C15, electric field of the mode $f = 3.9184$ GHz (b.cond. *EE*); phase advance $\varphi = 122°$.

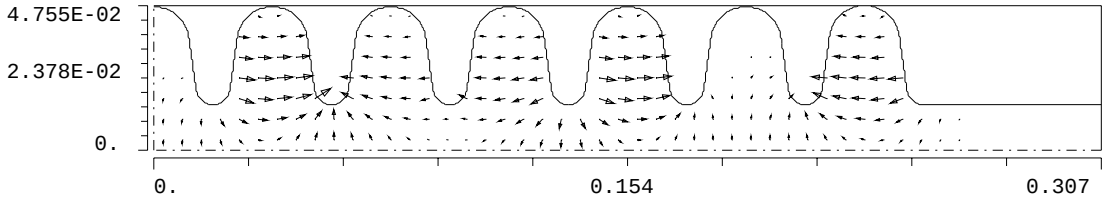

Figure 73: 13-cell cavity of shape C15, electric field of the mode $f = 3.9293$ GHz (b.cond. *ME*); phase advance $\varphi = 107°$.

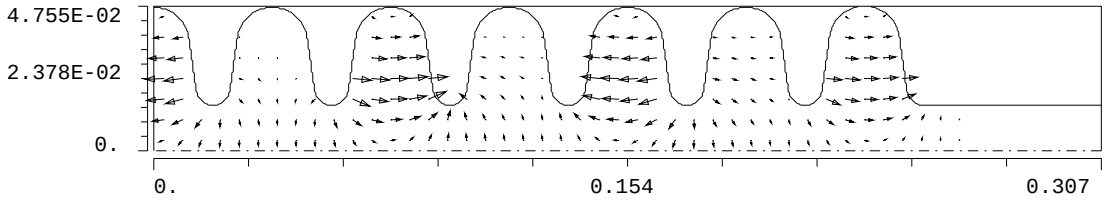

Figure 74: 13-cell cavity of shape C15, electric field of the mode $f = 3.9429$ GHz (b.cond. *EE*); phase advance $\varphi = 93°$.

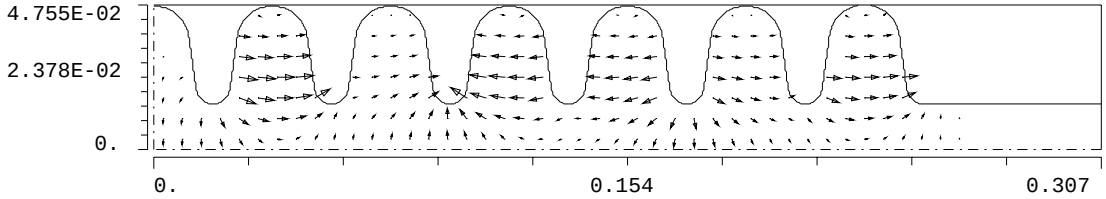

Figure 75: 13-cell cavity of shape C15, electric field of the mode $f = 3.9594$ GHz (b.cond. *ME*); phase advance $\varphi = 79°$.

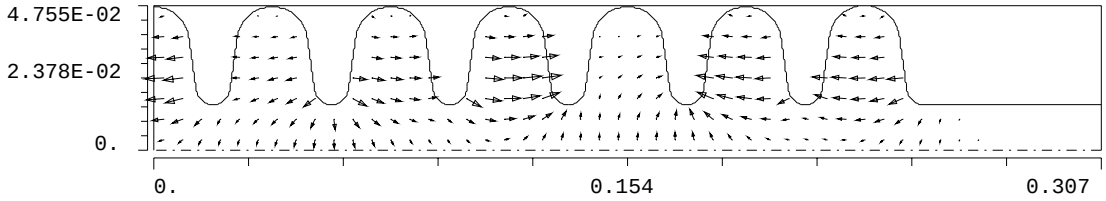

Figure 76: 13-cell cavity of shape C15, electric field of the mode $f = 3.9785$ GHz (b.cond. *EE*); phase advance $\varphi = 65°$.

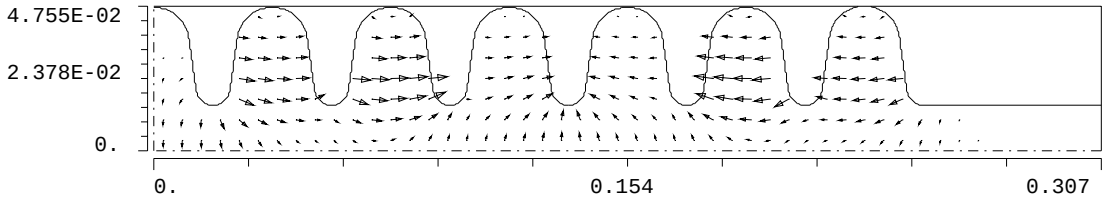

Figure 77: 13-cell cavity of shape C15, electric field of the mode $f = 3.9996$ GHz (b.cond. *ME*); phase advance $\varphi = 51°$.

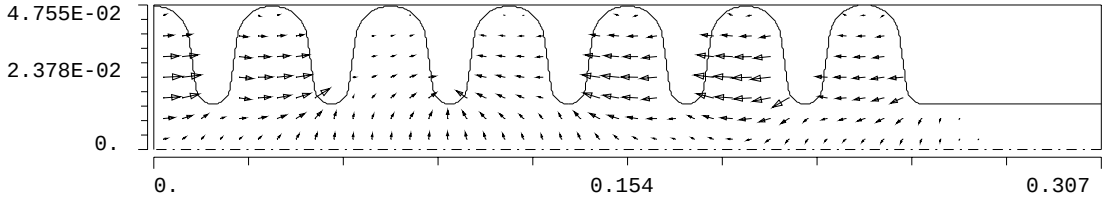

Figure 78: 13-cell cavity of shape C15, electric field of the mode $f = 4.0215$ GHz (b.cond. *EE*), phase advance $\varphi = 38°$.

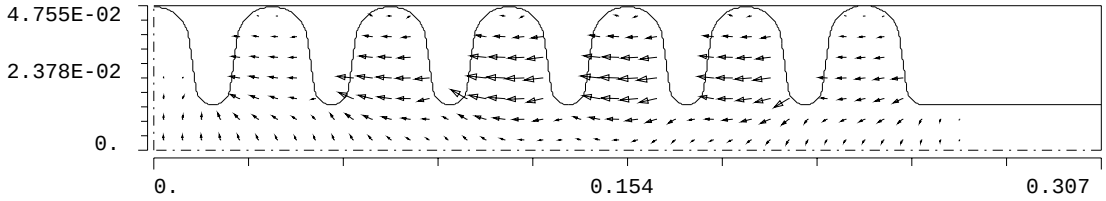

Figure 79: 13-cell cavity of shape C15, electric field of the mode $f = 4.0417$ GHz (b.cond. *ME*); phase advance $\varphi = 25°$.

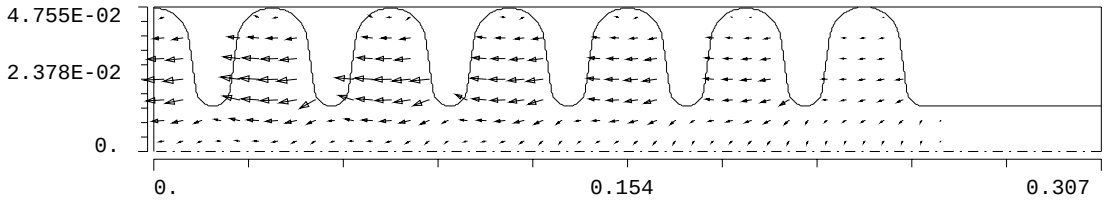

Figure 80: 13-cell cavity of shape C15, electric field of the mode $f = 4.0564$ GHz (b.cond. *EE*); phase advance $\phi = 12°$ ($\pi/15$-mode).

D Cavity of shape C15 with an alternative end-cell design

The purpose of this appendix is to show how an end-cell could look like which is well suited to mount a coaxial coupler with an inner conductor penetrating into in an enlarged beam pipe. Fig. 81 shows the considered configuration of a mid-cell and an end-cell with an iris diameter of 18 mm [19]. The longitudinal electric field at 5 MV/m transverse voltage is show at a fixed radius of 1 cm in Fig. 82.

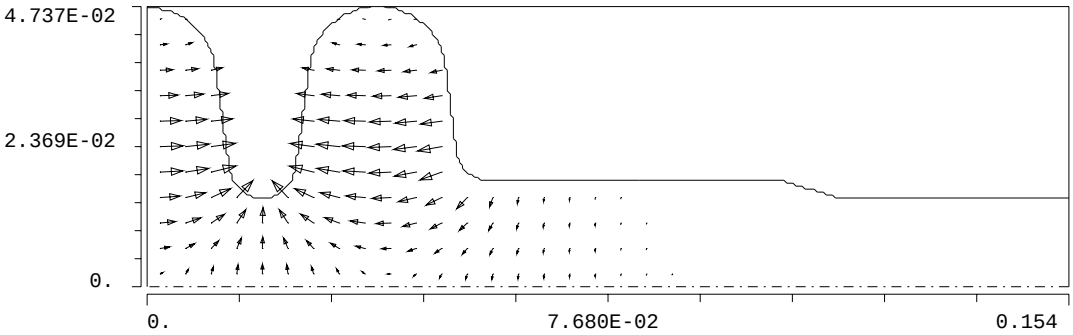

Figure 81: Cavity of shape C15, the electric field of the π-mode ($f = 3.8992$ GHz) is shown.

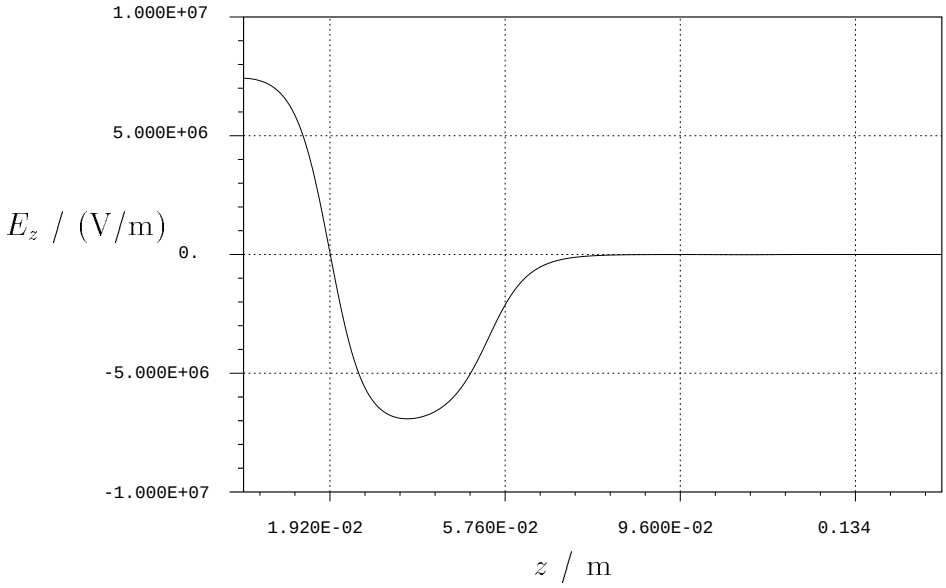

Figure 82: Cavity of shape C15 with an alternative end-cell design ($f = 3.8992$ GHz). The longitudinal electric field of the π-mode at 5 MV/m transverse voltage is show at a fixed radius of 1 cm.

The end-cup is slightly shorter than a regular cup. Furthermore are transition-cup (trans.-cup) is needed to adapt the end-cup to the mid-cell. A complete list of the geometrical parameters is given in table 11.

C15a		mid-cell	trans.-cup	end-cup
half cell length	$g/2$	19.2 mm	19.2 mm	18.6 mm
iris radius	a	15.0 mm	15.0 mm	18.0 mm
iris curvature	r_i	5.5 mm	5.5 mm	5.5 mm
equator radius	b	47.18 mm	47.37 mm	47.37 mm
equator curvature	r_e	11.41 mm	11.41 mm	11.41 mm
Mid-points	z_1	5.447 mm	5.448 mm	5.457 mm
	r_1	19.74 mm	19.75 mm	22.82 mm
	z_2	7.899 mm	7.897 mm	7.278 mm
	r_2	37.34 mm	37.52 mm	37.38 mm

Table 11: Geometrical parameters of the cavity input shapes of cavity C15 with an alternative end-cell design. The input shapes are approximated on a mesh, with about 7300 points per cell.

All modes of the first dipole mode passband of a 13-cell cavity of shape C15 with an alternative end-cell design are summarized in table 12. The electric field of the π-mode and the $\pi - 1$-mode (modes # 1 and # 2 in the table) are show in Fig. 83 and 85. A good field-flatness is achieved for the π-mode (see Fig. 84). The peak magnetic field for a transverse gradient of 5 MV/m is 0.079 T.

mode #	f / MHz	$(R/Q)'$ / Ohm	G_1 / Ohm
1	3899.6	348	229
2	3900.6	0.006	230
3	3903.7	0.846	230
4	3909.1	0.066	231
5	3916.7	0.766	233
6	3926.8	0.071	236
7	3939.4	0.412	239
8	3954.9	0.061	242
9	3973.0	0.045	247
10	3993.6	0.038	254
11	4015.8	0.045	262
12	4037.6	0.038	254
13	4054.9	0.011	282

Table 12: Results from the MAFIA eigenvalue solver and post-processor for a 13-cell cavity of shape C15 with an alternative end-cell designed.

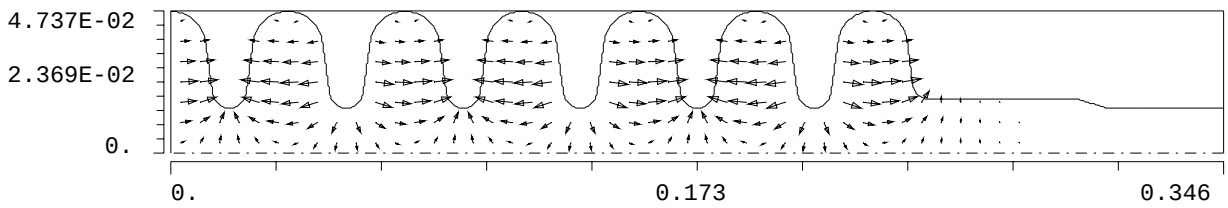

Figure 83: 13-cell cavity of shape C15, electric field of the mode $f = 3.8996$ GHz (b.cond. *EE*); π-mode.

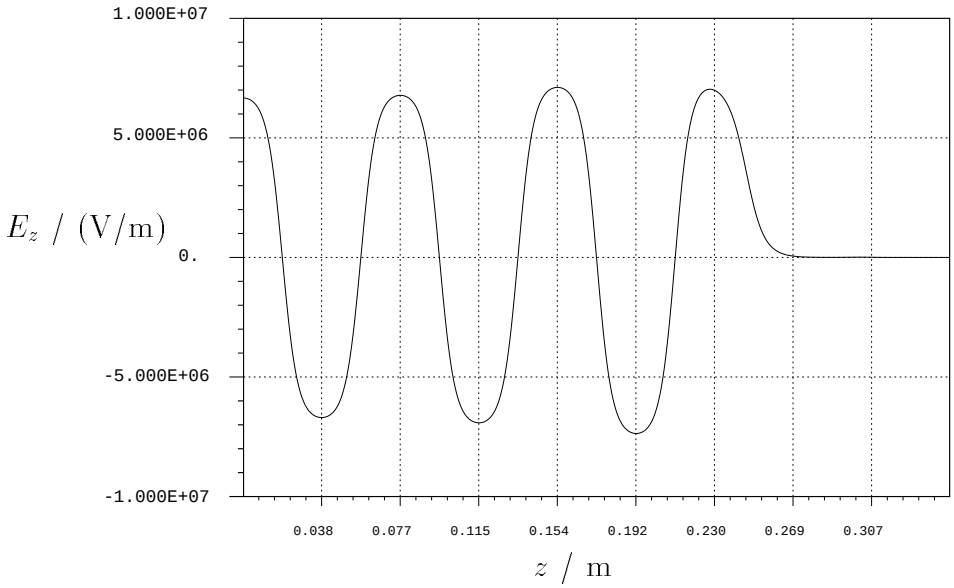

Figure 84: 13-cell cavity of shape C15 with a alternative end-cell design ($f = 3.8996$ GHz). The longitudinal electric field of the π-mode at 5 MV/m transverse voltage is show at a fixed radius of 1 cm.

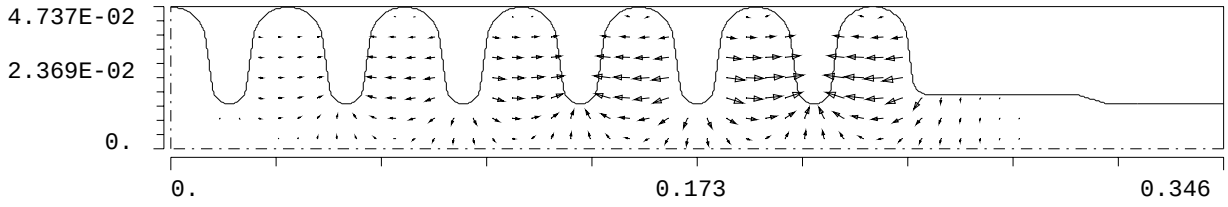

Figure 85: 13-cell cavity of shape C15, electric field of the mode $f = 3.9006$ GHz (b.cond. *ME*);$\pi - 1$-mode.

E Separator System and RF Cavity Parameters

Table 13: Separator System Parameters

Beam momentum, pc	22	GeV
Main Injector cycle time	3	sec
Extracted beam duration per cycle	1	sec
Main Injector intensity used	5×10^{12}	proton
Secondary beam intensity	$\approx 1.4 \times 10^{10}$	
Secondary beam current	$\approx 2.2 \times 10^{-9}$	amp
Potential beam loss on cavities	≈ 2	%
Power in lost beam	11	W
RF Station Configuration	2	stations
Distance between stations	86.5	m
Station deflection angle	0.68	mrad
Deflection per station	15	MV
Total deflection	30	MV
Deflection gradient	5	MV/m
Total effective RF length	6	m
Station effective RF length	3	m
Total # cavities	12	
System requirements @30MV		
Cryo power @1.8K bath, 2K surface	8.5	W/m
Cryo power @2.0K bath	20	W/m
Total cryo power @2.0K∗	120	W
Q_{ext}	6×10^{7}	
RF power @ 5MV/m	400	W/m
design margin	$\times 2$	
RF power/2m(4cav)	1600	W
RF power @ source supply	2.4	kW
# RF supplies/station	2	
Total # RF supplies	4	
Total RF power	10	kW
∗contingency factor= duty factor		

Table 14: Separator RF Cavity Parameters

Frequency	3.9	GHz
mode	π, $\approx$TM110	
Equator diameter body, (end)	94.36 (95.10)	mm
Iris diameter	30	mm
Cell length	38.4	mm
cells/cavity	13	
cells/m	26	
Effective RF length/cavity	499.2	mm
# cavities/m effective	2	
Overall length/cavity	660	mm
(R/Q)$\prime$/cavity*	351	Ohm
(R/Q)$\prime$/m	702	Ohm
V_{trans}	5	MV/m
E_{peak}@ 5 MV/m	18.5	MV/m
B_{peak}@ 5 MV/m	0.077	T
Coupling factor $(f_0 - f_\pi)/f$	0.04	
$f_\pi - f_{\pi-1}$	1.0	MHz
polariz-tune-split.	10 ... 40	MHz
tuning range	$\pm$ 1	MHz
Q_{copper}	1.4×10^4	
Q_{nb}@273K	Qcu/3	
$f/2Q_{nb}$@ 273 K	0.42	MHz
G_1 =Q$\times$ R_{sur}	228	Ohm
R_{sur} @ 2K, T_c/T=4.6	1.1×10^{-7}	Ohm
Q@R_{sur}	2.1×10^9	
Power dissipated@5MV, 2K	8.5	W/m
Q_{ext}	6×10^7	
full bandwidth f/Q_{ext}	65	Hz
U (stored energy)	0.73	Joules/m
Beam tube		
Mode	TE11	
Decay length	10.9	mm
Beam tube length	80.5	mm
$Freq_{cutoff}$	5.856	GHz
*P=V^2/2(R/Q)$\prime\times$Q		

Acknowledgment

One of the authors (R.W.) would like to thank all members of the A0 and KTeV groups for their kind hospitality during the visits to FERMILAB in 1999 (Apr. 10 to Jun. 12) and 2000 (Aug. 28 to Sep. 15). H. Edwards, M. McAshan and L. Bellantoni deserve special thanks for many helpful discussions and making the visits comfortable and productive.

References

[1] D. A. Edwards, Editor, *An RF Separated Kaon Beam from the Main Injector: Superconducting Aspects*, Fermilab TM-2060, October 1998

[2] T. Weiland, *On the numerical solution of Maxwell's Equations and Applications in the Field of Accelerator Physics*, Part. Acc. 15 (1984), 245-292

[3] T. Weiland, *On the computation of resonant modes in cylindrically symmetric cavities*, NIM 216 (1983) 329-348

[4] W.K.H. Panofsky, W.A. Wenzel, *Some consideration concerning the transverse deflection of charged particles in radio-frequency fields* , Rev. Sci. Inst. Vol 27, 11 (1956), 967

[5] P.B. Wilson *High Energy Electron Linacs: Application to Storage Ring RF Systems and Linear Colliders*, AIP Conference Proceedings 87, American Institute of Physics, New York (1982),p. 450-563

[6] K.L.F. Bane, R.L. Gluckstern *The Transverse Wakefield of a Detuned X-Band Accelerator Structure* , SLAC-PUB-5783, March 1992

[7] D.A. Watkins *Topics in Electromagnetic Theory* , Wiley 1958, New York

[8] D.R. Lide, Ed. *Handbook of Chemistry and Physics* , 79th edition, 1998-1999, CRC Press, Washington, D.C.

[9] M. Dohlus, private communication.

[10] W.W. Hansen, J. Appl. Phy., **V9**, p. 654-663 (1938)

[11] T.I. Smith, Stanford University High Energy Physics Laboratory Report HEPL-437 (1966)

[12] D. Nagle, E. Knapp, and B. Knapp, Rev. Sci. Instr., **38**, 1583 (1967)

[13] Thomas P. Wangler, *Principles of RF Linear Accelerators*, John Wiley & Sons, New York (1998)

[14] H. Padamsee, J. Knobloch and T. Hays, *RF Superconductivity for Accelerators*, John Wiley & Sons, New York (1998)

[15] R.L. Gluckstern, *Radio-Frequency Systems: Electromagnetic Fields in RF Cavities and Cavity Chains*, AIP Conference Proceedings 127, American Institute of Physics, New York (1985) p. 344-367

[16] H. Henke and M. Filtz, *Envelope Equations for Transients in Linear Chains of Resonators*, DESY, TESLA Report 93-26, June 1993

[17] J. Sekutowicz, *Transient State in Standing Wave Accelerating Structures*, Particle Accelerators, **V45**, p. 47-58, 1994

[18] J. Sekutowicz, C. Yinghua, and W. Yixiang, *A Different Tuning Method for Accelerating Cavities*, Proceedings of the 4th Workshop on RF Superconductivity, V. Kojima, Editor, KEK Report 89-21, January 1990, p. 849-857

[19] H. Edwards, *alternative end-cell design*, private communication